DOCTOR OF SCIENCES

Porous structured materials embedding tin and gallium as single-site for catalytic applications
effect of the hydrophobic/hydrophilic balance

VIVIAN, Alvise

Award date:
2020

Awarding institution:
University of Namur

UNIVERSITY OF NAMUR

DOCTORAL THESIS

Porous structured materials embedding tin and gallium as single-site for catalytic applications: effect of the hydrophobic/hydrophilic balance

---

Author:
Alvise VIVIAN

Supervisor:
Prof. Carmela APRILE
Prof. Damien P. DEBECKER

A thesis submitted in fulfillment of the requirements for the degree of Doctor of Philosophy

in the

Laboratory of Applied Materials Chemistry (CMA)
Department of Chemistry

March 11, 2020

Examining board:
Prof. Robert Sporken (UNamur)
Prof. Sonia Fiorilli (Politecnico di Torino, Italy)
Prof. Eric Gaigneaux (UCLouvain, Belgium)
Prof. Michel Devillers (UCLouvain, Belgium)

ABSTRACT

The quest for more sustainable processes in a future biomass-based industry, guides the interest in the development of novel heterogeneous catalysts. In the panorama of bio-based feedstocks, glycerol, especially coming as a by-product from the production of biodiesel, can be an attractive platform for the synthesis of valuable chemicals. Promising routes for its valorization are represented by the condensation of glycerol with acetone to produce solketal, or by the synthesis of ethyl lactate from dihydroxyacetone, which can itself be obtained by partial oxidation of glycerol. Both these added-value products present several applications in industrial areas related to chemicals, food, pharmaceuticals and cosmetic products. A sustainable way to perform these reactions envisages the use of heterogeneous silica-based catalysts presenting a metal inserted as single-site in the matrix, displaying Brønsted and/or Lewis acidity. A vivid interest is growing for the design of robust and active metal-substituted silicates for these applications and, in this context, sol-gel chemistry demonstrated to be a powerful tool providing a wide range of tunable parameters to tailor the physico-chemical properties of these solids.

This thesis explores novel sol-gel routes proposing a valid improvement of knowledge in the field of metal-substituted silicates as versatile acid catalysts. The importance of the efficient insertion of metals in the silica matrix as well as the morphology is highlighted. Novel silica-based nanotubes and aerosol-made silicates presenting Sn and Ga inserted as single-site are prepared and properly characterized. The catalytic activity of each solid, presenting the desired balance of Brønsted and Lewis acid sites, is evaluated in the synthesis of solketal and ethyl lactate under specific reaction conditions. With the aim of improving both activity and selectivity, the efficient insertion of metals and the precise tuning of the morphology can be combined with the control of adsorption/desorption phenomena on the surface. Since the affinity of reactants and products with the catalytic surface can be guided by hydrophilic/hydrophobic interactions, a systematic study is devoted in this work to the deep understanding of the impact of surface polarity on catalytic activity. Exploiting the aerosol process, functionalized metal-silicates are prepared in one-pot using different organosilanes. The control of surface polarity, achieved with a proper surface functionalization, proved to be a powerful tool for the optimization of the global efficiency of the catalysts.

Acknowledgements

Une aventure aussi passionnante que riche en défis n'est jamais entreprise en solitaire et nous devons tout ce que nous sommes devenus aux personnes qui nous ont accompagnés jusqu'à présent.

Tout d'abord, je tiens à adresser ma sincère gratitude à ma promotrice, la Professeure Carmela Aprile, et à mon co-promoteur, le Professeur Damien Debecker, pas seulement pour leur encadrement intellectuel mais aussi pour m'avoir donné la possibilité de travailler à leurs côtés. D'une manière particulière, un grand merci est destiné à la « Prof », Carmela Aprile, qui avec son énergie intarissable, avant tout humaine et scientifique, m'a toujours donné confiance, contribuant toujours à nourrir ma passion pour la recherche. Je lui suis redevable de m'avoir accompagné dans mon évolution et d'avoir « endurci mon armure », en tolérant souvent mon manque de pragmatisme et ma lenteur à distinguer les vraies priorités.

Les pages de ce manuscrit ont mûri aussi grâce à l'atmosphère joyeuse du laboratoire CMA, alimentée par des personnes merveilleuses. Je tiens à remercier ses membres, actuels et passés, qui ont toujours contribué à le soutenir en tant qu'équipe formidable. Un Grand merci à Mireia, Lucia, Alexandra, Valerio, Amélie, Anthony, Alessandra, Andrea, Hussein, Carla, Esther, Sandrine, Chloé et ... Adrien, qui perd de plus en plus le rôle de simple collègue pour devenir un cher ami. Merci à Luca, avec qui je me sens lié par une complicité fraternelle et qui m'a inlassablement sauvé des moments difficiles en m'accueillant chez lui comme un membre de sa famille. À ne pas oublier mes autres amis namurois, Andrea, Anaelle e Francesco, pour les belles soirées et bonnes conversations ensemble. Une foule de souvenirs et de bons moments me lie à vous tous, avec qui j'ai passé plus de temps ces dernières années qu'avec ma famille.

Je voudrais ensuite adresser mes remerciements à Nikolay, Corry, Pierre, Alexandre, Laurent et Giuseppe pour leur expertise scientifique, technique et logistique sans laquelle ce manuscrit n'aurait que peu de valeur. Un grand merci aussi à Val pour sa rigueur analytique, son dévouement et sa joie de vivre.

Je suis très reconnaissant aux membres de mon comité d'accompagnement – les Professeurs Eric Gaigneaux et Michel Devillers – non seulement pour

avoir partagé mon parcours de thèse mais aussi pour m'avoir aidé à porter un regard plus critique sur ma recherche. Je tiens également à remercier chaleureusement la Professeure Sonia Fiorilli pour avoir accepté de faire partie de mon jury de thèse et pour son précieux apport scientifique. Enfin, je remercie le Professeur Robert Sporken qui a accepté le rôle de président du jury.

Je crois fermement que l'on ne peut pas vivre sans cultiver des liens affectifs profonds. Pour cette raison je voudrais commencer par remercier une personne qui m'a pris au dépourvu il y a plus d'un an, en devenant l'une des personnes les plus précieuses et qui a indéniablement nourri mon courage depuis lors. Merci donc à Loraine pour son soutien sans faille, pour maîtriser l'art de la discipline et pour sa rare pureté qui fascine mon âme.

Pour terminer, je ne saurais comment remercier plus profondément ma famille que j'aime énormément, qui a toujours été mon phare dans la mer tourmentée et qui m'a toujours soutenu dans mes prises d'initiatives en faisant preuve d'un amour infini.

This research project has been the result of a collaboration between the University of Namur and the UCLouvain through the ARC programme. This research used resources of the "Plateforme Technologique Physico-Chemical Characterization" – PC^2, the SIAM platform (Synthesis, Irradiation & Analysis of Materials) and the MORPH-IM platform (Morphology & Imaging) located at the University of Namur.

Contents

Context

The art of "Heterogreeneous" catalysis

If we can call art "the expression or application of human creative skill and imagination, to produce what is beautiful", some would maybe admit that this definition could be easily applied to the concept of materials chemistry. This definition is even more appropriate if we recall the concept of skill as "capacity acquired through systematic and sustained effort to smoothly and adaptively carry out complex activities". Skill and knowledge are primary ingredients leading to understanding complex reactions and developing novel catalysts. It is commonly accepted that contemporary chemical industry requires alternative and environmentally friendly catalytic processes. This trend on the way to 'green chemistry', in agreement with the 12 Principles of Green Chemistry established by Anastas and Warner [1], demands a paradigm shift from the traditional concept of process efficiency, that focuses mostly on chemical yield and profit, to one that accredits economic value to eliminating wastes at the source and avoids the use of toxic and/or hazardous substances. Nowadays, especially heterogeneous catalysis, plays more than ever a key role in the development of a more sustainable society in which chemicals, materials and energy are produced considering both resource efficiency and waste minimization. In this background, the development of novel and highly efficient heterogeneous catalysts represents one of the main challenges attracting the attention of a very active scientific community. Since they can be easily separated from products and unreacted starting materials, reactivated and reused in consecutive cycles, heterogeneous catalysts constitute a valid alternative to standard non-catalyzed processes as well as to homogeneous catalysis. One of their major drawbacks is represented by diffusion limitations that reactants and products may encounter while approaching or leaving the active sites. Hence, considerable efforts are dedicated to the design of novel heterogeneous

catalysts able to enhance the accessibility of highly dispersed and well-defined active centers in order to simulate the behavior of the homogeneous ones. As a result, a large variety of approaches ranging from the reduction of the catalysts particle size and modification of their shape to the synthesis of highly porous materials have been investigated and new processes for their synthesis have been optimized. Due to their high chemical and thermal stability as well as the relatively easy synthesis procedure allowing a careful control of the textural and structural features, silica-based solids are probably the most used supports for catalytic purposes. Concerning the possible applications, in the field of green chemistry, it was already pointed out that some starting materials may come from bio-sources and can be produced via a low energy consumption and reduced costs strategies compared to standard petrochemical-based reactants. Glycerol represents one of the most abundant biomass derived product. The conversion of glycerol and its derivatives to added-value chemicals is receiving a considerable attention due to the growing interest for biodiesel as alternative to fossil fuels. Biodiesel production is based on the transesterification of triglycerides obtained from natural lipids and yields glycerol as the main co-product. Glycerol through an acetalization reaction with acetone can be converted to solketal, which has direct applications as surfactant, fuel additive and flavoring agent [2–4]. The acetalization reaction is typically catalyzed by Brønsted acids [5–7], though metal-substituted mesoporous silicates displaying mainly Lewis acidity have also been reported as promising heterogeneous catalysts for this reaction [8]. Another relevant process is represented by the conversion of trioses such as dihydroxyacetone (DHA), obtained from glycerol via catalytic processes, to ethyl lactate. This attractive product can be employed as green solvent, as precursor for the synthesis of polylactic acid and in various other applications related to food, pharmaceutical and cosmetic industry [9, 10]. This second reaction is also catalyzed by a combination of Brønsted and Lewis acidity, with the former promoting the dehydration of dihydroxyacetone to pyruvic aldehyde, and the latter catalyzing the rearrangement of this intermediate to ethyl lactate. In this context, porous silicates embedding different metal elements (Sn, Ga, Zr…), partially substituting silicon in their framework, have been reported as active and selective catalysts for the conversion of glycerol and its oxidation derivative (dihydroxyacetone) to solketal and ethyl lactate respectively[11–13]. Moreover, these two reactions can be classified as a high atom economy process (87%) with a potentially low E factor. This emerging biomass-based industry is dealing

with polar and highly functionalized molecules, that ideally should be manipulated in aqueous media. Therefore, new catalysts active and selective under mild conditions should be created, dealing with multifunctional molecules for which adsorption and residence time on the surface are dictated among others by hydrophilic/hydrophobic interactions. Often underestimated, the impact of a careful tuning of the surface polarity has already been reported to have a high valorization potential in terms of process developments and should be not neglected in the design of efficient catalysts. There is thus certainly room for the improvement of these complex systems, dealing with the future generation of bio-feedstocks, using a systematic and careful approach.

Inspired from these concepts and from the recent challenges facing "Heterogreeneous" catalysis, this work proposes a contribution to the development of novel metal-substituted silica-based structured catalysts obtained mastering advanced sol-gel synthetic procedures. Their tailored properties and specific morphologies will allow targeting high activity, selectivity, stability in the valorization of biomass-based molecules.

General Introduction

1.1 Development of porous materials

Porous structured materials incessantly trigger the interest of scientific community due to their innumerable applications in petrochemical, environmental and catalytic technologies. The presence of uniform channels and cavities, high adsorption capacity and tunable active sites are some of the unique features responsible of their success. Among the most frequently studied structured porous materials we find zeolites, ordered mesoporous silica and more recently metal–organic frameworks (MOFs) (Figure 1.1). Speaking more specifically about heterogeneous catalysts, the discovery of zeolites represented a revolution. They are an important group of solids with large-scale applications especially in the refinery industry and with an increasing potential in environmental catalysis[14]. Zeolites are microporous crystalline aluminosilicates, structured by SiO_4 and AlO_4 units in a tridimensional framework. Zeolite Y, ZSM-5, beta and mordenite are popular zeolites for industrial applications due to their extraordinary stability. Their good performances, robustness under severe conditions and relatively economical production allowed these solids to be used as heterogeneous catalysts since the 1960s[15]. However, these materials may encounter some limitations and hence be inadequate when processing feedstocks with molecular dimensions greater than their micropores. In this context, the discovery of the M41S family of ordered mesoporous materials (i.e. MCM-41, MCM-48 and MCM-50) in the 1990s, accompanied later by analogous solids such as FSM-16 and SBA-15, created new perspectives in the panorama of heterogeneous catalysis[16, 17]. These mesoporous materials constituted of purely silica framework, present high specific surface areas (700–1500 $m^2\,g^{-1}$), large pore volumes and tunable pore dimensions (2–50 nm), making them interesting in the field of adsorption, sensing and catalysis[18–20]. The relatively large pores in mesoporous silica-based solids, if

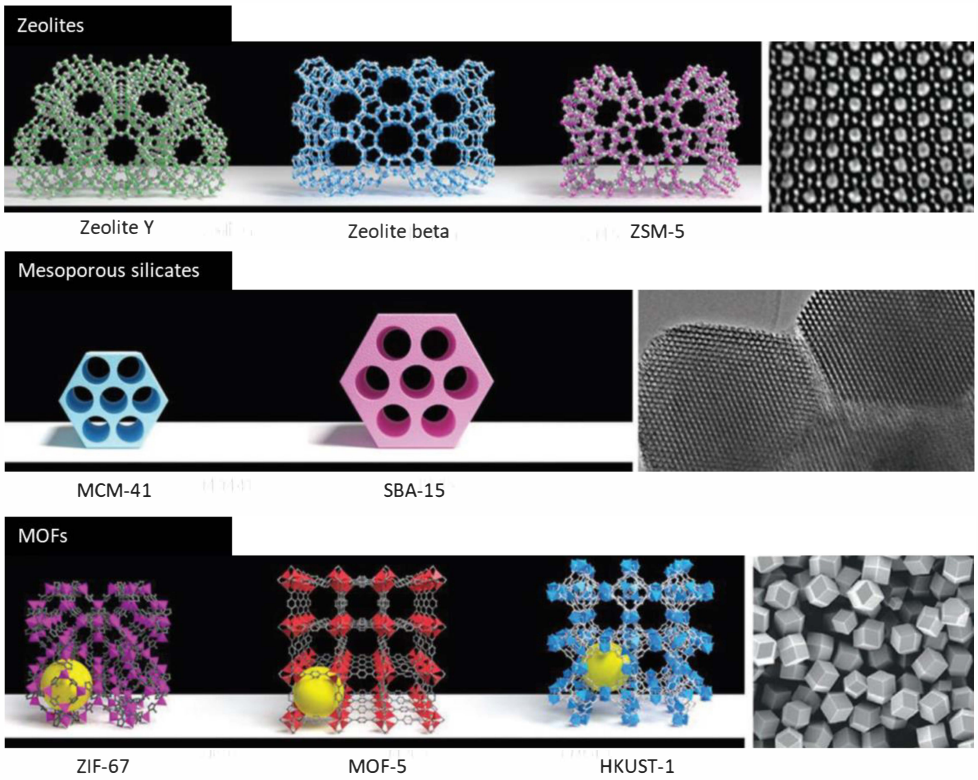

FIGURE 1.1: Structural models (left) and TEM micrographs (right) of some among the most frequently studied structured porous materials. Structures obtained from their single-crystal X-ray diffraction data. Picture adapted from[21]

compared to zeolites, facilitate mass transfer and enable catalytic reactions involving bulky substrates. However, the purely siliceous composition of this family of solids allows only limited application in the field of catalysis. In order to take advantage of their features for a wide range of catalytic applications, a modification of these mesoporous silicas is indispensable. Grafting of functional groups, insertion of metal elements in the silica matrix or deposition of metal nanoparticles on their surface are only few of the possibilities to largely enrich their catalytic applications.

Another class of porous materials, more recently discovered, is represented by MOFs. In contrast to the purely inorganic zeolites and mesoporous silicas, MOFs are inorganic–organic hybrid materials built from metal ions coordinated with organic linkers[21–23]. They present extremely high specific surface area up to 10.000 $m^2\,g^{-1}$ and for their synthesis almost all the transition metals and a large variety of organic linkers have been already used[24]. These attractive features give MOFs a vast potential for various applications

in heterogeneous catalysis especially in the case of the highly robust MIL-101(Cr), UiO-66(Zr) and PCN-224(Zr)[25–28]. The three types of porous materials briefly presented (zeolites, silica-based mesoporous solids and MOFs) are certainly very attractive for catalytic applications. In this manuscript, we aim to provide a more specific focus on mesoporous structured solids and in particular metal substituted silica-based catalysts.

1.2 Mesoporous structured silicates

Mesopores are defined by IUPAC as pores with sizes in the range of 2–50 nm. The first reports on the synthesis of mesoporous materials, in the early 1990s, were a milestone in materials chemistry and drove a wave of research interest on the synthesis of other mesoporous materials with many different ordered structures and pore sizes[29]. The general approach to the synthesis of mesoporous silica materials involves "soft-templating", which is actually very similar to the method traditionally used to prepare zeolites[30]. However, there are some key differences between the two. One of the first synthesis of mesoporous materials with tunable pore sizes was a rather revolutionary work in the early 1990s, where Kato and co-workers[31] developed a convenient method for synthesizing mesoporous silicas by using polysilicate kanemite ($NaHSi_2O_5$) as the silica precursor and as templating agent alkyltrimethylammonium chloride, which has a much bigger size than tetrapropylammonium ions, characteristic to zeolite synthesis. Kresge and co-workers again in the nineties, reported the synthesis of the Mobil composition of matter (MCM)-41[16] and the concomitant syntheses of MCM-48 and -50 mesoporous silicas. These are most probably the best known and most widely studied mesoporous silica-based solids and they were among the first series of mesoporous materials documented in the literature with not only mesoscopic pores but also well-ordered structures. The above-mentioned family of mesoporous materials (called M41S) was synthesized from the hydrolysis of silica precursors followed by the condensation around ordered arrays of surfactant micelles. The final removal of the templating agent can be obtained by calcination or solvent extraction. The use of a precise range of concentrations of cationic surfactant as cetyltrimethylammonium ion in aqueous solution, led to the formation of a regular array of cylindrical micelle aggregates. The synthetic method allowed the formation of different types of mesoporous silica solids having

regular arrays of uniform cylindrical channels as a result of the spontaneous self-assembly of surfactant species, obtained varying parameters as the nature of surfactant and silica precursor/surfactant ratio.

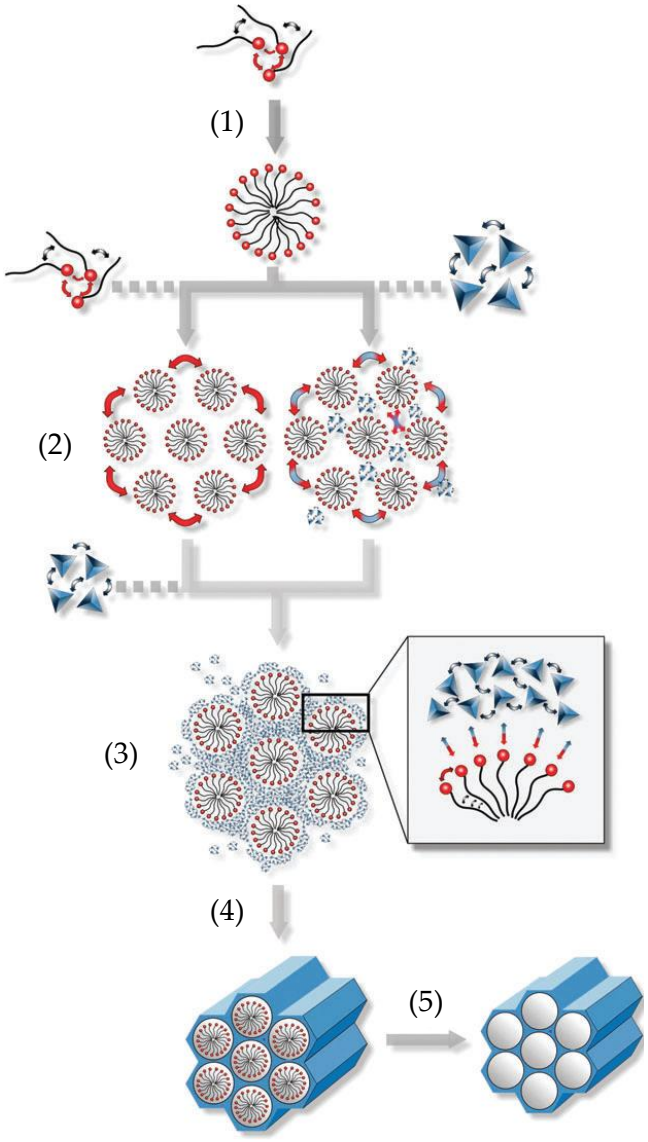

FIGURE 1.2: Schematic representation of the formation of mesoporous materials by structure-directing agents (adapted from[32])

With the aim of giving an explanation to the formation of the highly ordered mesoporous structure of M41S solids, Kresge and coworkers[16] proposed a mechanism known as liquid crystal templating. According to the authors the process involves the following four steps, as schematized in Figure 1.2: (1) surfactant micelles form in the aqueous solution and assemble into cylindrical micelles; (2) the cylindrical micelles are organized into a regular

array of liquid crystalline structures which can evolve to several mesophases (here a hexagonal mesophase); (3) the attraction between the hydrolyzed silica source and the positively charged surfaces of liquid crystalline surfactant micelles ensures an interaction of the silica phase around the soft template. This type of interaction is made possible by the basic medium in which the synthesis is performed, allowing the formation of anionic silicates in the solution (starting from a precursor such as tetraethyl orthosilicate (TEOS)). Finally, the polycondensation of the silica precursor results into a mesostructured solid (4). The last step envisages the removal of the surfactant either by calcination or by solvent extraction to release the materials porosity (5). Two additional approaches, developed by Pinnavaia et al., for the synthesis of mesoporous materials based on non-ionic organic–inorganic interactions, deserve to be mentioned. They took advantage of neutral surfactants such as primary amines and poly(ethylene oxides) to prepare hexagonal mesoporous silica[33, 34], and MSU (Michigan State University material)[35], respectively. The main difference when non-ionic surfactants are used, instead of ionic ones, is the affinity between soft template and silica forming phase that is driven by hydrogen bonding instead of ionic interactions. One of the most used groups of surfactant, the Pluronic family, are triblock co-polymers consisting of poly(ethylene oxide)$_x$–poly(propylene oxide)$_y$–poly(ethylene oxide)$_x$, $(PEO)_x(PPO)_y(PEO)_x$, which show the ability to form liquid–crystal structures. They can be used to synthesize a variety of different ordered mesoporous materials with rather large pores (between 4 and 13 nm) and various framework compositions under strongly acidic conditions[36–38]. The interactions between the silanol groups and non-ionic templates are possible in acidic reaction media due to the formation of hydrogen bonds[39]. Formed via this pathway, 2D hexagonal mesoporous material denoted as SBA-15 (Santa Barbara No. 15), exhibits large pore sizes adjustable between 6 and about 15 nm. The thick wall of this material significantly improves the thermal and hydrothermal stability compared to mesoporous MCM-41 and related silicas. One interesting feature of SBA-15 is the presence of microporosity which branch out in its mesopore wall, connecting neighboring mesopores. One of the interesting features of ordered mesoporous solids for catalysis is the multitude of possibilities to modify them. The modifications can be used to adjust surface functionality, to incorporate catalytic functions or to change their textural properties. The rich organization of lyotropic surfactant system can be used to obtain many morphologies. In addition to the standard particle form, fibers and ropes , gyroids, hollow

and solid spheres, films, nanotubes and many other morphologies can be obtained[40](Figure 1.3).

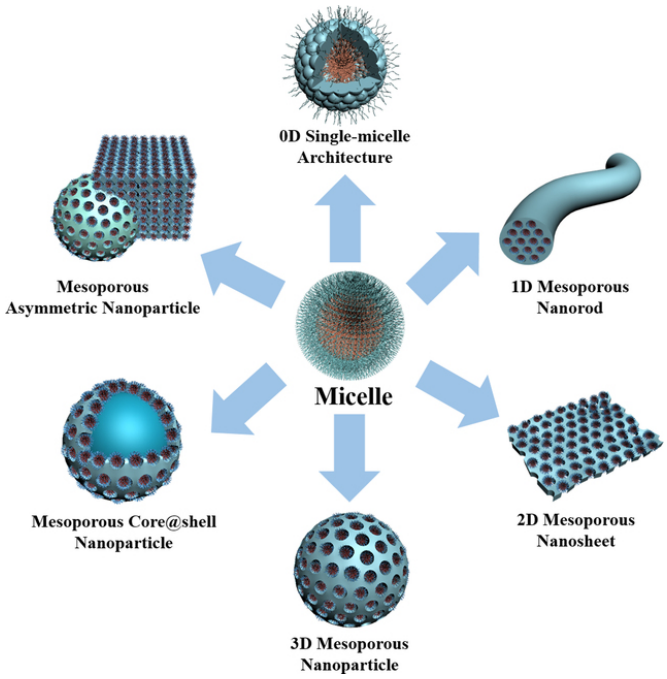

FIGURE 1.3: Schematic illustration of the single-micelle-directed synthesis of ordered porous materials with different possible architectures. Figure adapted from [41]

For instance, in the comprehensive series of porous silicates, the controlled preparation of nanotubes constitutes a recent progress. In 1999, Harada and Adachi[42] reported a sol-gel method for the synthesis of single silica nanotubes or bundles through a surfactant-mediated template mechanism and they described the procedure for controlling the geometry of the tubes. These open-ends tubular nanostructures display promising features as supports in heterogeneous catalysis (see Part I of the manuscript). Another promising synthetic route to obtain mesoporous silica-based catalysts is represented by the aerosol assisted sol-gel processes. In these preparation procedures, a precursors solution containing a surfactant is sprayed and dried under mild temperature to rapidly trigger the inorganic polycondensation reactions, yielding materials with spherical shape, high homogeneity and tunable texture. These processes have been coined as "Type IIIc" aerosol processes in a recently proposed classification[43]. The advantages of this process compared to conventional sol-gel approaches include: a limited number of steps, a much shorter synthesis time, a limited waste generation and low environmental impact[43, 44](see Part II of the manuscript).

1.3 Isomorphous substitution of heteroelements generating acid sites

Structured porous solids constituted of whole silica possess rather limited applications in catalysis[45]. The incorporation of heteroelements (where hetero means different from silicon), as reported in the case of zeolites, is one of the possible routes to modify the properties of silica framework and broaden the range of possible catalytic applications. In this section, some general aspects concerning the isomorphous substitution of silicon with other elements will be illustrated, with a special focus on the generation of acid sites. When trivalent cations like Al^{3+}, Ga^{3+}, B^{3+} or Fe^{3+} isomorphically substitute a silicon atom in the walls of structured silica, a combination of Brønsted and, in a minor extent, Lewis acidity is generated. The Brønsted acidity arises from hydroxyl protons located on oxygen bridges between silicon and the trivalent cation (Figure 1.4a). The presence of Brønsted acidity can be explained via an interaction between the oxygen of the OH group of a tetrahedral framework Si atom with a neighbor M^{3+} acting as Lewis base. As a consequence of this interaction (Figure 1.4a) weakly bonded proton are generated. The nature of the trivalent cation as well as its amount and dispersion strongly influence the strength of Brønsted acid sites. The Si-O-M angle is another important parameter to be considered. In addition, the O-M distance plays a fundamental role in the Brønsted/Lewis acid balance. For instance, in mesoporous solids with amorphous walls, the O-M distance is usually longer than in crystalline zeolites thus inducing in the former a higher amount of Lewis sites[46]. The Lewis acidity is usually attributed to a non-complete coordination of the intra-framework metal cation with the consequent availability of a free orbital which may interact with external Lewis bases. When cations like Ti^{4+}, Sn^{4+}, V^{4+}, Zr^{4+} are introduced, this substitution is reported to generate a combination of Lewis and, in minor amount, Brønsted acid sites (Figure 1.4b). The Lewis acid character is again attributed to the availability of a free orbital of the metal center bound to four framework oxygen, able to accept electron pairs and hence lead to chemical activation of reactants presenting electron rich groups[47]. The Brønsted acid character can arise from an expansion of the coordination number (for example from 4 to 6) forming bridged OH groups possessing Brønsted acidity.

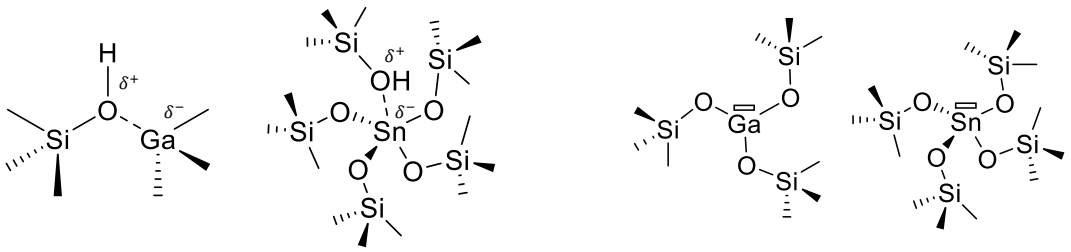

(a) (b)

FIGURE 1.4: Schematic representation of isomorphically substituted tri-valent Ga cation and of tetra-valent Sn cation, generating a combination of Brønsted (a) and Lewis (b) acid sites

The modification of the framework composition is possible either by co-synthesis starting from mixtures containing both silica precursors and heteroelement containing salts, or by post-synthesis on a pure silica material. These two synthetic methods may result in different final catalysts and the nature of the reagents used for grafting/co-synthesis can strongly impact the properties of the resulting materials. The co-synthesis method generally results in a relatively homogeneous incorporation of the heteroelement. However, a non-negligible proportion of these sites may be located inside the walls of mesoporous silicas, not accessible to substrates during the catalytic application. The post-synthesis procedure primarily grafts the active species on the wall surface and if the same loading than co-synthesis is used, it leads to increased concentration and accessibility of the catalytically active sites on the external surface of the material. Nevertheless, this technique may be accompanied by an uneven distribution of metal active sites that can eventually migrate on the surface forming aggregates and even inactive clusters. The possibility to replace isomorphically an atom in the silica framework may depend on two competing factors. The required energy involved in the deformation of the lattice caused by the replacement of an atom with a different radius or charge and, particularly in the case of zeolites, in the gain of energy derived from the increased configuration entropy[47]. Usually, the isomorphous substitution is possible between atoms characterized by similar sizes and electronegativities with an assumed critical difference of about 15% in the radii and 0.4 a.u. in the electronegativity scale. These very general criteria have found application for instance to the deeply studied world of zeolites, where the incorporation of tri- and tetra-valent heteroatoms as B^{3+}, Al^{3+}, Ga^{3+}, Fe^{3+}, Ti^{4+} and Sn^{4+} are easily achieved. The incorporation of tri and tetra-valent heteroatoms in the

framework of silica-based solids allows tailoring the amount and strength of Brønsted and Lewis acidity as well as their balance. The degree of silicon substitution in the structure is not only related to the nature of the metal elements but also to several parameters such as pH of the synthesis mixture or to special hydrothermal treatments. In particular, it has been reported both in the case of zeolites as the MFI and MCM-41, that the degree of isomorphous substitution decrease in the order: Al > Ga> Fe[48], in accordance with the previously mentioned general rules. Another peculiarity correlated to the type of trivalent cation is the acid strength of the bridging hydroxyl groups. An estimation of the deprotonation energy made by quantum chemical calculations indicated an increasing energy value for the series Al > Ga> Fe[49], representing a decreasing strength of bridging hydroxyl groups. However, in terms of Lewis acidity strength, it has been reported that the insertion of Ga generates stronger acid sites compared to Al, especially in MCM-41-like solids[50].

Some considerations worth to be made on the stability of the heteroatoms integrated in the silica framework. The stability of Al, Ga and Fe in tetrahedral coordination was reported in the case of zeolites to be often critical[51]. For this reason, the application of thermal treatments may provoke the migration of metals in extra-framework positions with the subsequent aggregation to form dimeric species and clusters. The presence of extra-framework isolated species is related to the formation of Lewis acid sites and was associated to the enhancement of the catalytic performances in aromatization reactions on Ga-containing MFI[52] and BEA[53] zeolites. The incorporation of tetra-valent metals M^{4+} into the silica structure may generate single-site Lewis acid domains. However, in contrast to Brønsted acid sites, the quantification of the strength of Lewis acid centers is more challenging as the affinity scale in this case strongly depends on the nature of the employed reference base molecule. This is related to the fact that the energy of Lewis acid–base interaction depends on the relative position of the highest occupied molecular orbital (HOMO) of the base and the lowest unoccupied molecular orbital (LUMO) of the acid[47]. The calculated adsorption energy of ammonia provided a more accurate prediction of the Lewis acid strength order for MFI zeolites: Ge < Ti < Sn < Zr[54]. The work of Gunther et al. is a rare if not the only example of an experimental study of Lewis acid strength associated with isolated M^{4+} atoms in the zeolite framework[55]. The ^{15}N chemical shift of adsorbed pyridine in magic angle spinning NMR was found to correlate linearly with the Mulliken electronegativity of the metal center in the order Ti < Hf < Zr < Nb < Sn.

1.4 Processes catalyzed by mesoporous solid with acidic properties

One of the most demanding field of applications of heterogeneous catalysts, including mesoporous materials, regard their use in cracking and hydrocracking reactions. Unfortunately, the poor acid strength and low hydrothermal stability of pure silica MCM-41 catalysts are a counterbalance to the advantage of the accessibility of the pores for bulkier molecules. Nevertheless, MCM-41 catalysts still show substantial cracking activity for bulky substances such as palm oil and asphaltene[56, 57]. Although the intrinsic weakness of the acid sites in mesoporous silicas restricts their applicability in many petrochemical reactions, still they present a great potential for instance in the production of fine chemicals which require a lower level of acidity. In addition, the relatively large pore channels of mesoporous materials offer the advantage of effective diffusion of bulky substances often found in fine chemicals synthesis. One of the earliest examples is that of a Friedel–Crafts alkylation with mesoporous aluminosilicates. The Al-MCM-41 with a pore diameter of 3.0 nm is active in the Friedel–Crafts alkylation of 2,4-di-tert-butylphenol with cinnamyl alcohol. The yield over Al-MCM-41 was much higher than over HY zeolite, suggesting the detrimental diffusion restrictions of the bulky alcohol in the zeolite pores[58]. These results clearly indicate the potentials offered by mesoporous materials in fine chemical synthesis with bulky substrates. Another interesting example, where direct synthesis and post-grafting impact the final activity of the catalyst, can be found in the Friedel–Crafts alkylation of benzene with benzyl chloride where Ga impregnated MCM-41 exhibited higher activity than Ga substituted MCM-41[59]. Acetalization is an important reaction for the protection of carbonyl functional groups. This reaction does not require strong acid sites, and therefore, mesoporous silicas with weak to intermediate acid site strength are suitable catalysts for this application[60]. For example, acetalization of heptanal, 2-phenylpropanal or diphenylacetaldehyde with trimethyl orthoformate was carried out over siliceous and Al-substituted MCM-41 on the one hand and different zeolite catalysts on the other[60]. Zeolite Beta and zeolite Y catalysts were found to be more active than mesoporous materials, but they deactivated more rapidly. There was no difference in activity between siliceous MCM-41 and Al-MCM-41, indicating that the bridging hydroxyl groups (Si–OH–Al) are of minor importance in this reaction and that

probably silanol groups are sufficient for catalysis in this case. Again, it was reported that when the size of the reactant increased, mesoporous solids had clear advantages over the zeolites. Acetalization is one of the reaction steps to produce jasminaldehyde. Al-MCM-41 with uniform mesopores was reported to be suitable for carrying out in good yield the three consecutive reactions to produce jasminaldehyde in one-pot[61]. From the comparison of several catalysts, including large pore zeolite (Beta) and mesoporous silica–alumina with various Si/Al ratios, it was concluded that a suitable catalyst should have mild acidity to avoid an excessive self-condensation of the aldehyde and undesired consecutive reaction. Aluminum substituted mesoporous silica exhibits better activity in Diels–Alder reactions with large organic molecules compared to conventional microporous zeolites (ZSM-5, HY)[62, 63]. In the reaction of cyclopentadiene with crotonaldehyde, aluminum isopropoxide grafted MCM-41 shows the highest activity compared to directly prepared or template ion-exchanged Al-MCM-41. Tin modified materials were found to be interesting catalysts for a number of important organic reactions. Sn-MCM-41 showed high activity in the Prins condensation of β-pinene and paraformaldehyde to nopol[58]. Conversion of β-pinene reached around 99% with good selectivity, whereas a reference amorphous silica catalyst only showed 37% conversion. Meerwein–Ponndorf–Verley (MPV) reaction is a useful reduction of a carbonyl substrate with a secondary alcohol. Zirconium 1-propoxide grafted SBA-15 shows high activity in this reaction and the rate of reaction increased with increasing Zr loading level[64]. It seems that the pore system of the support material influences the catalytic activity. In the reduction of 4-tert-butylcyclohexanone with 2-propanol, the initial conversion was in the order MCM-41 > MCM-48 > SBA-15. The advantages of using metal-substituted acid catalysts has been demonstrated in a wide range of reactions. The appropriate selection of the metal center allows to tune the catalysts properties balancing the Brønsted/Lewis acid properties needed often to perform multistep reaction with high selectivity.

1.5 Tin and gallium as single-site

A special focus in this work is dedicated to Sn and Ga silicates that are demonstrating promising applications especially in the valorization of biomass derived products. These metals emerged to be particularly adapted because

of their promising combination of Lewis and Brønsted acid sites. Stannosilicates have recently attracted significant attention as highly active and selective Lewis acid catalysts in a number of reactions involving transformation of biomass-derived substrates, such as monosaccharide isomerization[65, 66], retro aldol condensations[67], hydride shifts[67–69], as well as a number of other reactions including Meerwein–Ponndorf–Verley–Oppenauer (MPVO). In particular, tin atoms incorporated in zeolite beta have shown to be highly active sites for these reactions; however, owing to the difficulty in preparing Sn-beta, other materials have been investigated, such as the mesoporous stannosilicate Sn-MCM-41[69]. The incorporation of isolated tin atoms has been shown to introduce strong Lewis acid sites in the framework of silica-based solids[70]. Several studies [71–74] have shown that in Sn-beta the active site is partially hydrolysed, as shown in Figure 1.5b. It has been claimed that the hydroxyl group acts as a base, creating a bifunctional active site of fundamental importance for the activity of the catalyst[75].

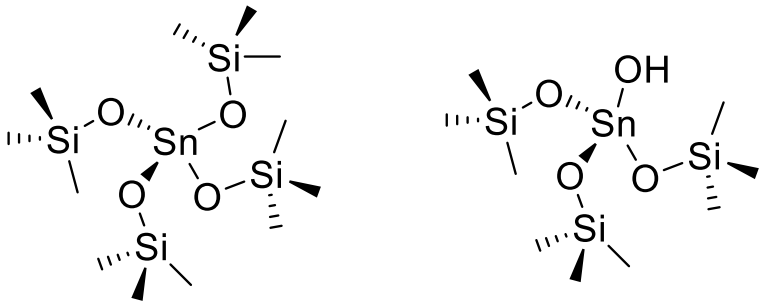

(a) (b)

FIGURE 1.5: Representation of Sn sites in Sn-beta zeolite: (a) perfect tetrahedral closed Sn site and (b) a partially hydroxylated Sn-OH open site[71].

There is a general agreement in the literature that Sn-beta zeolites are dominated by two major species: the partially hydrolyzed "open Sn site" (Figure 1.5b), where the Sn center forms three bonds with the surrounding zeolite lattice and one coordination site is occupied by an OH ligand, and a "closed Sn site" (Figure 1.5a), where Sn occupies a perfectly tetrahedral center[71]. It is proposed that the open site configuration allows for a higher flexibility of the Sn center resulting in a higher Lewis acidity and reactivity toward glucose activation[74, 76]. Computational studies on the mechanism of glucose to fructose isomerization by Sn-containing zeolites revealed the crucial role of secondary

hydrogen bonding interactions between the carbohydrate substrate and various OH sites neighboring the catalytic Sn species. Concerning the isomorphic substitution of Ga, catalysis over Ga-based zeolites focuses on alkylation, isomerization, and disproportionation of aromatics. These reactions have been investigated in detail to optimize product selectivity by utilizing the shape-selective properties of zeolites. Aromatization of low alkanes (Cyclar process) has gained a commercial breakthrough[77]. Ga-MCM-41 has been used to catalyze the aromatization of propene and, as compared with Al-MCM-41, Ga-MCM-41 presented a higher stability during reaction[78]. Less than 2% of the feed component is converted to higher boiling compounds and coke precursor products. Moreover, Brønsted acidity of Ga-substituted MCM-41 and -48[79] is sufficient to achieve cumene cracking and n-hexane conversion[80]. Mesoporous gallium silicates have also been exploited for a series of sustainable chemical processes including the synthesis of alkyl lactates and other valuable chemicals from glycerol and its derivatives[11–13]. In particular, it has been already reported that Ga-MCM-41 nanoparticles are one of the most efficient heterogeneous catalysts in the conversion of glycerol into solketal[11].

1.6 Characterization of acid properties

Understanding how acidity can be tuned by precise synthesis procedures or how it behaves under particular reaction conditions is essential in the design of new catalysts and in the prediction of catalysts performances. The combination of several characterization techniques is a prerequisite to convey all the necessary information to properly describe solid acidity. A broad variety of features has to be investigated, such as nature of the acid sites (Brønsted or Lewis), acid strength and distribution, site abundance and their accessibility. In this perspective, some of the goals in catalysis science concern the discovery of reliable experimental methods for characterizing these properties. The objective of this section will be to stand out some important features of a selection of characterization techniques used in the determination of solid acidity. Temperature Programmed Desorption (TPD) of basic molecules is one of the most utilized techniques mainly due to its simplicity and it has been largely applied to characterize zeolites[81]. In a standard TPD experiment the surface of the solid is initially outgassed at high temperature and then saturated with the selected probe molecule at low temperature. The sample is then subjected

to a temperature program to favor the desorption of the adsorbed base. The fundamental concept is that molecules adsorbed on strong binding acid sites are desorbed at higher temperatures than the temperature required to desorb molecules from weak acid sites. Raising the temperature, the rate of desorption also increases and the surface gets depleted of adsorbate. The amount of adsorbed base evacuated at different temperatures can give an estimation of the acid strength. The resulting TPD profile is represented in terms of concentration in the gas phase of probe molecule that desorbs at a certain temperature as a function of temperature[82]. An example of typical ammonia TPD spectrum of a proton exchanged zeolite is presented in Figure 1.6. It shows generally two desorption bands, one at low temperature (l-band) and one at high temperature (h-band). The l-band cannot be ascribed to desorption from a particular kind of acid site. It is instead the consequence of the strong saturation of the surface. The adsorption of ammonia first happens on Brønsted acid sites, to form ammonium species, and on strong Lewis sites. When all the sites are covered, incoming molecules start to get adsorbed on NH_4^+ species by hydrogen bonding.

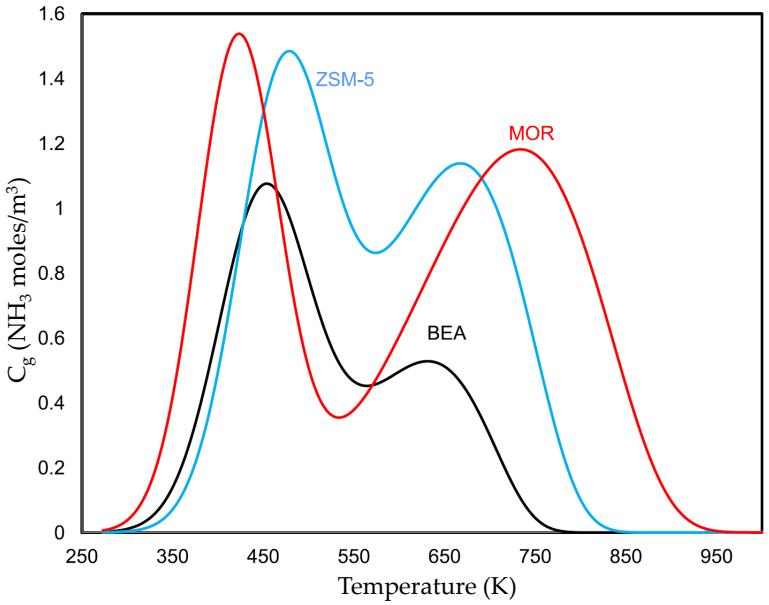

FIGURE 1.6: Typical NH_3-TPD profiles of three common zeolites: ZSM-5, MOR and BEA. Two desorption bands, one at low temperature (l-band) and one at high temperature (h-band) are observable (adapted from[83])

Therefore, the l-band cannot be considered in the quantification of acidic sites since it is even observable in sodium exchanged zeolites[84]. To suppress this contribution a steam treatment can be used at low temperature to replace

these ammonia molecules with water ones after the adsorption step. The h-band, on the other hand, is the consequence of ammonia desorption from true acidic centers. The temperature of maximal desorption rate is influenced by several factors, such as intrinsic acid strength, acid strength distribution and amount, the structure and porosity of the materials and particular experimental factors[85]. TPD of ammonia is sometimes limiting if not coupled with other techniques, since it does not allow distinguishing between desorption from Brønsted or Lewis sites. To overcome this drawback, the combination with infrared spectroscopy (IR) has proven to be very effective. Infrared spectroscopy (IR) is a powerful technique that allows determining the abundance and type of acid sites, either using specific molecular probes or by limiting the analysis to the pure sample. The abundance of acid sites can be estimated through the integration of particular bands in the IR spectrum and the exact position of these is correlated to the relative strength and nature of acid sites. IR performed without the use of probe molecules deals with vibrations of OH groups and can be exploited to assess for instance the silanol groups population. Wavenumbers associated to O-H stretching inform about the different types of hydroxyl groups in the material. Vibrational modes of O-H can be altered by the position of the group[86], terminal, bridging or by geometric distribution of atoms surrounding the bond (related to the materials structure). Brønsted acid sites in zeolites for instance ($\equiv Si-(OH)-Al\equiv$) vibrate at 3450 and 3550 cm^{-1}. Terminal silanols ($\equiv Si-(OH)$) can be found as external surface hydroxyls (3740-3745 cm^{-1}) or as defect framework sites. The vibrational modes of defect sites depend strongly on the local characteristics of the lattice. Hydrogen bridging interactions shifts hydroxyl bands to lower frequencies, usually below 3500 cm^{-1}. Isolated silanols appear between 3715 and 3735 cm^{-1}[83]. Of major importance, in the determination and discrimination of acidity in metal-substituted materials, is the utilization of IR spectroscopy of adsorbed molecules. The specific information on acidic sites can be obtained by taking advantage of the specific acid-base interaction of acid sites with the chosen probe molecule. Among these, pyridine is excellent because it interacts with Brønsted acid sites to produce pyridinium ion ($PyrH^+$) that is characterized by a very different adsorption band if compared to pyridine coordinatively bonded to Lewis acid sites. In the case of Al-MCM-41 it was possible to discriminate bands due to hydrogen bonded pyridine (1445 and 1596 cm^{-1}), strong (1623 and 1455 cm^{-1}) and weak (1575 cm^{-1}) Lewis bound pyridine, pyridinium ion vibration assigned to pyridine bound

to Brønsted acid sites (1546 and 1639 cm^{-1}) and a band at 1492 cm^{-1} which can be assigned to pyridine associated with both Brønsted and Lewis sites[87]. Another option is represented by carbon monoxide, widely used because of its mild acidity and its small size. The advantage of CO is its sensitivity to almost every acidic site not only in zeolite materials but in several oxides[88–90]. It has been speculated that the free electron pair on carbon atom confers to CO the basic character. CO has also been used in the determination of coordination numbers in metal ions. The interaction is much stronger with tetrahedral sites (e.g., framework aluminum) compared to octahedral sites (e.g., extra-framework aluminum). FT-IR of adsorbed ammonia is another example on how IR spectroscopy can be a powerful tool in the characterization of the acidic properties of solids since it allows differentiation between Lewis and Brønsted acid sites with respect to their type and strength, especially if this method is combined with *in situ* TPD studies. The absorbances at 1620 and 1300 cm^{-1} in the spectra of ammonia-loaded samples are assigned to bending modes of ammonia coordinated to Lewis sites[48]. According to the results obtained on zeolites, the vibration bands at 1620 and 1330 cm^{-1} refer to ammonia bound to weak and strong Lewis sites, respectively[91, 92]. The vibration band of ammonium ions at Brønsted sites appears at 1450 cm^{-1}. Such studies have already been performed on aluminum-rich and silicon-rich zeolites, revealing that the FTIR study of ammonia is of general application over the whole Si/Al range observed in different types of zeolites. The use of even different molecules on the same sample has been successfully exploited to determine the acid site distribution, since not all acid sites are reactive towards a particular probe, or the probe cannot access all of the acid sites because of geometric constraints. An additional fruitful approach for the study of acidity that deserve to be mentioned, consists in the adsorption of probe molecules during solid state NMR experiments. The most important probes are: pyridine-D5, acetonitrile-D3, ^{2}C-2-acetone and trimethylphosphine. In a standard experiment, a portion of the material is saturated with the chosen molecule; this interaction induces displacements of ^{1}H NMR signals of the materials and of the probe (^{13}C, ^{15}N, ^{31}P, etc.). The size, basic strength, flexibility and shape of the molecule under use determines the type of acid sites that can be investigated[83]. In the assessment of acidic sites located only on the external surface of zeolites H-ZSM-5, perfluorotrimethylamine (kinetic diameter ca. 0.94 nm[93]) has been used taking advantage of its too bulky diameter to enter the internal porosity

of 0.55 nm. This molecule is sensitive only to acid sites located to the external surface[94]. After saturation with this molecule, silanols and Brønsted acid sites signals that originally appeared at low ppm are shifted high by 0.25 and 0.47 ppm, respectively, indicating the location of such hydroxyls on the outer surface of the crystal or in secondary mesopores[93, 95]. Pyridine is another extensively used probe. Pyridine adsorption on bridging O-H groups generally occurs by full protonation ($PyrH^+$). ^1H magic angle spinning (MAS) NMR signals of deuterated pyridine adsorbed on zeolite materials are found at 10 ppm whenever hydrogen bridges with surrounding silanols are formed, and at 12-20 ppm for $PyrH^+$, formed on Brønsted acid sites. Another molecule of common usage is ^{13}C-2-acetone[96, 97]. Biaglow et al. measured ^{13}C signals of the carbonyl group after acetone adsorption on a series of zeolites with different acid properties[96]. Their results showed that carbonyl signal on H-SAPO-5 came about 216.8 ppm (referred to TMS); on HeY, the signal appeared at 219.6 ppm; on H-MOR, at 221.8; on H/Ga-MFI, at 222.8; on H-ZSM-12, at 223.4; on H-MFI, at 223.6; and on H-ZSM-22, at 225.4. One way to interpret these results is to compare them with the chemical shifts found for acetone dissolved in chloroform (205 ppm) and in 100% sulfuric acid (245 ppm)[98]. The lower chemical shifts correspond to milder acidic sites, with a limiting value at 205 ppm. In this acidity scale, acid sites of H-MFI are as acid as 80% sulfuric acid[99]. The main limitation of acetone as a probe relies on the by-reaction that may occur on very acidic sites to yield mesityl oxide. Deuterated acetonitrile has recently been put in the lightspot since it can be studied quantitatively by ^1H MAS NMR[100, 101]. Acetonitrile interacts by hydrogen bridging, with consequential displacements of the signals originally appearing at low ppm. The larger displacement in Brønsted acid sites signals after the saturation step, corresponds to the higher acid strength. These resonance displacements induced by adsorption have been measured for a number of zeolites (H-X; HeY; Al,Na-X and HUSY), showing strong correlations with results afforded from other methods[100, 102].

1.7 Characterization of silica matrix via solid state NMR

Solid state NMR spectroscopy finds many applications in the characterization of solid materials, allowing the investigation of both bulk and surface

structure[103]. In catalysis science, the characterization of active centers on the catalyst surface is of key importance, unveiling the relation between catalysts structure and surface reactivity. This includes the detection of acidic or basic sites, as discussed in the previous section, and elucidation of the structure, oxidation state or coordination environment of active species. Solid-state NMR spectroscopy is widely used not only in probing crystalline solids but is particularly advantageous when studying amorphous or weakly crystalline materials, as it is most sensitive to the short- to medium-range order of the structure. For this reason, it can be used in combination with methods such as X-ray diffraction and high-resolution electron microscopy to provide complementary information[104]. Silica-based solids are among the most extensively employed materials in catalysis; either used as support for catalytically active species or as the catalyst itself. To avoid the difficulties in spectral analysis of broad and overlapping anisotropic line shapes, most of the solid state ^{29}Si NMR work is done by use of the magic angle spinning (MAS) technique which averages the distinct components of the chemical shift anisotropy tensor to the single mean value of the isotropic chemical shift. A review of ^{29}Si NMR of inorganic solids was published by Engelhard and Koller[105]. The most direct and rather fundamental information which follows immediately from the number of distinct resonances observed in the ^{29}Si MAS NMR spectrum is the number of chemically inequivalent Si sites present in the sample. Moreover, from the normalized peak intensities the relative populations of the various sites can be determined. The number of inequivalent sites that can be distinguished in the spectra depends on the relationship between spectral resolution (line width) and chemical shift difference between the distinct sites. For highly crystalline samples as zeolites with well-ordered structure usually very narrow lines are observed, and subtle differences in the structural surrounding of the corresponding Si sites may be detected. In contrast, amorphous, samples with highly disordered structures show, in general, broad and overlapping resonances making the interpretation of the spectra difficult. However, those spectra may be analyzed by deconvolution and line fitting procedures. As an example, Figure 1.7 displays the ^{29}Si MAS NMR spectrum of a silica-based mesoporous catalyst. The broad spectral pattern evidenced in light red (right) can be clearly separated into three resonances corresponding to three different Si environments. The vast majority of silicates and other inorganic silicon compounds contain four-fold coordinated silicon but a number of structures with five- and six coordinated Si are known. Values between - 60 and -120

ppm are typical of four-coordinated SiO_4 in silicates [106], the resonances of octahedral SiO_6 coordinations, as observed, e.g., in thaumasite, stishovite[107], perovskites and other high-pressure silicate minerals, appear in the range between -170 and -220 ppm. The ^{29}Si MAS NMR spectrum of a methyl functionalized silica-based mesoporous catalyst presented in Figure 1.7, can be an interesting example to analyze. The signal centered at around -100 ppm, evidenced in light red, is assigned to silicon atoms in the silanediol groups, silanol groups, and silicon-oxygen tetrahedra of the SiO_2 framework, respectively. In other words, to silicon-oxygen tetrahedra Q^2 $[(SiO)_2Si(OH)_2]$, Q^3 $[(SiO)_3SiOH]$, and Q^4 $[(SiO)_4Si]$ where the superscript indicates the number of siloxane bonds. The respective proportion of this contribution, measured by quantitative Direct Excitation ^{29}Si MAS experiments, is used to collect information on the degree of condensation of the silica matrix and on the population of surface silanols present on the surface. Moving from a purely siliceous matrix to a functionalized silica matrix may be very important to many research and technology fields and ^{29}Si MAS NMR again has been shown to be a powerful tool for the characterization of silica surfaces and subsequent molecular grafting. The introduction for instance of organic groups on the surface of silica can be used to redesign surface properties. Specifically, silica nanoparticles can be grafted with siloxanes to obtain high specific surface area functional materials.

Mono- (M), di- (D), tri- (T), and quaternary- (Q) substituted silanes all have a particular chemical shift range in ^{29}Si NMR, and thus it is possible to assign NMR peaks in a corresponding spectrum to these structural details. An example is presented in Figure 1.7, where a separated signal centered at around -70 ppm can be observed and assigned to T^2 and T^3 sites, ascribed to the presence of methyl groups grafted on silica surface. More recent extensions of these studies include the discrimination of internal and external hydroxyl groups in terms of both their chemical nature, local mobility, and proximity to trapped water[108], and also using ^{29}Si–^{1}H CP-MAS, to distinguish hydrogen-bonded silanols from non-hydrogen-bonded silanols[109]. Maciel and co-workers reported a study of the molecular dynamics of deuterated surface silanols using ^{2}H NMR. Modeling of the 2H lineshape allowed the possible motions of the hydroxyl bond to be identified[110]. ^{29}Si MAS NMR can thus provide detailed information on the local structure around the silicon atoms and is, therefore, a valuable complement to the X-ray or neutron diffraction techniques which monitor the periodic long-range order of crystalline materials. Second nearest neighbor effects on the ^{29}Si chemical shift has been particularly well studied for

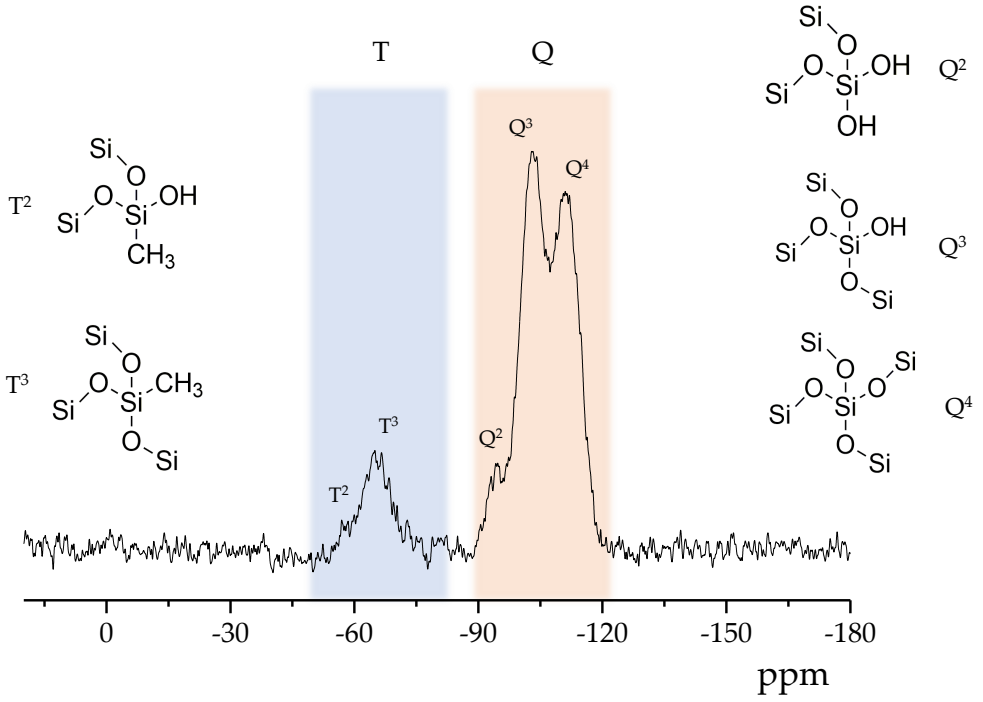

FIGURE 1.7: Direct Excitation ^{29}Si MAS NMR spectrum of a mesoporous methyl functionalized silica-based catalyst. On the right and left side, schematic representation of different silicon environments present in the bulk and on the surface.

silicates, aluminosilicates and related materials. There are especially two characteristic features which affect the ^{29}Si chemical shift of a SiO_4 group: characteristic high-field shifts are observed with increasing number of Si-O-T bridges (T = Si, Al..) formed by the SiO_4 tetrahedron (degree of SiO_4 polymerization), and typical low-field shifts follow from the replacement of Si with Al in the second coordination sphere of the central silicon with a given number of SiOT bridges (degree of tetrahedral Al substitution). Similar shift effects have been observed for tetrahedral Ga substitution in gallosilicates. Thus, the presence of the distinct types of structural units and, from peak intensities, their quantitative distribution in the structure can be determined from the ^{29}Si MAS NMR spectrum[105]. Solid state NMR spectroscopy is a powerful tool to investigate not only the silica matrix but also the coordination number/geometry of metal centers inserted as single site within the framework of solids. The understanding and (when possible) the quantification of different species is of fundamental importance since it allows to strongly correlate the final properties of the solids with the metal coordination. This aspect will be of fundamental importance and will be discussed more specifically across the different chapters of this manuscripts.

1.8 Developing better heterogeneous catalysts

The design of novel and more efficient heterogeneous catalysts is focused on the optimization of multiple characteristics as their texture or structure, nature and dispersion of the active sites, to operate on diffusion and reactivity aspects. The concept of improving a catalyst is shifting from a focus on increasing the rate of conversion of reactants to products to the importance of improving the selectivity of catalysts to promote the desired reactions in more sophisticated synthetic processes. In terms of more sustainable processes, selectivity not only reduces the consumption of reactants and facilitates the isolation of the targeted products, but also helps making industrial processes greener. At the first place, chasing always better performances, the nature and dispersion of the active sites dictating the desired reactivity have to be controlled precisely. In the case of heterogeneous catalysts where a finely dispersed metal on a high-surface-area support represents the active phase, not only the nature of the active phase but also the control of the particle size during the synthesis is critical. The challenge, for this kind of heterogeneous catalysts, is to disperse the colloidal nanoparticles on high-surface area supports and to activate them without losing the original size distribution[111]. Textural and structural features of solid catalysts are also important factors in controlling activity and selectivity. The porous structure of a catalyst can affects catalytic performance via control of the access of the reactants to the active phase or of the products to the outside environment. As already mentioned, the discovery of zeolites and ordered mesoporous materials are the most representative example of activity and selectivity control by engineering the shape of their pores. An alternative approach to develop better heterogeneous catalysts is the derivatization of solids, adding specific molecular functionality by anchoring specific molecules to the surface. A common example is represented by anchoring homogeneous catalysts onto the surface of porous materials. The heterogenization of homogeneous catalysts represents also a convenient way to handle catalysts, making their separation from the reaction mixture easier. This procedure can be used to prepare catalysts with two or more functions, such as acidic and basic sites, that usually are not be able to coexist in solution[111]. With the aim of improving both activity and selectivity, the efficient introduction of the desired active sites, their efficient dispersion and the precise tuning of the morphology of the solids can be combined with the control of adsorption/desorption phenomena

on the surface.

1.9 The key role of the surface governing adsorption/desorption phenomena

In heterogeneous catalysis, the surface of the solid plays a central role. On the catalytic surface, reactants are first physically adsorbed and this weak interaction is followed by the catalytic activation. This process leads to the formation of the desired product lowering the activation energy of the transformation. For this reason, the adsorption of reagents on the surface of the given catalysts is a key step. However, a too stable adsorption will hinder the crossing of the too high activation energy barrier, impeding the transformation and therefore poisoning the active sites. The most favorable case in heterogeneous catalysis is represented by a favorable balance between the adsorption of the reactants and release of the products from the catalytic surface, to allow the active catalytic site to initiate another turnover. Adsorption/desorption phenomena may also have consequences on the local reaction equilibrium at the surface of a heterogeneous catalyst, for instance, in the case of reactions yielding different co-products. If at least one of the co-products presents a weak interaction with the surface and is easily repelled to the bulk, the catalytic conversion is expected to increase. When dealing with consecutive catalytic reactions, not only conversion but also selectivity to the products of each step should be dependent from the respective strength of adsorption of these products. It is speculated that the long residence time of a product on the surface of the catalyst, originating from an intermediate step of a network of subsequent reactions, would lead to a higher probability for this product to be transformed in the subsequent step rather than desorbing to the bulk. These considerations converge in the importance of a fine control of both adsorption and desorption steps to improve the desired catalytic processes. The affinity and interaction of a molecule with the catalytic surface, impacting adsorption and desorption phenomena, can be adjusted modifying its chemical functions or modifying the catalyst surface. These kinds of surfaces modified catalytic systems should be able to process the new generation of feedstock coming from renewable resources and biomasses. This biomass-based industry requires catalytic systems able to transform a wide series of complex and highly functionalized substrates possibly at low temperature with a high selectivity. The catalytic

performances of these systems should be high even in aqueous media and ideally multistep processes should be replaced by one-pot cascade reactions. For this reason, there is a high valorization potential in developing advanced multifunctional materials able to promote different individual reactions within a multiple-step process. Polarity or more specifically hydrophilic/hydrophobic interactions, are definitely crucial when dealing with reactants and products presenting different functionalities and usually a systematic and careful approach is lacking in the literature despite many arguments suggest the presence of a tight link between hydrophilic-phobic character of catalysts and their performances.

1.10 The role of the hydrophilic/hydrophobic tuning to control catalyst activity and selectivity

Heterogeneous catalysis is constantly demanding the developments of more innovative and sustainable systems. In this panorama, only a minor effort is dedicated to the fundamental and systematic study of the role played by the hydrophilic and hydrophobic properties of the catalyst surface. The degree of hydrophilicity/phobicity strongly influences the interactions between the catalytic material and reactants, products or side reaction compounds and, as consequence, it determines the catalyst performances. It is known, for example, that in the case of a reaction yielding various co-products, the catalytic conversion and yields should increase when at least one of the co-products has a weak interaction with the catalyst surface and it is rapidly repelled from it. A careful tuning of the hydrophilic/hydrophobic balance of the catalyst surface may have a positive influence on the performances of the catalyst improving both activity and selectivity. This embraces especially catalysts based on ordered mesoporous materials, since due to their pore system with relatively narrow pores the reacting molecules are exposed to a local environment determined by the surface properties of these pores for a relatively long time. The hydrophobic/hydrophilic properties of the catalyst surface sometimes also have a strong influence on the catalytic activity and few examples may easily be cited. For instance, Gosselier et al. demonstrated the Pd/carbon nanofibers polarity in the dehydrogenation of fatty acids. In this work, the introduction of oxygenated

polar functions allows reducing the hydrophobicity of the support and this resulted in a beneficial effect on the activity. This can be explained due to the preferential adsorption of polar carboxylic groups of the fatty acid interacting with the more polar support[112]. The most well-known example for the effect of surface hydrophobicity is the olefin epoxidation over titanium-modified materials. Silylated mesoporous titanosilicates which are more hydrophobic compared to the unmodified silicas, have enhanced activity in olefin epoxidation[113–117]. When alkylhydroperoxides are used as oxidants, the substrates have to compete with water. An increase in activity is then expected for a more hydrophobic support, because the substrates are favored in the pore system and therefore gain easier access to the catalytically active titanium centers. Moreover, in Ti-MCM-41 with larger pores compared to zeolites, the alkylhydroperoxide can easily penetrate the mesopore system, reducing diffusion limitations or complete exclusion of the hydroperoxide. Not only activity but also selectivity may be influenced by surface hydrophobization. If we consider as an example the reaction pathway for cyclohexene oxidation, the desired epoxide can be obtained by two competitive paths. In the first path, called allylic oxidation, the formation of cyclohexenyl hydroperoxide is responsible for the oxidation of the olefin through a radical mechanism[118] (Figure 1.8, top). In the second path (Figure 1.8, bottom), the direct epoxidation of cyclohexene with H_2O_2 gives the desired product. The allylic oxidation path should be avoided since it leads to the concomitant formation of undesired side products (2-cyclohexen-1-ol and its oxidation product 2-cyclohexen-1-one). The mechanism implies the formation of a radical species on the Ti active site due to the over-adsorption of H_2O_2 on the catalyst surface, which is favored by a high H_2O_2/Ti ratio[118, 119]. It has been reported by Smeets et al. that increasing the surface hydrophobicity by introducing methyl groups on the surface of mesoporous SiO_2-TiO_2 catalysts may help reducing locally this ratio by repelling H_2O_2 molecules from the surface and thus from Ti active sites[117]. Consecutive to the formation of the epoxide, the ring opening of the epoxide to form a diol (cyclohexane diol) is another unwanted process. This hydrolysis reaction is promoted by the presence of H_2O and therefore thought to be mitigated by surface hydrophobization.

The role played by surface polarity in determining activity and selectivity is again evidenced in the acid-catalyzed dehydration of fructose into 5-hydroxymethylfurfural (HMF) by Karimi et al.[120], using sulfonic acids supported on organosilane-functionalized SBA-15 presenting different degrees of

hydrophobicity. In this reaction, in most of the cases, the selectivity to HMF could not be raised to maximize HMF production due to its further reaction to form by-products such as formic acid, levulinic acid and polymeric humins. The authors showed that a suitable tuning of the SBA-15 surface polarity was favorable for the fast departure of HMF from the pores, resulting in a higher selectivity to HMF. Considering the higher hydrophobic nature of HMF than fructose, it has been proposed that during the reaction HMF would be more favorably repelled out from the mesopores of less hydrophobic catalyst, thus retarding the rehydration of HMF to unwanted by products and improving the HMF selectivity. However, when the catalyst becomes more hydrophobic, the HMF molecules would settle inside the system pores of the catalyst to greater extent and further rehydrated in the presence of acidic sites, thus lowering the overall HMF selectivity. Another important example is represented by the acetalization of glycerol into solketal. Hydrophilicity is needed to favor glycerol adsorption on the surface of the catalyst in close proximity of the active sites. On the other side more hydrophobic surfaces help the removal of the water produced during the reaction. Elimination of water from the reaction mixture using a Dean-Stark apparatus was proved to have a beneficial effect on the catalyst's performances increasing the solketal yield. Silva et al reported an excellent conversion of glycerol to solketal over various catalysts and they attributed the good performance of the best solid to its relatively high hydrophobic nature[4]. It was proposed that the hydrophobic character of the material may be responsible for the elimination of the formed water molecules from the pores. Recently, it was found that USY and Al-TUD-1 display poor

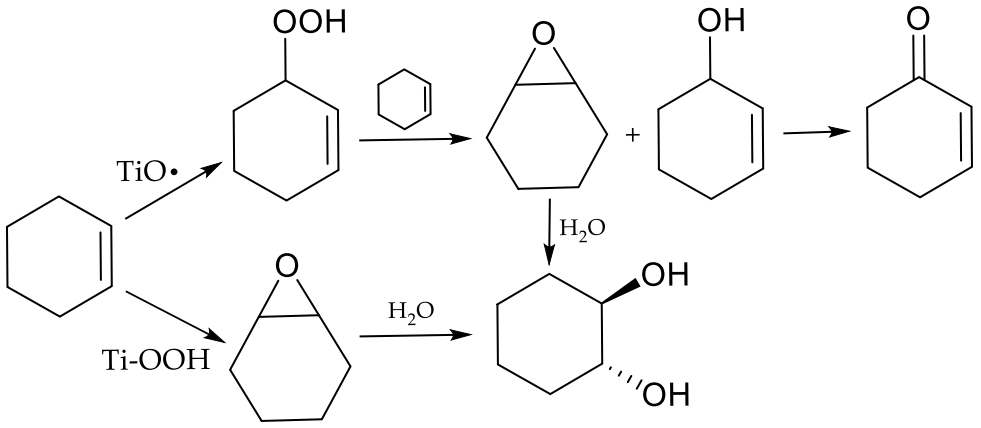

FIGURE 1.8: Reaction scheme for the epoxidation of cyclohexene via the allylic oxidation (top) or the direct epoxidation routes (bottom) adapted from[118].

catalyst performances in the conversion of glycerol to solketal[8]. The lower activity of USY and Al-TUD-1 based materials compared to other catalysts reported in the manuscript was attributed to their higher hydrophilic character.

1.11 The glycerol challenge

Recently, the interest of the scientific community moved toward green applications and in particular, in agreement with the directive of the Kyoto protocol, toward the reduction of the dependence from oil. Nowadays, the worldwide production of synthetic plastics is still mainly oil-dependent. Biomass conversion to chemicals represent one of the most promising green alternatives to the existing technologies and a possible answer to the increasing oil price as well as to the demand of sustainable feedstocks. Biodiesel is gaining a growing importance on biofuels market due to its good compatibility with commercial diesel engines. Moreover, increasing amount of biodiesel must be added to the traditional fuels in order to fulfil the requirements of the European commission in terms of energy and sustainability[121]. Biodiesel is produced via transesterification of vegetable oil or animal fat with methanol. The process yields, as by-product, an amount of glycerol approximately equivalent to 10 wt% of the total biodiesel produced[7].

The increasing production of biodiesel during the last years caused an oversupply of glycerol. The global glycerol market was 800000 tons in 2005 (400000 tons from biodiesel) in comparison to 60000 tons only in 2001[122]. The price of glycerol consequently suffered of a drastic decrease and nowadays it is even considered a waste. Consequently, growing efforts have been devoted to transform glycerol (and its derivatives) into valuable chemicals employing various catalytic processes. Glycerol is a highly functionalized molecule compared to other petrochemically produced hydrocarbons and much effort has been dedicated to investigate its catalytic conversion, including oxidation, dehydration, etherification, hydrogenation and esterification[124–127]. Glycerol can be employed in industrial fields related to pharmaceuticals, cosmetics, soaps and food (see Figure 1.9). More importantly, glycerol can also be considered as a low-cost raw material and its transformation into other valuable compounds has attracted great interest in the last few years[128]. Among all the possible glycerol derivatives, a special attention will be given in this work to alkyl lactates and solketal (Figure 1.10). Alkyl lactates present a great potential in

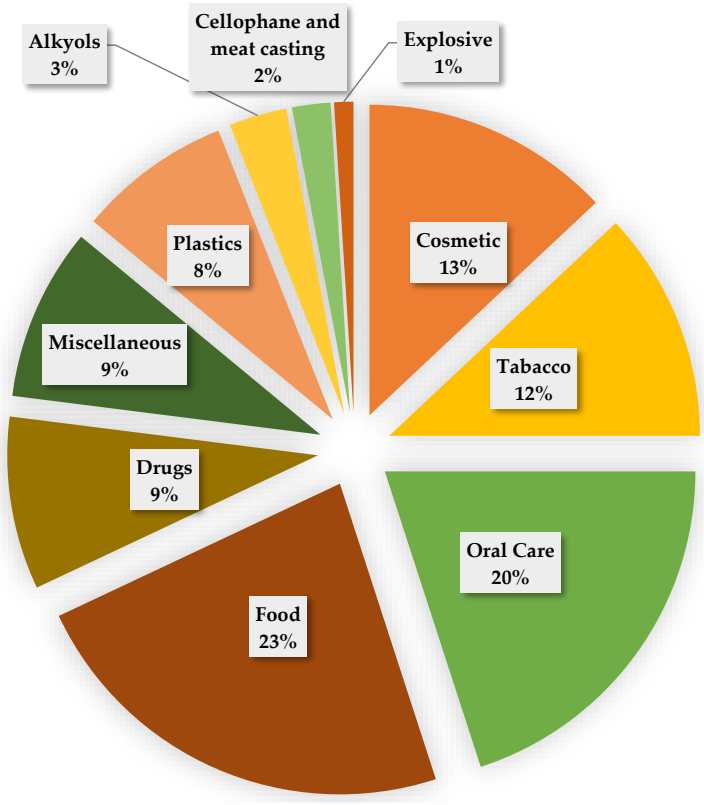

FIGURE 1.9: The market for glycerol in terms of volumes and industrial use. Data taken from[123]

the application as green solvents, precursors for the synthesis of polylactate, which is very actual as a biodegradable plastic material and in various other industrial areas related to chemicals, food, pharmaceuticals and cosmetic products[9, 10, 129]. The second product of interest derives from the condensation of glycerol with acetone. This reaction yields the compound known as solketal (2,2-dimethyl-1,3-dioxolane-4-methanol), which has direct applications as surfactant, flavouring agent and can be blended with gasoline or biodiesel as fuel additive to improve the cold flow properties reducing also particles emission[3].

1.11.1 Synthesis of alkyl lactates

Recently lactic acid and alkyl lactates attracted a considerable interest from both academic and industrial parties for the broad window of possible applications ranging from green solvents and intermediates for the production

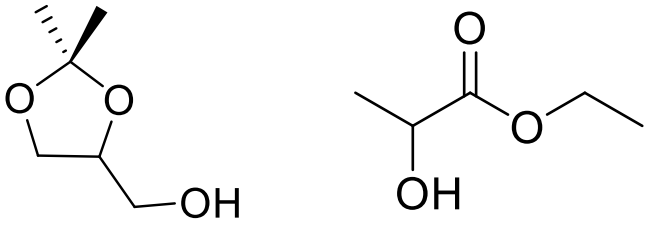

Solketal Ethyl Lactate

FIGURE 1.10: Molecular structure of solketal and ethyl lactate

of chemicals to pharmaceuticals and cosmetic products[9, 10, 129, 130]. Several feedstocks have been used for the production of alkyl lactates including glycerol, cellulose, glucose, fructose and trioses[131]. Trioses, such as dihydroxyacetone (DHA), can be obtained from glycerol via catalytic oxidation or fermentation. The subsequent synthesis of alkyl lactate from DHA and alcohol is the subject of intense research efforts. Homogeneous catalysts, as transition metal halides, are typically highly active in this transformation. However, the intrinsic toxic and corrosive nature of this reagents make them less attractive in the optics of green chemistry and environmentally friendly processes. More recently, a remarkable number of Sn-based heterogeneous catalysts were reported as better candidates for a more sustainable and greener conversion of trioses to alkyl lactates, including zeolites (MFI, USY, Beta)[68, 132–134], Sn-MCM-41[12, 135], and silica-carbon composites[136]. Taarning et al. synthesized and evaluated the activity of a series of metal-containing Beta zeolites (M = Al, Zr, Ti, and Sn) in the conversion of DHA in methanol[68]. For comparison, they also prepared purely siliceous Beta zeolite and the corresponding oxides, aiming at clarifying the importance of the metal atoms. Sn incorporated zeolite Beta was the most active, fully converting DHA into methyl lactate at 80 °C; while for the other zeolites, to reach the complete conversion, an increase in the temperature to 125 °C was necessary. The authors correlated the catalytic activity of these metal containing zeolites to the bond strength between the metal and the carbonyl group, Sn being the strongest in their series. The high selectivity towards the formation of dimethyl acetal of pyruvic aldehyde over acidic ion-exchanged resins and Al-Beta, which mainly contains Brønsted acid sites, allowed to consider that strong Brønsted acid sites are selective towards the formation of dimethyl acetal of pyruvic aldehyde, whereas Lewis acid sites are selective for the formation methyl lactate. Although Sn-Beta was quite active in such reaction, its long synthesis time and the use of hazardous fluoride media during the synthesis reduce the sustainability of the process.

Therefore, in 2010, the same group reported the synthesis of methyl lactate from DHA by employing commercially available solid acids, including zeolites of the type H-USY, H-Beta, H-ZSM-5 and H-MOR, sulphated zirconia and H-montmorillonite[68]. Pescarmona et al. investigated different commercial available USY zeolites with a broad range of Si/Al ratios, with the purpose of elucidating the type and strength of the zeolite acid sites and their contributions in the reaction pathway[132]. The authors concluded that a combination of strong Lewis acid sites and weak Brønsted acidity is crucial for obtaining excellent DHA conversion and selectivity towards the desired lactate. Strong Brønsted acid sites are detrimental because they favor the formation of diethyl acetal of pyruvic aldehyde. As well, higher temperature and extended reaction time are also beneficial for the reaction, because alkyl lactate is more thermodynamically stable. Recently, de Clippel and Dusselier et al. reported the preparation of a carbon-silica composite material with well-balanced Lewis and Brønsted acid sites and its promising activity in the conversion of DHA into ethyl lactate[136]. This hybrid material consists of a porous (polyaromatic hydro) carbon network introduced into the pores of a mesoporous Sn-MCM-41. In this material, Lewis acid sites are generated from Sn (IV) and Brønsted acidity is derived from the intraporous carbon, which is decorated with various surface oxygen-containing functional groups (like phenols, anhydrides, and carboxylic acids). The amount and strength of Brønsted acid sites were controlled by the carbon deposition content, the pyrolysis temperature, and thermal post-treatment[136].

The conversion of trioses into alkyl lactate has been intensively investigated over both homogeneous and heterogeneous catalysts. It emerged that the most crucial factor to reach high conversion and selectivity towards lactates is a combination of mild Brønsted acid sites and Lewis acid sites. Brønsted acid sites catalyze the initial dehydration of triose sugars into pyruvic aldehyde, and Lewis acidity is responsible for the isomerization of pyruvic aldehyde or its hemiacetal into the desired alkyl lactates (Figure 1.11). Strong Brønsted acidity is detrimental to the reaction by driving the reaction towards the side-products, thus decreasing the selectivity. The Lewis acid catalyzed step has been described either as an internal Cannizzaro reaction or as a Meerwein-Ponndorf-Verley reduction and Oppenauer oxidation (MPVO) reaction[68]. The amount and strength of both Lewis and Brønsted acidity is of major importance in determining the catalytic performance in the synthesis of alkyl lactates. For this reason, the design of efficient catalytic systems is strictly related

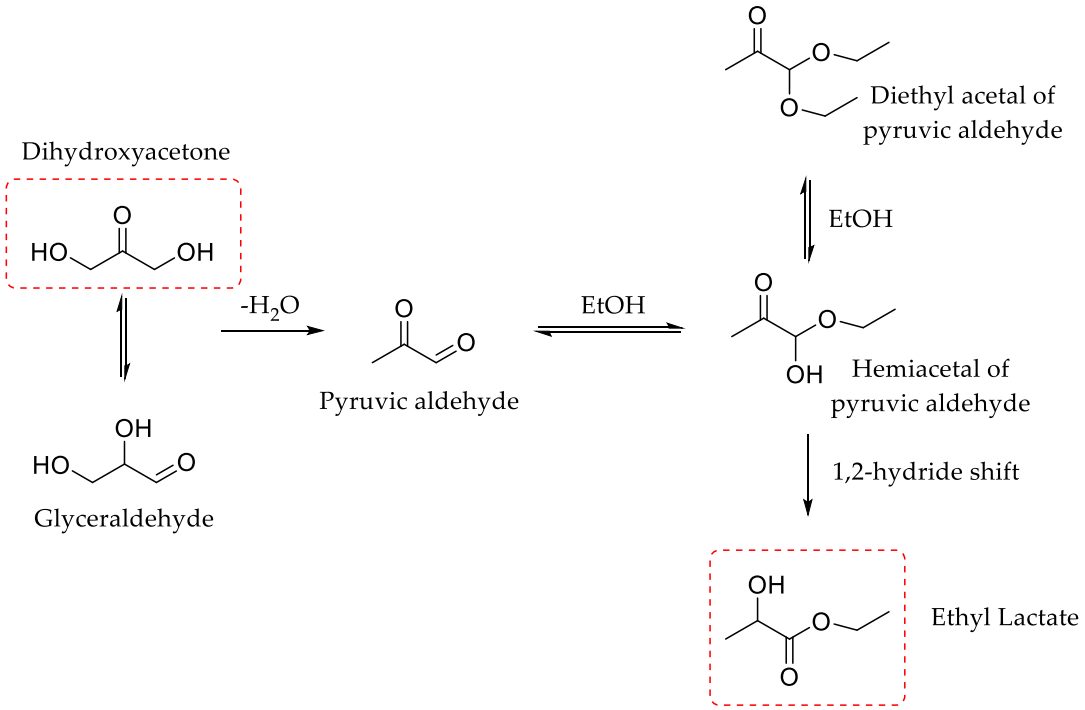

FIGURE 1.11: Proposed reaction mechanism for the production of ethyl lactate from dihydroxyacetone and ethanol

to the optimization of the balance between these two acid sites.

1.11.2 Synthesis of solketal

The condensation of glycerol with acetone could yield both the five- and the six-membered ring isomers, whose relative formation depends on the acetalization position within the glycerol molecule. The acetalization reaction is usually performed in the presence of large amounts of strong homogeneous Brønsted acid catalysts. Very expensive iridium complexes have also been reported to be active homogeneous catalysts for this reaction[137]. All these methods, based on homogeneous catalysis, present relevant drawbacks derived from the use of non-recyclable reagents and from the necessity of neutralization of the strongly acidic media, with the production of undesired wastes. The sustainability of this process can be substantially improved by substituting the homogeneous catalysis with the heterogeneous one. Recently, Amberlyst resins, zeolites, K-10 montmorillonites, sulfonic mesostructured silica, and silica-supported heteropolyacids were reported as active catalysts for this reaction[138]. The activity of these heterogeneous catalysts has been generally ascribed to the presence of Brønsted or to a combination of Brønsted/Lewis

acid sites[8]. Clarkson et al. studied the continuous synthesis of solketal by employing a sulfonic acid-functionalized ion-exchange resin, Amberlyst DPT-1, as the catalyst[139]. The catalytic test was carried out at 70 °C, an optimal temperature for maintaining the acetone concentration in the liquid reaction mixture and full conversion was achieved after 4 h of reaction. In order to save the cost of the raw materials, the conversion of aqueous glycerol (glycerol containing 20 wt% of water) was also tested. In order to achieve the complete conversion, a ramped temperature profile was applied. In this way, the same effect can be obtained by varying the temperature profile rather than by prolonging the reaction time. Another arenesulphonic acid polymer, Amberlyst-36, which contains large pores and high number of acid sites, was studied by Deutsch et. al. in 2007[5]. Although the reaction was performed at quite low temperature (40 °C), high yield of solketal was still achieved. This is most likely attributed to the continuous removal of water with a Dean-Stark trap. However, the use of the hazardous dichloromethane as solvent makes this process less environmentally recommended. The utilization of a hydrophobic catalyst might be an alternative way to increase the yield without using any hazardous solvent. Indeed, the use of zeolite Beta, with Si/Al ratio of 16, led to a conversion of over 95% within 60 min of reaction time[4]. Its hydrophobic character, due to the high silicon content, assists the removal of the formed water from the active sites and displaces the equilibrium concentrations towards the products. Vicente et al. reported the catalytic activity of a series of sulfonic acid-modified mesostructured silicas in this reaction in 2010[7]. The preliminary screening of the catalysts revealed that in a batch test, arenesulfonic acid-functionalized silica (Ar-SBA-15) outperformed other silicas (83% of solketal yield after 30 min of reaction at 70 °C with an acetone/glycerol ratio of 6). Ar-SBA-15, even with a much lower acid site concentration, displayed a comparable conversion as those achieved by the resin Amberlyst-15 (85% after 30 min).

Another well-known acid material, heteropolyacid (HPAs) with the Keggin structure, has been identified as a highly active catalyst in various acid-catalyzed reactions. However, HPAs have some disadvantages, such as low thermal stability, low specific surface area, separation problem from reaction mixtures and solubility. Ferreira et al. investigated several silica-immobilized HPAs and the sample prepared from tungstophosphoric acid was the most active one, getting a full conversion after 4 hours of reaction[140]. Figure 1.12 illustrates the mechanism of the condensation of glycerol with acetone over Brønsted acid sites, in which the selective formation of the five-membered

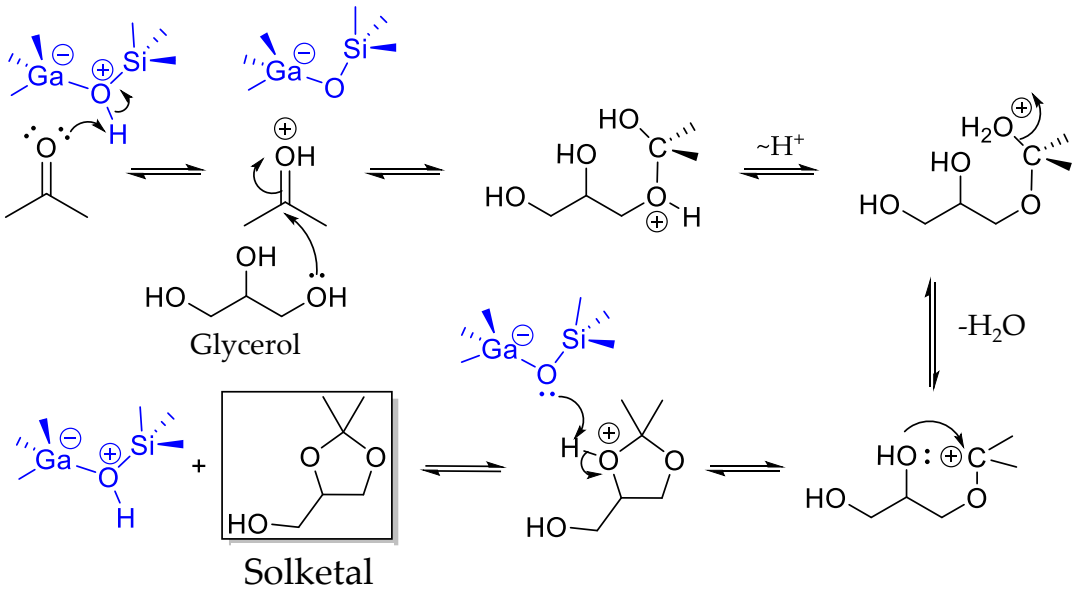

FIGURE 1.12: Schematic reaction mechanism for the condensation of glycerol with acetone into solketal over a Ga-silicate catalyst presenting Brønsted acid sites

solketal is achieved through a pathway involving a short-lived carbenium ion intermediate. Upon the formation of hemiacetal via the acetalization of glycerol, the dehydration yields a tertiary carbenium ion. The carbenium ion is stabilized by resonance with the non-bonded electron pairs of the adjacent oxygen atom. Then, the secondary hydroxyl group of glycerol promotes a nucleophilic attack and solketal is then formed. Compared to hemiacetal, the lifetime of the carbenium ion is much shorter and thus the system favors the production of the less thermodynamically stable five-membered ring transition state.

Setting the Objectives

The previous sections guide across the connection between the importance of developing novel metal-substituted porous silicates catalysts and the growing interest in the application of these tailored solids in the valorization of renewable resources and biomasses. In this context, sol-gel chemistry demonstrated to be a powerful tool providing a wide range of parameters that can be tuned to exactly tailor structural and textural features of a catalyst. It is evident that exploring new routes for the design of robust and active catalysts for these applications became a very actual and relevant research field. With the aim of improving both activity and selectivity, not only the efficient insertion of metals and the precise tuning of the morphology are important parameters to control but they can be combined with the control of adsorption/desorption phenomena on the surface. The degree of hydrophilicity/hydrophobicity can strongly influences the interactions between the catalytic material and reactants, products or side reaction compounds and, as consequence, it determines (directly or indirectly) the catalyst performances. Polarity are definitely crucial when dealing with multifunctional molecules and usually a systematic and careful approach is lacking. There is definitely place for a systematic and structured approach to take advantage of the underestimated relation between activity and hydrophilic-phobic character of a catalyst.

Guided by the above-mentioned concepts, this thesis grows around two main objectives:

1. Exploring advanced sol-gel techniques for the synthesis of porous silicates embedding Sn and Ga as single-site to be used as efficient catalysts in the upgrade of glycerol

This first objective will target an upgrade of knowledge in the vast panorama of metal-substituted silicates, proposing **advanced sol-gel techniques**. Different aspects deserve to be studied with the aim of precisely assess, design and

tune the materials textural and chemical properties and investigate their impact on the catalytic performances. To face one of the major drawbacks and weak aspect of heterogeneous catalysis, represented by diffusion limitations of substrates and products, considerable efforts are devoted to the design of catalysts able to enhance the accessibility of highly dispersed active centers. In this context, an important aspect to explore is the **influence of the catalyst morphology and porosity on its catalytic activity**. This first objective will be approached presenting original sol-gel synthetic routes that allow to obtain unique morphologies and to control structural and textural properties. Not only morphology but also a controlled dispersion of active sites is needed to produce highly active and selective catalysts. In particular, porous silicates embedding Sn and Ga, partially substituting silicon in their framework, have been reported as active and selective catalysts for the conversion of glycerol and its oxidation derivative (dihydroxyacetone) to solketal and ethyl lactate respectively. The acetalization reaction is typically catalyzed by Brønsted acids, though metal-substituted mesoporous silicates displaying mainly Lewis acidity have also been reported as promising heterogeneous catalysts for this reaction. In the conversion of trioses such as dihydroxyacetone, obtained from glycerol via catalytic processes, to ethyl lactate, a combination of Brønsted and Lewis acidity, with the former promoting the dehydration of dihydroxyacetone to pyruvic aldehyde, and the latter catalyzing the rearrangement of this intermediate to ethyl lactate is needed. **The precise control on the efficient insertion of metal elements as single site** in the silica framework, using a one-pot approach, and the tuning of the acidic properties can be obtained mastering the synthetic conditions. This challenge will be tackled as well in combination with the control of the morphology.

2. Studying the impact of the hydrophobic/hydrophilic balance of the catalyst surface on the performances

Many works reported in the literature impute to polarity a key role in the context of heterogeneous catalysis. However, often the relation bridging polarity and catalytic activity rests on assumptions and speculations lacking of a systematic and careful approach. In the perspective of developing better heterogeneous catalysts, improving both activity and selectivity, the efficient insertion of metals and the precise tuning of the morphology can be combined with the control of adsorption/desorption phenomena on the surface. Since the affinity of reactants and products with the catalytic surface can be

guided by hydrophilic/hydrophobic interactions, the aim of the second part will be devoted to the **deep understanding of the impact of the hydrophobic/hydrophilic balance** on the catalytic activity. This goal can be achieved only via the selective tuning of the surface properties. The control of surface polarity, achievable with a proper surface functionalization, could be use as a powerful tool for the optimization of the global efficiency of the catalysts. This approach will create the basis for a more ambitious goal (from an applied point of view), that is to synthesize more robust catalysts able to work under solvent free conditions hence avoiding the use of polluting solvents and at the same time allowing performing the reaction in presence of crude biomass-derived substrates usually presenting high amount of water.

Thesis Outline

In light of the above objectives, this manuscript will be structured around two main parts and five chapters. Each chapter can be considered independently and it will deal with one or both objectives.

To the first chapter has been dedicated the whole first part of the manuscript. The influence of the catalyst morphology and porosity on its catalytic activity in the upgrade of glycerol will be addressed proposing a straightforward one-pot sol-gel approach for the controlled preparation of novel 1D nanotubes presenting Sn inserted as single site in the structure. In the broad series of porous silicates, the controlled preparation of nanotubes constitutes a recent advancement. In 1999, Harada and Adachi reported a sol-gel method for the synthesis of single silica nanotubes or bundles through a surfactant-mediated template mechanism and they described the procedure for controlling the geometry of the tubes[42]. Earlier research showed that mixtures of commercially available triblock copolymer surfactants of the Pluronics family, in the presence of a micelle swelling agent, are effective templates for the synthesis of silica nanotubes with adjustable inner diameter. In this chapter, the optimization of the synthesis parameters will be studied to obtain materials with tubular structure and very high surface area even in the absence of additional hydrothermal treatments hence further reducing the environmental impact of the synthesis approach. The isomorphic substitution of Sn within the silica framework is fundamental to confer the acidic properties for catalytic application. To assess the coordination environment of Sn in the structure, a deep characterization via ^{119}Sn solid state NMR under static conditions will be performed. In addition, the characterization performed using FT-IR of NH_3 dosages will allow a more in-depth study of the Brønsted and Lewis acidity balance, strictly related to the catalytic activity of the materials. Sn-silica nanotubes will be used to catalyze both the transformation of dihydroxyacetone into ethyl lactate and the conversion of glycerol into solketal, with a special attention to the sustainability of the

process working under solvent-free conditions. The enhanced accessibility of their active sites given by their tubular morphology and the suitable combination of acid sites is expected to enhance their catalytic performance compared to the already reported metal-silicates presented in the literature. Moreover, the solids will be tested in multiple catalytic cycles and characterized to prove their stability in terms of textural properties and active sites under the selected reactions conditions.

The second chapter will open the second part of this work, where another advanced sol-gel technique for the synthesis of Sn and Ga-substituted porous silicates will be explored and used to tune their textural and chemical properties. The incorporation of catalytically active elements by co-synthesis using sol-gel approaches is widely used, however a key parameter is represented by the homogeneity of the synthesized solid catalysts. For example, the true incorporation of Al or Ti atoms in a silica network generates dehydration activity in aluminosilicates[141] or epoxidation activity in titanosilicates[142, 143]. In biomass conversion, isolated sites of Sn oxides in silica catalyze important reactions like glucose isomerization or alkyl lactate synthesis[135, 144]. An aerosol-assisted sol-gel process[145, 146] has emerged recently as an innovative, versatile and effective way to produce nanostructured porous catalysts exhibiting new properties[147]. In this synthesis process, the condensation of the inorganic network occurs during a short drying time, along with the evaporation-induced self-assembly of surfactant molecules. The method allows the formation of spherical particles with calibrated porosity and with a precise control on the composition and homogeneity of complex formulations. Of particular interest is the possibility to run this process in a continuous mode and scale it up relatively easily to industrial scale. In this chapter, taking advantage of this process, we present the synthesis of novel mesoporous tin silicate catalysts prepared selecting two different Si/Sn ratios. Small particle size and controlled porosity will be targeted as well as the insertion of Sn as single site in the silica matrix to brought about the desired combination of Lewis and mild Brønsted acid sites. After a complete characterization the materials will be tested as catalysts for the direct conversion of dihydroxyacetone to ethyl lactate to possibly highlight the positive effect dictated by texture and particle size as well as Sn speciation.

In the perspective of combining together both the objectives declared above, the next chapter will be dedicated to the development of a straightforward

one-pot procedure to synthesize a series of methyl-functionalized Sn-silicates with different degrees of methylation using the aerosol-assisted sol-gel process. In this third chapter, among the various parameters that can be optimized to design more efficient catalysts, the often underestimated parameter represented by the hydrophilic hydrophobic balance of the catalyst surface will be investigated. A complete characterization of the solids will assess the successful incorporation of isolated Sn as single site via ^{119}Sn solid state NMR measurements, while ^{29}Si and ^{13}C solid state magic angle spinning NMR experiments will reveal the degree of methylation, hence proving the efficacy of the adopted co-synthetic approach. In the context of alkyl lactate production from dihydroxyacetone, it was hypothesized by Lari and coworkers[148] that the lower interaction of water with the zeolite surface of hydrophobic Sn-MFI and Sn-BEA favor a shift of the dehydration equilibrium towards the pyruvic aldehyde (PA) intermediate hence improving the dihydroxyacetone conversion and the selectivity. However, to the best of our knowledge, a systematic investigation of role played by the hydrophobic/hydrophilic properties of the catalyst surface on this reaction was never performed. A systematic approach will be adopted in this chapter to investigate the tunable hydrophilic/hydrophobic character of the catalyst surface as a possible tool to further boost the catalytic performance of these formulations in the conversion of dihydroxyacetone to ethyl lactate. Moreover, the efficient reuse of the heterogeneous catalyst as well as the possibility of an easy recovery of the reaction solvent, resulting in a low waste production protocol and low E-factor, will be targeted.

The versatility of the aerosol assisted sol-gel process lies in the possibility of handling easily complex formulations to tune chemical composition and texture of materials. On the way to fulfill the first objective, the insertion of gallium in the matrix of silica based structured solid will be attempted using again the aerosol process and different Si/Ga metal ratios will be selected. Mesoporous gallium silicates have also been exploited for a series of sustainable chemical processes including the synthesis of alkyl lactates and other valuable chemicals from glycerol and its derivatives. Nevertheless, its full potential may not yet have been exploited in the conversion of glycerol into solketal. Therefore, in the fourth chapter, the synthesized Ga-silicates will be tested in the synthesis of solketal from glycerol and acetone and compared to reference

metallosilicate catalysts reported in literature. In the synthesis of metallosilicate catalysts, a central pillar is represented by the investigation of the coordination number/geometry of the metal centers inserted as single site within the silica matrix. Describing and quantifying the different species is of fundamental importance since it is strongly correlated with the catalytic performance. A deep structural investigation on the synthesized Ga-silicates will be used to provide strong evidences of the relation between the nature of Ga species and their catalytic activity. The insertion of gallium as single site in the silica structure will be studied via challenging techniques as solid state ^{71}Ga MAS NMR and XPS using the Auger parameter.

The final chapter will try once more to consolidate and expand the knowledge on the impact of the hydrophobic/hydrophilic balance of the catalyst surface on the performances, moving the attention on the acetalization of glycerol into solketal. The acquired knowledge will be exploited for the synthesis of two series of functionalized mesoporous Ga-silicates. The surface of the materials will be modified using different alkyl-silanes in a one-pot procedure to study their influence on the catalytic performances as well as on the morphology. In the acetalization of glycerol hydrophilicity is hence needed to favor glycerol adsorption on the surface of the catalyst in close proximity of the active sites. On the other side more hydrophobic surfaces may help the removal of the water produced during the reaction. To support a systematic study, these materials will be tested as catalysts in the synthesis of solketal from glycerol at low temperature and under solventless conditions and compared to the non-functionalized analogues to eventually prove the beneficial role of surface hydrophobicity.

Experimental Section

This section gathers: (1) the detailed description of the characterization techniques that have been used to study the materials presented in this manuscript and (2) the most common reaction conditions that have been selected to test the catalytic performances of the synthesized materials in the two reactions of interest; the conversion of dihydroxyacetone into ethyl lactate and the acetalization of glycerol with acetone into solketal. The synthetic procedure, adopted for the preparation of the solids, is reported separately at the beginning of each chapter.

1.1 Structural and textural properties

Transmission electron microscopy (TEM) micrographs were acquired using an acceleration voltage of 80 kV on a Philips Tecnai 10 microscope. N_2 adsorption-desorption isotherms were acquired at 77 K with a Micromeritics Tristar 3000 volumetric adsorption analyzer. The samples were outgassed under reduced pressure at 150 °C overnight before the analysis. To calculate the specific surface area, the Brunauer–Emmett–Teller (BET) method was applied to the nitrogen ads./des. isotherms in the 0.05-0.20 relative pressure range. The mean pore diameter was determined from the adsorption branches of the isotherm using the Barrett-Joyner-Halenda (BJH) method. The total pore volume (Vt) was derived from the quantity adsorbed at a relative pressure of 0.99. The amount of metal in the catalysts was obtained by inductively coupled plasma optical emission spectroscopy (Optima 8000 ICP-OES Spectrometer). The samples were prepared digesting 10 mg of the material in a mixture of 100 µL of aqua regia and 600 µL of HF 48%. Powder X-ray diffraction (XRD) patterns were recorded on a PANalytical X'pert diffractometer with Cu Kα radiation (λ = 1.54178 Å).

1.2 UV–Vis, solid state NMR and X-ray photoelectron spectroscopy

Diffuse reflectance UV–Vis spectra were collected on a Varian Cary 5000 UV–Vis spectrophotometer equipped with a Harrick single-beam Praying Mantis diffuse reflectance collection system. The Si environment was studied by ^{29}Si Magic Angle Spinning (MAS) NMR. ^{29}Si NMR spectra were recorded at room temperature on a Bruker Avance-500 spectrometer operating at 11.7 T (99.3 MHz for ^{29}Si) using a 4mm CP-MAS Bruker probe. The sample was packed in a 4 mm zirconia rotor and measured with a spinning frequency of 8000 Hz. Quantitative ^{29}Si spectra were recorded using the following acquisition parameters: 300s relaxation delay, 3 µs (90°) excitation pulse, 52 ms acquisition time. Cross Polarization (CP-MAS) spectra were recorded using a 5 s relaxation delay and 5 ms contact time. The processing comprised exponential multiplication of the FID (Free Induction Decay) with a line broadening factor of 30 Hz, zero-filling, Fourier transform, phase and baseline corrections. The chemical shift scale was calibrated at room temperature with respect to a sample of solid 3-(Trimethylsilyl)-1-propanesulfonic acid sodium salt (DSS) (0.0 ppm). The coordination of Sn atoms was studied by ^{119}Sn static NMR. The spectra were recorded at room temperature on a Varian VNMRS-400 spectrometer operating at 9.4 T (149 MHz for ^{119}Sn) using a 10 mm wideline probe. The sample was packed in a 10 mm Kel-F tube and studied in static condition. ^{119}Sn spectra were recorded using the Hahn echo pulse sequence and following acquisition parameters: 60 s relaxation delay, 3 µs (90°) excitation pulse, 5 ms acquisition time. The processing comprised exponential multiplication of the FID with a line broadening factor of 1000 Hz, zero-filling, Fourier transform, phase and baseline corrections. The chemical shift scale was calibrated at room temperature with respect to the isotropic shift of SnO_2 to -603 ppm[149]. The insertion of Ga in the silica matrix was studied by ^{71}Ga solid state NMR. MAS spectra were recorded at room temperature on a Bruker Avance-500 spectrometer operating at 11.7 T using a 2.5 mm Bruker CP-MAS probe. The solids were prepared in a 2.5 mm zirconia rotor and analyzed with a spinning frequency of 25000 Hz. The spectra were recorded using a Hahn echo sequence and the following acquisition parameters: a relaxation time of 0.3 s, an excitation of 2.6 µs (90°) and an acquisition time of 16 ms. Data processing includes the multiplication of the FID by a line broadening factor of 1000 Hz, zero-filling,

Fourier transformation and phase and baseline corrections. Fourier transformation from the echo maximum ensured a flat baseline with only zero-order phase correction. The chemical shift scale was calibrated at room temperature using $Ga((NO)_3)_3$ as the reference compound (0.0 ppm). X-ray photoelectron spectroscopy characterizations were carried out on a ThermoFisher ESCALAB 250Xi spectrometer, using a monochromatic Al Kα X-ray source (1486.6 eV) and a hemispherical deflector analyzer (SDA) working at constant pass energy (CAE). The diameter of the X-ray spot was set to 300 µm. The base pressure of the analyzer chamber was amounted to $2 \cdot 10^{-8}$ Pa. A flood gun, using electrons and Ar ions, was used to compensate for charges induced by photoemission. Survey spectra were recorded with a pass energy of 150 eV that was decreased to 25 eV for high-resolution spectra. Chemical components on photoemission spectra as well as Auger signals were fitted with Gaussian-Lorentzian lineshape. The Gaussian-Lorentzian (L/G) ratio, Full Width at Half Maximum (FWHM), kinetic energy and intensity (peak area) were adjusted during the procedure.

1.3 Characterization of surface acidity

Surface acidity was studied using NH_3-TPD and Fourier Transform Infrared Spectroscopy (FT-IR) of ammonia adsorption. In NH_3-TPD analyses, 50 mg of sample was introduced in a quartz reactor on a Hiden Analytical Catlab-PCS instrument. Prior to the analysis, the sample was treated in a dry air flow (30 $mL\,min^{-1}$) at 550 °C for 2 hours. Consequently, it was cooled down to 50 °C and then exposed to a gas mixture of 5% NH_3 in He (10 $mL\,min^{-1}$) and Ar (20 $mL\,min^{-1}$) for 45 min. Physisorbed NH_3 was evacuated by purging with Ar (30 $mL\,min^{-1}$) 90 min at 50 °C. The TPD analysis was performed by heating the sample from 50 to 650 °C with ramping rate of 5 $°C\,min^{-1}$. Desorbed NH_3 was detected using a mass spectrometer (QGA model). Brønsted and Lewis acidity was investigated by Fourier Transform Infrared Spectroscopy (FT-IR) of ammonia adsorption. FT-IR measurements were performed in transmission mode by using a Bruker Tensor 27 spectrometer equipped with a liquid nitrogen-cooled mercury–cadmium–telluride (MCT) detector, operating at 2 cm^{-1} resolution. Pre-treatments were carried out using a standard vacuum frame, in an IR cell equipped with KBr windows. The samples were pressed

into self-standing wafers and outgassed 1h at 400 °C before adsorption of ammonia at room temperature. Adsorption of ammonia was studied in the pressure range 0.01–20.0 mbar: the reversible fraction of the adsorbed ammonia was then removed by prolonged outgassing at room temperature.

1.4 Catalytic tests

Conversion of dihydroxyacetone into ethyl lactate: DHA (180.0 mg, $2 \cdot 10^{-3}$ mol), decane (25.0 mg, $0.2 \cdot 10^{-3}$ mol, GC internal standard) and absolute EtOH (3.92 g, 5.0 mL) were weighed inside a 25 mL glass vial. Then, DHA was dissolved in EtOH during 30 min at 50 °C under 800 rpm. Then, the catalyst was added to the mixture. The reaction mixture was heated at 90 °C under 1200 rpm. At the end of the catalytic test, the mixture was cooled down at room temperature and centrifuged (10 min, 4500 rpm). After, a sample of the supernatant was analyzed by gas chromatography on a Trace GC Ultra.

Recycling tests: In the case of non-functionalized solids, recycling tests were performed by separating the catalyst from the reaction mixture by centrifugation followed by sonication in ethanol (5 x 10mL). The catalyst was finally calcined in air at 500 °C for 2h (heating rate 1 °C/ min). Functionalized (methylated) solids were recycled using the above-mentioned washing procedure but adopting a thermal treatment in air at 300 °C for 4h (heating rate 1 °C/ min).
Leaching tests: DHA (90.0 mg, 0.001 mol) was dissolved in absolute EtOH (1.97 g, 2.50 mL) containing decane (13.9 mg, 0.0001 mol) at 50 °C for 30 min under 800 rpm stirring. Then, the catalyst was added and the reaction mixture was heated at 90 °C under 1200 rpm stirring. After 1 h, the catalyst was separated from the reaction mixture by hot filtration (around 90 °C). A sample of the filtrate (0.20 mL) was taken for GC analysis (diluted 5 times in EtOH prior to GC analysis). The filtrate was kept at 90 °C for another 5 h 30 min. A second GC analysis of the reaction mixture was then performed.

All the components for the conversion of DHA into EL were analyzed by Gas chromatography on a Trace GC Ultra from Interscience, with a polar column (phase: PH M-1, 0.5 µm, 5.0 m, 0.32 mm) using nitrogen as carrier gas at constant flow rate of 2.0 mL min^{-1}. The oven temperature was maintained at 50 °C for 2 min, then increased to 300 °C at 200 °C min^{-1} and finally maintained at 300 °C for 1.23 min.

Acetalyzation of glycerol into solketal: In a round bottom flask, glycerol (purity 99%, 921 mg, 0.010 mol), acetone (2.32 g, 4 equiv.) and the catalyst were added and stirred at 700 rpm at the desired temperature. After 6 h, the catalyst was separated by centrifugation and the reaction solution was analyzed by ^{1}H-NMR, using DMSO as deuterated solvent. 2,2-(dimethyl-[1,3]dioxan-4-yl)-methanol (solketal): ^1H-NMR (400 MHz, DMSO-d6): δ = 4.78 (1H, t, -OH), 4.03 (1H, m, -CH-), 3.94 (1H, dd, $-CH_2-CH-$), 3.63 (1H, $-CH_2-CH-$), 3.42 (1H, m, $-CH_2-OH$), 3.35 (1H, m, $-CH_2-OH$), 1.30 (3H, s, $-CH_3$), 1.25 (3H, s, $-CH_3$).

Recycling tests at 50 °C: In the case of non-functionalized solids, glycerol (1.84 g, 0.02 mol), acetone (4 equiv.), the catalyst (60 mg), were added and stirred at 50 °C for 4 h in a round-bottom flask. After this, EtOH was added to the reaction mixture and the catalyst was separated from the mixture by centrifugation (4500 rpm, 5 min). A sample of the supernatant was taken out, dried under reduce pressure and analyzed by ^{1}H-NMR. Then, the supernatant was carefully removed from the centrifuge tube and the catalyst was rinsed with EtOH and centrifuged (twice). After this, the catalyst was calcined in air at 550 °C for 2 h (heating rate: 2 °C min^{-1}). The subsequent catalytic tests were carried out by repeating this procedure from the beginning (the quantities were adapted in function of the mass of recovered catalyst). Functionalized solids were recycled using the above-mentioned washing procedure but adopting a thermal treatment in air at 300 °C for 4h (heating rate 1 °C/ min).

Leaching tests: In a round-bottom flask, glycerol (921 mg, 0.01 mol), absolute EtOH (0.70 mL) acetone (2.32 g, 4 equiv.) and the catalyst (0.025 g) were added and heated at 50 °C under 700 rpm stirring. After 1 h, the catalyst was separated from the reaction mixture by hot filtration (around 50 °C) and then centrifuged (4500 rpm, 5 min). A sample of the filtrate (0.4 mL) was dried under reduce pressure and analyzed by ^{1}H-NMR, using DMSO as solvent. The filtrate was kept at 50 °C for another 5 h. A second NMR analysis of the reaction mixture was then performed.

Part I

Chapter 1

Design and Catalytic Applications of 1D Tubular Nanostructures: Improving Efficiency in Glycerol Conversion

Abstract

A straightforward one-pot sol-gel approach for the controlled preparation of highly active 1D nanotubes is herein presented. The optimization of synthesis parameters allowed obtaining materials with tubular structure and very high specific surface area even in the absence of additional hydrothermal treatments hence further reducing the environmental impact of the synthesis approach. The isomorphic substitution of Sn within the silica framework was assessed via ^{119}Sn solid state NMR under static conditions. Sn-silica nanotubes were efficiently used to catalyze both the transformation of dihydroxyacetone into ethyl lactate and the conversion of glycerol into solketal, where outstanding turnover frequencies were obtained under solvent-free conditions. The catalytic performance of these materials is ascribed to the enhanced accessibility of their active sites given by their tubular morphology and to the suitable combination of acid sites. Moreover, no-leaching of active sites was evidenced and the best solid preserved its activity in multiple catalytic cycles. Characterization after the reuses allows supporting further the stability of Sn-silica nanotubes under the selected reactions conditions.

The results presented in this chapter have been published in:

L.A. Bivona [#], A. Vivian [#], L. Fusaro, S. Fiorilli, C. Aprile[*], Design and catalytic applications of 1D tubular nanostructures: Improving efficiency in glycerol conversion, Applied Catalysis B: Environmental, 247 (2019) 182-190.

[#] These authors contributed equally to this work

1.1 Experimental section

Synthesis of Si-NTs: Pluronic F127 ($EO_{106}PO_{70}EO_{106}$, $0.8 \cdot 10^{-4}$ mol, 1.0 g) was transferred in a capped PP container and dissolved in 2N HCl (60 mL) at 11 °C, under stirring at 250 rpm for 1 h. Then, TEOS (0.013 mol, 2.8 g) and toluene (3.0 mL) were added dropwise at 11 °C. The reaction mixture was stirred at 250 rpm for 24 h at 11 °C. The mixture was then treated hydrothermally for 24 h at 100 °C. The as-synthetized material (gel) was filtered, washed with Milli-Q water (600 mL) and dried at 65 °C in an oven overnight. The resulting white powder was calcined at 550 °C under air for 5 h (heating ramp 2 °C/min).

Synthesis of Sn-NTs-A: Pluronic F127 ($EO_{106}PO_{70}EO_{106}$, $0.8 \cdot 10^{-4}$ mol, 1.0 g) was transferred in a capped PP container and dissolved in 2N HCl (60 mL) at 11 °C, under stirring at 250 rpm for 1 h. Then, a solution of $SnCl_4 \cdot 5\ H_2O$ ($3.71 \cdot 10^{-4}$mol, 0.130 g, Si/Sn=37) in absolute ethanol (0.2 mL) was mixed with TEOS (0.013 mol, 2.8 g) and toluene (3.0 mL) and added dropwise at 11 °C. The reaction mixture was stirred at 250 rpm for 24 h at 11 °C. The mixture was treated hydrothermally for 24 h at 100 °C. The as-synthetized material (gel) was filtered, washed with Milli-Q water (600 mL) and dried at 65 °C in an oven overnight. The resulting white powder was calcined at 550 °C under air for 5 h (heating ramp 2 °C/min).

Synthesis of Sn-NTs-B: The same synthetic procedure as for the synthesis of Sn-NTs-A was followed with the exeption of the hydrothermal treatment. The reaction mixture was stirred at 250 rpm for 24 h at 11 °C and the as-synthetized material (gel) was filtered, washed with Milli-Q water (600 mL) and dried at 65 °C in an oven overnight. The resulting white powder was calcined at 550 °C under air for 5 h (heating ramp 2 °C/min).

1.2 Results and discussion

Sn-silicates with 1D tubular structure (Sn-NTs) were synthesized adapting a procedure previously reported for the preparation of silica nanotubes[150]. In order to achieve a successful incorporation of tin as single site in the silica architecture and avoid the formation of separated SnO_2 domains, the two inorganic precursors were simultaneously added dropwise to an aqueous solution of Pluronic F127 (see experimental section for more details). After reaction,

TABLE 1.1: Properties of Si-NTs-A and Sn-NTs-B materials

Entry	Material	Synthesis conditions	S_{BET} ($m^2\,g^{-1}$)	PD (nm)	Si/Sn
1	**Si-NTs**	24 h 11 °C + 24 h 100 °C	656	13	-
2	**Sn-NTs-A**	24 h 11 °C + 24 h 100 °C	763	15	133
3	**Sn-NTs-B**	24 h 11 °C	754	13	135

S_{BET}: specific surface area calculated from adsorption data in the relative pressure range of 0.05-0.20 p/p_0 for all materials; PD: pore diameter determined by BJH-KJS model; Si/Sn determined by number of moles of Sn calculated from ICP-OES analysis for the calcined materials; Theoretical Si/Sn ratio of 37

the mixture was subjected to hydrothermal treatment (HT) under static condition for 24 h (Sn-NTs-A). However, it was previously reported[12] that in some cases the HT could be avoided without detrimental effects on the morphological and textural properties of the solids. Moreover, under strongly acidic conditions, metal precursors exist mainly in the cationic form (M^{n+}) rather than their corresponding oxo species (M–OH), and therefore the insertion of heteroatoms via a condensation process with silicon species is not favored[151, 152]. The elimination of the thermal treatment may enhance the stability of metal oxo species resulting in a better interaction between the M–OH and Si–OH species in the synthesis gel to form metal–O–Si bonds[151, 152]. In order to investigate these possibilities and to reduce both reaction time and energy consumption, an analogous sample was synthesized eliminating the additional HT step at 100 °C for 24 h (Sn-NTs-B). Both solids were characterized employing several techniques including transmission electron microscopy, N_2 physisorption, FT-IR spectroscopy and solid state nuclear magnetic resonance among others. Transmission electron microscopy (TEM) investigation, performed on Sn-NTs-A and -B solids, revealed mainly the presence of nanotubes and a minor amount of nanospheres (Figure 1.1a and c). The nanostructures exhibit an average diameter of about 20 nm with an inner porosity of c.a. 15 nm. After calcination, the appearance of nanostructures of reduced length was observed indicating that the thermal treatment resulted in a partial cleavage of some tubes into smaller fragments (Figure 1.1b and d).

It is important to underline that, in view of the future catalytic applications, the presence of short tubes may represent an advantage, since an even increased accessibility of reactant and products to/from the active sites could

be achieved in presence of nanotubes with decreased length. The textural properties of both solids after calcination were characterized through N_2 physisorption measurements (Figure 1.2 and Table 1.1). Both materials exhibited high specific surface area (Table 1.1). The observed hysteresis loop can be considered as a combination of two different contributions due to the presence of tubular structures as well as to disordered cavities generates by the entangled nanotubes. This behavior is particularly evident in the case of Sn-NTs-A which displays a step-wise desorption branch at intermediate relative pressure typical of tubular structures open at both ends together with a sloping adsorption branch characteristic of heterogeneously distributed pores. In the case of Sn-NTs-B, the broadness of the hysteresis loop may indicate that the nanotubes prepared without the hydrothermal treatment had also narrow entrances and/or constrictions. It has been hypothesize by Kruk et al.[150] that the hydrothermal treatment causes an enlargement of the entrances to the mesopores in this kind of nanostructures. Due to the entangled nature of nanotubes, the pore size distributions was estimated via the Barrett-Joyner-Halenda (BJH) method using the Kruk-Jaroniec-Sayari (KJS) correction[153, 154] (Figure 1.2).

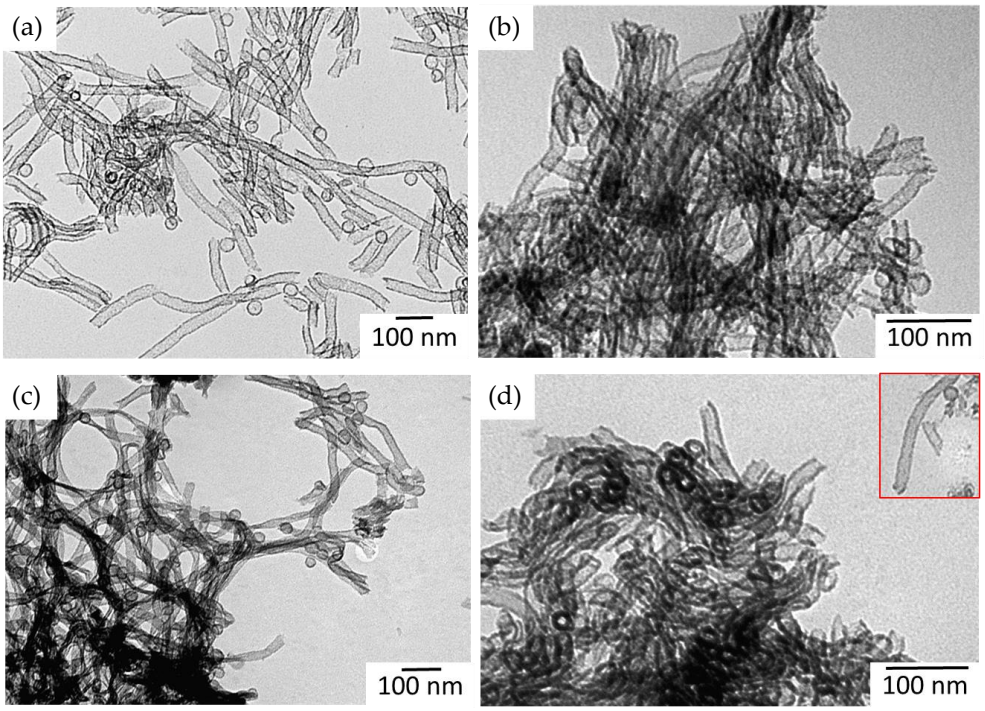

FIGURE 1.1: TEM micrographs of: Sn-NTs-A before (a) and after calcination at 550 °C (b) and Sn-NTs-B before (c) and after calcination at 550 °C (d).

Two distinct porosities can be clearly distinguished, the first and more defined contribution centered at around 14 nm could be attributed to the internal void of the 1D structure in agreement with TEM observations, while the second broader band was ascribed to the irregular inter-tubular spaces. Solid state ^{29}Si MAS-NMR analysis revealed the presence of a broad asymmetrical band centered at -105 ppm, which can be considered as an overlapping of three different contributions centered at -90, -100 and -110 ppm and corresponding respectively to $Si(OSi)_2OH_2$ (Q^2) $Si(OSi)_3OH$ (Q^3) and $Si(OSi)_4$ (Q^4) species. As expected, the degree of condensation, defined as $Q^4 / \sum Q^n$, was lower than standard silica based particle with spherical structure[12] (Figure 1.3A). This result may be considered as a consequence of the 1D morphology of the nanotubes which display a surface decorated with hydroxyl groups. The tin loading was quantified via inductively coupled plasma optical emission spectroscopy (ICP-OES), the Si/Sn ratios are reported in Table 1.1. For comparison all-silica nanotubes (Si-NTs) were synthesized as well and fully characterized (Table 1.1 and Figure 1.3B).

It is known that the isomorphic substitution of silicon with a metal center in tetrahedral coordination within the SiO_2 network does not represent an easy achievement. Various parameters may influence the metal insertion including temperature, pH, nature and modality of addition of the inorganic precursors among others. The lower amount of tin inserted as single site in the silica nanotubes compared to other porous silica structures previously reported in the literature could be ascribed to the high acidity of the synthesis medium[155] (see page 46). Shah et al. observed a similar behavior for the synthesis of Sn-SBA-15 solids[156]. Increasing amount of Sn in the synthesis mixture did not

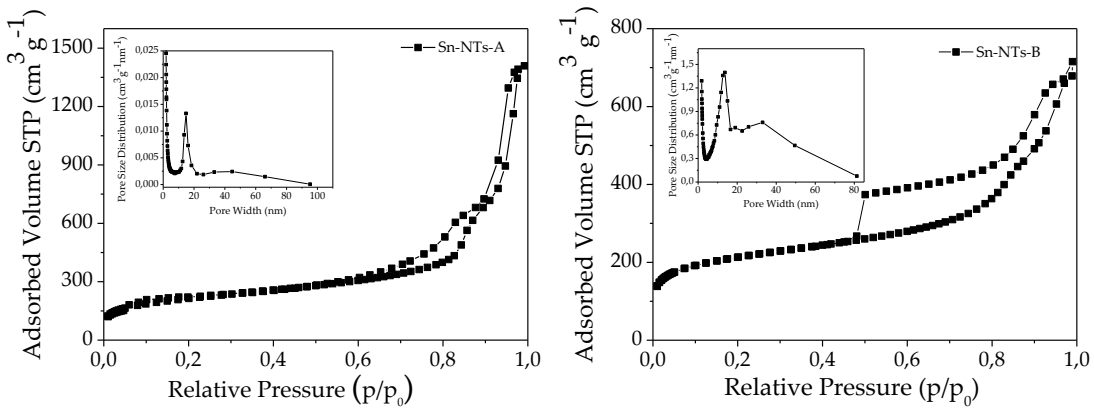

FIGURE 1.2: Nitrogen adsorption/desorption isotherms of Sn-NTs-A and Sn-NTs-B.

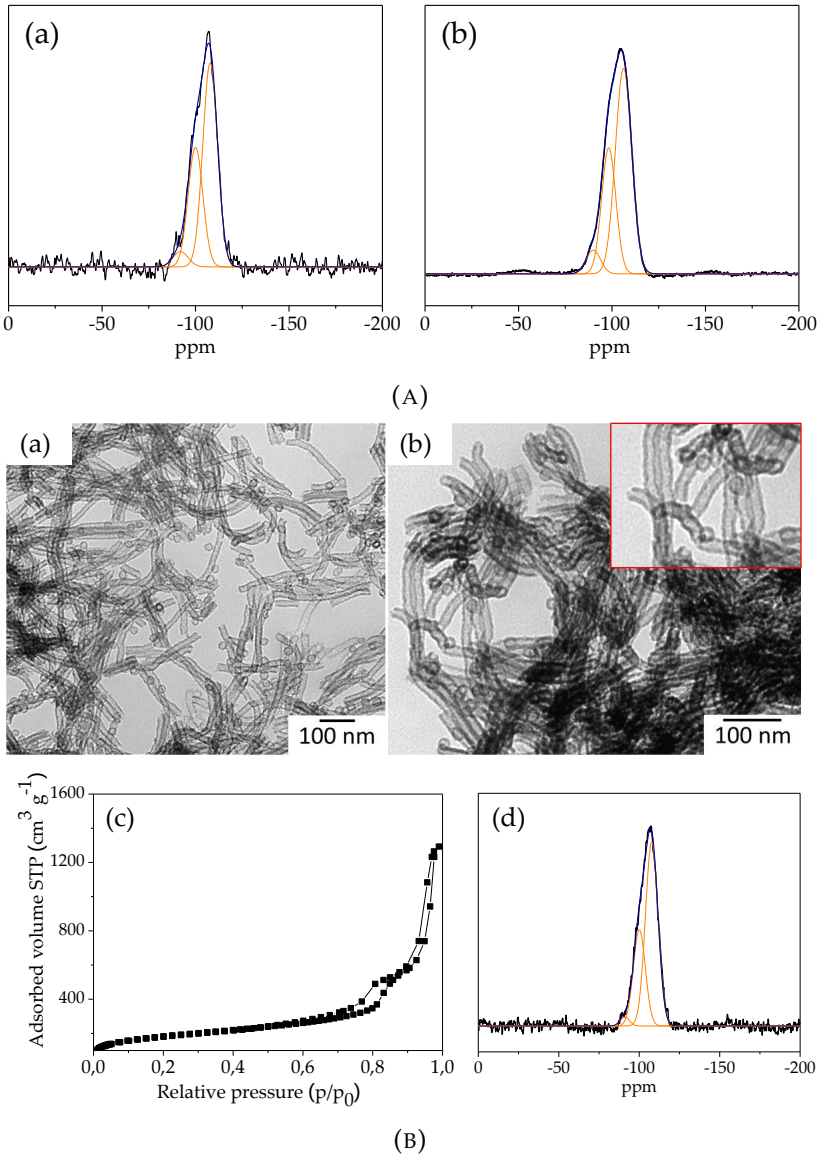

FIGURE 1.3: (A) ^{29}Si solid state DE-MAS NMR (99 MHz) spectra of Sn-NTs-A (a) and Sn-NTs-B (b). (B) TEM micrographs of Si-NTs not calcined (a); Si-NTs after calcination at 550 °C under air (b), N_2 ads/des isotherm of Si-NTs (c), ^{29}Si solid state DE-MAS NMR (99 MHz) spectrum of Si-NTs (d).

allow higher insertion of metal in the tubular structure. However, for the selected application, the amount of Sn determined experimentally is more than enough to ensure a good catalytic activity. More importantly, the insertion of Sn in tetrahedral coordination should be carefully addressed. In order to deal with this objective solid state ^{119}Sn NMR experiments were performed as well (Figure 1.4).

It is known[157, 158] that the isomorphic substitution of Si with Sn in a silica framework is characterized by the appearance in ^{119}Sn NMR spectra of a

band centered at around -700 ppm which can be attributed to tetrahedral coordinated tin atoms connected to four silicon through oxygen bridges or to partially hydrated intra-framework Sn species. Whereas, extra-framework SnO_2 nanoparticles would give a signal presenting a maximum at around -600 ppm. In the case of Sn-NTs-A a broad band shifted at higher frequencies is observed indicating the presence of a combination of intra- and extra-framework tin species (Figure 1.4b). On the other hand, Sn-NTs-B mainly displays tin inserted as single site (Figure 1.4c) even if, due to the broad linewidth, the presence of a minor contribution of extra-framework SnO_2 cannot be completely excluded. This result suggests that the additional hydrothermal treatment leads to the formation of tin oxides domains with a detrimental effect on the insertion of tin as single site. This behavior could be ascribed to the strong acid conditions

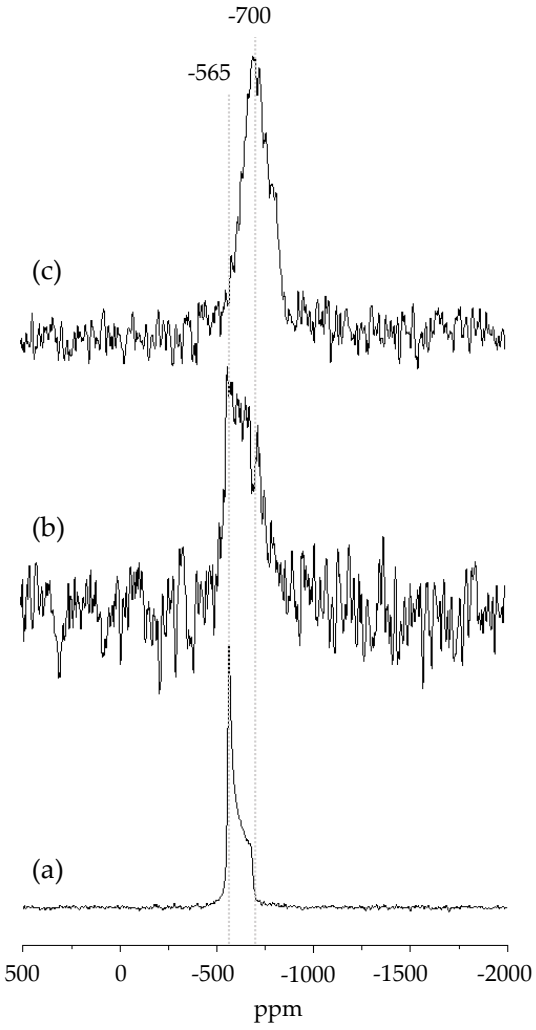

FIGURE 1.4: Solid state ^{119}Sn static NMR spectra recorded in static conditions of SnO_2 (a), materials Sn-NTs-A (b) and Sn-NTs-B (c).

of the synthesis solution which, in combination with the relatively high temperature (100 °C) of the hydrothermal treatment, could cause a migration of the intra-framework tin species to external surface through a process similar to the extensively described dealumination[159]. It is known[160] that zeolites can be dealuminated using high temperature steam or at more moderated temperatures (30 to 100 °C) in presence of elevated concentrations of mineral acids. On the other side, the insertion of Sn in SBA-15 matrix was successfully achieved using milder reaction conditions in terms of acidity (e.g. the HCl auto-generated from the hydrolysis of the $SnCl_4$ precursor)[161]. However, similar conditions cannot be applied in the present synthesis since the formation of tubular structure requires very low pH. Hence, Sn-nanotubes obtained without the additional hydrothermal treatment (sample B) constitute the best compromise between the acid conditions needed to obtain the 1D structures and the insertion of Sn as single site. Moreover, this procedure allows obtaining a potentially better solid in a shorter synthesis time. The main reason behind the isomorphic substitution of silicon with tin is the generation of the appropriate balance of Lewis/ Brønsted acidity to promote both the conversion of dihydroxyacetone into ethyl lactate and of glycerol into solketal. From the analysis of ^{119}Sn NMR data, it would be reasonable to suppose that Sn-NTs-B should display a higher amount of acid sites, hence better catalytic performances, compared to Sn-NTs-A. In order to investigate the acidic properties, in term of acid site nature and concentration, the samples were studied via FT-IR of adsorbed ammonia (basic molecular probe), which can interact both with Brønsted (surface hydroxyls) and Lewis (surface Sn(IV)) sites. FT-IR difference spectra (1700-1300 cm^{-1} range) of ammonia adsorption on both Sn-NTs-A and Sn-NTs–B are shown in Figure 1.5 (see a and b). The absorption band at 1635 cm^{-1}corresponds to the bending mode of NH_3 molecules H-bonded to hydroxyl groups, whereas the broad signal at around 1460 cm^{-1} is due to the bending mode of NH_4^+ ions resulting from proton-transfer reaction from Brønsted acidic groups. This suggests that the incorporation of Sn within the nanotube framework is able to provide Brønsted sites acid enough to protonate NH_3. On the contrary, the surface hydroxyls of pure silica materials interact with NH_3 via hydrogen-bonding without proton transfer. The intensity of the band ascribed to ammonium ion is significantly higher and broader for Sn-NTs-B compared to Sn-NTs-A, suggesting that the surface of the sample prepared without hydrothermal treatment is characterized by a larger population of hydroxyl groups.

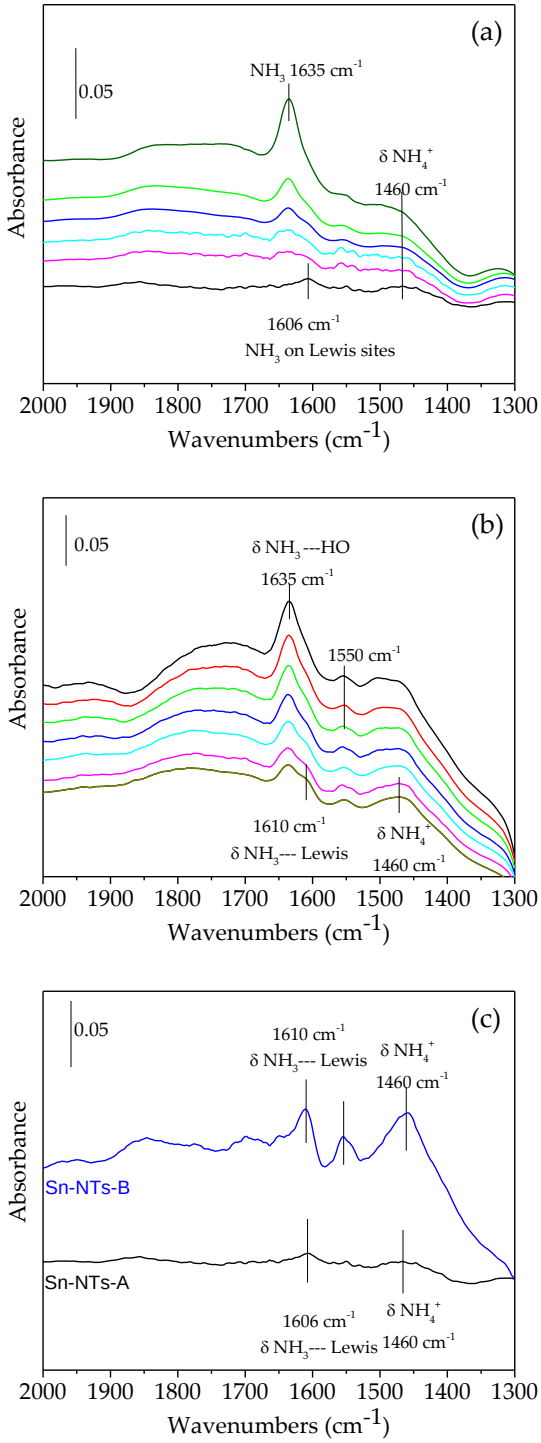

FIGURE 1.5: Difference FT-IR spectra of NH_3 dosages on Sn-NTs-A (a) and Sn-NTs-B (b) and after prolonged outgassing (c)

The larger broadness and the blue-shift of the ammonium band for Sn-NTs-B is attributed to the multiple lateral interactions of ammonium species with neighboring OH groups, which are more abundant for this system. Moreover,

the spectra related to Sn-NTs-B reveal an additional component at around 1550 cm^{-1} which, based on the literature[162], can be assigned to N-H bending vibration of Si-NH_2 species formed through reaction of strained siloxane bridges with ammonia. This reactivity is usually observed on amorphous silica-based materials upon treatment at high outgassing temperatures (700-800 °C). Here, although the lower outgassing temperature (400 °C) a similar assignment for the band is proposed. The peculiar nanotubular morphology of the investigated samples could cause the presence of strained reactive siloxane bridged as a consequence of the curvature of the surface. For both samples, a shoulder at around 1610 cm^{-1} ascribed to ammonia molecule adsorbed on surface unsaturated cations acting as Lewis sites was observed. Figure 1.5c reports a comparison between the difference spectra of Sn-NTs-A and Sn-NTs-B after a prolonged outgassing at room temperature. For both samples the characteristic signal of NH_4^+ ions became less intense upon outgassing (reversible proton transfer), the absorption band attributed to NH_3 physisorbed on silanols (1635 cm^{-1}) decreased in intensity and was red-shifted up to 1606 cm^{-1} for Sn-NTs-A and 1610 cm^{-1} for Sn-NTs-B for the fully outgassed samples (residual pressure $<1 \cdot 10^{-3}$ Pa). The band at 1550 cm^{-1} ascribed to Si-NH_2 is still clearly discernible in the spectrum of Sn-NTs-B, in agreement with the proposed assignation. It is evident that upon the same outgassing time the residual bands for Sn-NTs-B are significantly more intense than those of Sn-NTs-A, evidencing the larger population of Brønsted and Lewis acidic sites for the sample that did not undergo hydrothermal treatment. Furthermore, the residual bands assigned to ammonia on Lewis sites is at higher frequency for sample Sn-NTs-B (blue curve) compared to that recorded on Sn-NTs-A (black curve), which indicates for the former the presence of Lewis sites with average higher acidic strength compared to the latter[163].

On the basis of the characterization results discussed above, it can be evidenced that tin-silica nanotubes present favorable features in the perspective of catalytic applications. The combination of acid sites, high specific surface area and the accessible pores are expected to have a positive impact on performances of the materials. The catalytic performances of the Sn-NTs were initially investigated selecting the conversion of dihydroxyacetone (DHA) into ethyl lactate (EL) as target reaction. To allow a meaningful comparison between the two solids, as well as with reference catalysts reported in the literature, the activity was compared in term of turnover frequency (TOF, defined as moles of DHA converted/ moles of Sn x time(h)). The reaction time was

selected in order to be far enough from the full DHA conversion. Two blank tests were initially carried out (Table 1.2) evidencing that in absence of catalyst no conversion is achieved (Table 1.2, entry 1) and, more importantly, that silica tubes are not acid enough to promote the conversion of DHA into EL (Table 1.2, entry 2). The catalytic tests performed with Sn-silica nanotubes evidenced that these materials are active catalysts for the selected reaction (Table 1.2, entries 3-4). As expected, Sn-NTs-B displayed enhanced catalytic performances than the analogous Sn-NTs-A. Since both morphology and textural properties

TABLE 1.2: Conversion of DHA into ethyl lactate catalyzed by Sn-NTs materials

Entry	Catalyst	Si/M	Conv.$_{DHA}$ (%)	Sel.$_{EL}$ (%)	TOF (%)	Ref.
1	**No catalyst**	-	-	-	-	This work
2	**Si-NTs**	-	-	-	-	This work
3	**Sn-NTs-A**	133	34	38	17	This work
4	**Sn-NTs-B**	135	56	63	30	This work
5	**Sn-MCM-41**	49	32	94	7	[69]
6	**XS-Sn-MCM-41**	63	64	69	17	[135]
7	**Sn-TUD-1**	51	30	90	6	[164]
8	**XS-Ga-MCM-41-H**	15	20	60	2	[11]
9	**Zr-TUD-1**	51	31	91	7	[164]

Reaction condition: 50 mg of catalyst, 5 mL of 0.4 M DHA solution in absolute EtOH, 6 h at 90 °C. Number of Sn mol calculated from ICP-OES analysis on the calcined materials. TOF =$(n_{DHAconv.}/n_{Sn})h^{-1}$

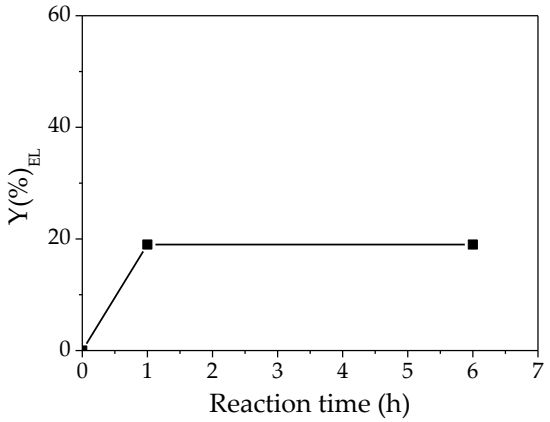

FIGURE 1.6: Hot filtration test for material Sn-NTs-B: yield of EL after 1 h and 6 h (catalyst removed). Reaction conditions: 2.5 mL 0.4 M DHA in EtOH, 50 mg of catalyst, 6 h at 90 °C.

of the materials are similar, these results could be ascribed to the better insertion of tin within silica framework in the case of Sn-NTs-B and to the consequent higher acidity of this material. It is important to underline that the best solid displays excellent TOF, higher than other Sn-based silica materials previously reported in literature (compare entries 3, 4 with 5-7). Moreover, Sn-NTs-B presents outstanding performances compared to other catalysts bearing Ga and Zr inserted as single site (compare entries 4 with 8, 9). A preparative test with Sn-NTs-B material was performed as well. Under optimized reaction conditions, (see experimental part) a high conversion (c.a. 90%) and a total selectivity (> 99%) were successfully achieved. The absence of leaching of catalytic active species was proved through a hot filtration experiment (Figure 1.6). After 1h reaction the catalyst was removed via hot filtration and the filtrate was left to react under the same conditions for additional 5 h. As can be seen from the figure the EL yield remains constant over time, proving that the reaction was performed in the presence of a true heterogeneous catalyst.

The second target reaction is represented by the acetalization of glycerol with acetone to produce solketal. Only the most active Sn-NTs-B was tested as catalyst for this reaction. In principle, the acetalization reaction can yield both five and six-membered ring compounds: (2,2-dimethyl-1,3-dioxolan-4-yl) methanol simply called solketal and (2,2-dimethyl-1,3-dioxan-5-ol) called

TABLE 1.3: Condensation of glycerol with acetone yielding solketal by Sn-NTs materials and comparison with literature data

Entry	Catalyst	Solvent	Yield$_{SK}$ (%)	Sel.$_{SK}$ (%)	TOF	Ref.
1	**No catalyst**	-	7	99	-	This work
2	**Si-NTs**	-	8	99	-	This work
3	**Sn-NTs-B**	-	58	97	378	This work
4	**Sn-NTs-B**	t-butanol	26	96	185	This work
5	**Sn-MCM-41**	t-butanol	42	99	102	[8]
6	**Sn-TUD-1**	t-butanol	44	99	94	[164]
7	**XS-Ga-MCM-41-L**	t-butanol	25	99	60	[11]
8	**Zr-TUD-1**	t-butanol	46	99	127	[8]
9	**Al-TUD-1**	t-butanol	28	99	61	[8]

Reaction conditions: 0.920 g of glycerol (0.01 mol), 4 eq. of acetone, 25mg of catalyst at 6 h, 80 °C. Entries 4-9: 0.920 g of glycerol (0.01 mol), 1 eq. of acetone, 1.48g of t-butanol, 25mg of catalyst at 6 h, 80 °C. TOF =$(n_{solketal}/n_{Sn})h^{-1}$.

TABLE 1.4: Condensation of glycerol with acetone yielding solketal by Sn-NTs materials

Entry	**Amount** (mg)	**T** (°C)	**Time** (h)	**Yield**$_{SK}$ (%)	**Sel.**$_{SK}$ (%)	**Prod.**	**TON**	**TOF**
1	10	80	6	42	95	39	3892	649
2	25	80	6	58	97	21	2267	378
3	10	50	6	20	84	18	1565	261
4	25	50	6	42	93	15	1377	230
5	50	50	6	61	98	11	1000	167
6	100	50	6	63	99	6	516	86
7	25	50	0.5	11	81	4	344	688
8	25	50	1	17	85	6	532	532
9	25	50	2	24	85	9	751	376

Reaction conditions: 0.920 g of glycerol (0.01 mol), 4 eq. of acetone, catalyst. TON =$(n_{solketal}/n_{Sn})$ TOF =$(n_{solketal}/n_{Sn})h^{-1}$.

acetal. Recently, one of the best solketal yield reported in the literature was achieved employing an acetone to glycerol ratio equal to 4:1 [165]. Hence, this ratio was selected to screen the catalytic performance of Sn-NTs-B. The tests were carried out under solvent free conditions varying the temperature, reaction time and amount of catalyst. Blank experiments performed at 80 °C for 6 h in the absence of catalyst (Table 1.3, entry 1) or with silica nanotubes (table 1.3, entry 2), resulted in both cases in a very low glycerol conversion (c.a. 7%). Under the same reactions conditions, Sn-NTs-B catalyst displayed excellent catalytic performance, demonstrated not only by the high conversion and selectivity toward solketal, but also by the very high turnover frequency, equal to 378 (Table 1.3, entry 3).

The high TOF represents a clear indication of the high activity of the tubular structures, however the absolute values of turnover frequency are meaningless without comparison with literature data. Since several articles report the use of solvents, in order to allow a meaningful comparison with reference solids an additional catalytic test employing t-butanol as solvent was performed. The results resumed in table 1.3 evidence the higher catalytic performance of Sn-NTs-B respect to Sn-based solids (entries 5, 6) and other metal-containing silicates reported in literature (entries 7-9)[8, 164]. This result further evidences the excellent performances of Sn-silica nanotubes. In view of sustainable processes, the decrease of reaction temperature represents a key aspect. To this purpose, two additional tests at 50 and 25 °C (Figure 1.7) were implemented.

It is important to underline that the overall catalytic performances (conversion and selectivity) did not suffer of a relevant decrease when the test was performed at 50 °C. Surprisingly, when glycerol acetalization was performed at 25 °C, a moderate solketal yield (20%) was still observed despite the challenging conditions. The decrease of activity may be also ascribed to the intrinsic difficulties of the selected reaction conditions due to the high viscosity of glycerol which (at 25 °C) can be also responsible for diffusion limitations. The effect of the amount of catalyst was investigated as well and the most representative tests are reported in Table 1.4. At 80 °C a surprisingly high TON equal to 3892 (entry 1) was obtained lowering the amount of catalyst to only 10 mg. However, raising the catalyst mass loading at 25 mg did not result in a proportional improvement in the conversion. A similar behavior was observed when performing the reaction at 50 °C. A plateau is reached around 60% yield of solketal. Comparable results were observed by Nanda et al.[3, 138]. In this context, the authors reported a study based on the influence of the catalyst amount (Amberlyst-35) on glycerol ketalization reaction.

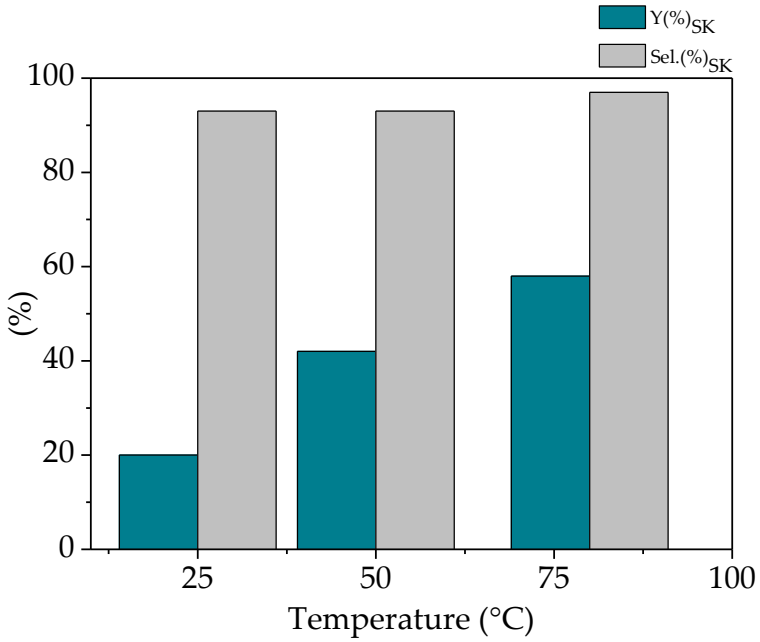

FIGURE 1.7: Acetalization of glycerol performed at different reaction temperatures using Sn-NTs-B. Reaction conditions: 0.920 g of glycerol (0.01 mol), 4 eq. of acetone, 25 mg of Sn-NTs-B for 6 h.

To support this analysis a kinetic investigation was also performed by monitoring the formation of solketal over time in the range of 30 min to 24 h (Figure 1.8). All tests were carried out at 50 °C, using 25 mg of Sn-NTs-B as catalyst (Figure 1.8). The analysis of these data allows evidencing that at about

60% solketal yield an equilibrium is reached and further improvements of the catalysts performances are not possible in absence of modifications of some parameters (e.g. reactants addition or product removal) which can alter the equilibrium itself. In line with these considerations, not all the TOF reported in table 1.4 are truly representative of the catalyst performances and most of them (e.g. entries 2, 5 and 6) underestimate its activity. Hence, a more representative TOF value was recalculated at the very early stage of the reaction (table 1.4, entries 7 to 9). All the previously reported results suggest that a reaction temperature of 50 °C can be selected as best compromise between catalytic activity and sustainability (reduced energy consumption). Hence, the last screenings were performed at this temperature. The heterogeneous nature of catalyst Sn-NTs-B was proved by hot filtration experiment (Figure 1.9, left). As can be clearly observed in the figure, the yield of solketal did not increase after removal of the catalyst from the reaction mixture, indicating the absence of leaching of active sites. The reusability of Sn-NTs-B was investigated at intermediate solketal yield far enough from glycerol equilibrium conversion (Figure 1.9, right). After each run, the catalyst was reactivated by a short calcination treatment before the following catalytic cycle (see experimental part).

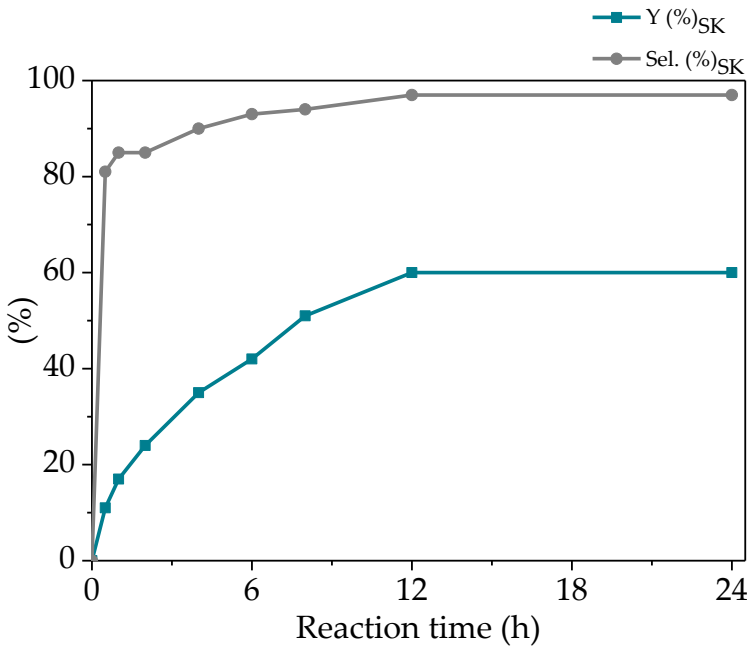

FIGURE 1.8: Kinetic study with Sn-NTs-B. Reaction conditions: glycerol (0.01 mol), 4 eq. of acetone at 50 °C

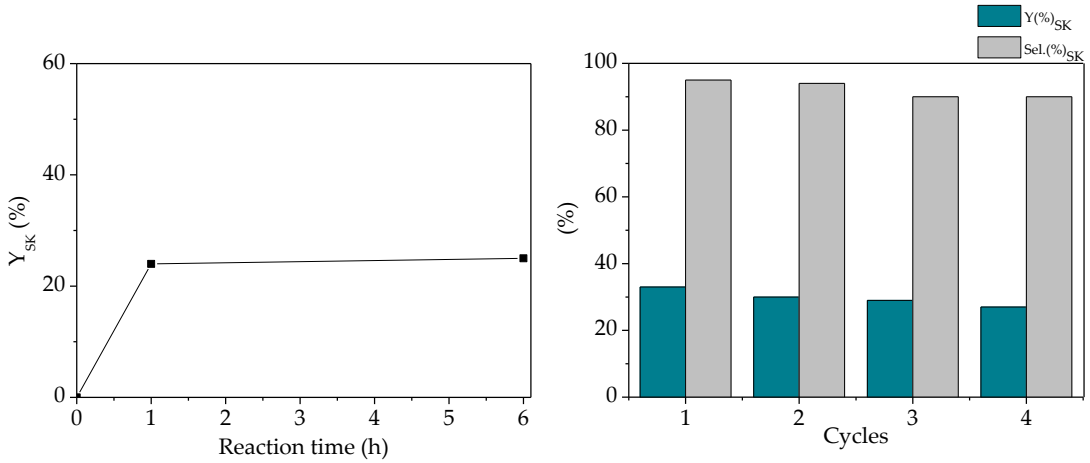

FIGURE 1.9: Hot filtration experiment (left) and recycling tests (right) with Sn-NTs-B material. Reaction conditions: 0.920 g of GLY (0.01 mol), 25 mg of catalyst, 4 eq. of acetone (hot filtration); 1.840 g of GLY (0.02 mol), 60 mg of catalyst, 4 eq. of acetone, 50 °C for 4 h (recycling tests).

Only a minor decrease in term of yield and selectivity was observed upon successive reuses, suggesting that tin-silica tubes were stable in the reaction conditions. The calcination treatment is of fundamental importance since it was already reported[11] that the activity gradually decreases upon reuse if the catalyst is only washed with the reaction solvent. This behavior was ascribed to the adsorption of organic species on the surface of the catalyst, which cannot be efficiently removed by washing procedures. The absence of tin leaching was again supported by ICP-OES analysis on the regenerated catalyst. After the fourth cycle, no difference was observed in term of Si/Sn ratio between the fresh and reused catalyst (Table 1.5). Moreover, the full characterization of the catalyst after recycle via TEM, N_2 physisorption and ^{119}Sn NMR did not display substantial differences with the fresh solid hence supporting further the stability of the Sn-NTs-B material under the selected reactions conditions (see Figure 1.10 and 1.11).

TABLE 1.5: Properties of Sn-NTs-B material before and after recycling tests

Entry	Material	S_{BET} ($m^2\,g^{-1}$)	PD (nm)	Si/Sn
1	**Si-NTs-B**	754	13	135
2	**Sn-NTs-B after 4th cycle**	670	13	135

Specific surface area calculated from adsorption data in relative pressure range of 0.05-0.20 p/p_0 for all materials; Pore diameter determined by BJH-KJS model.

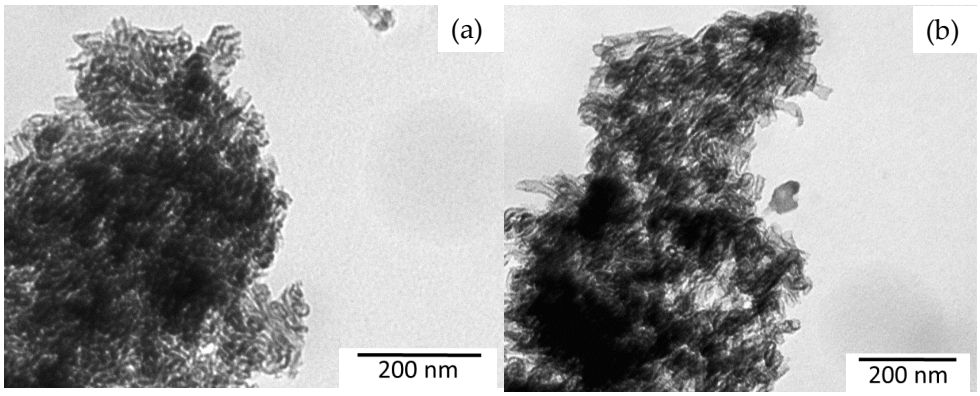

FIGURE 1.10: TEM micrographs of Sn-NTs-B (a and b) after the 4th cycle of the reaction of glycerol with acetone yielding solketal.

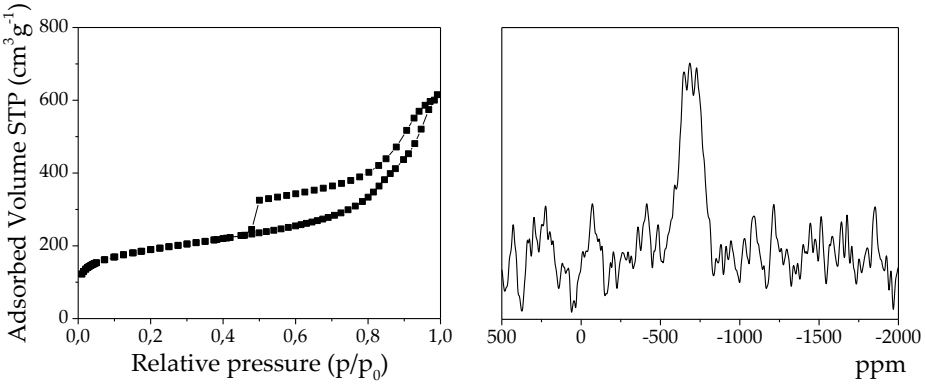

FIGURE 1.11: N_2 ads/des isotherm (left) and ^{119}Sn solid state static NMR spectrum of Sn-NTs-B (right) after the 4th cycle of the reaction of glycerol with acetone yielding solketal.

1.3 Conclusions

A novel silica based solid displaying a 1D tubular structure and bearing Sn inserted as single site in the framework was successfully prepared for the first

time. The synthesis procedure was optimized in order to achieve the isomorphic substitution of silicon through a relatively short protocol. The solid was fully characterized via transmission electron microscopy, ICP-OES analysis, ^{29}Si and ^{119}Sn solid state NMR spectroscopy. Specific surface area and the pore dimensions were determined through N_2 physisorption measurements. Due to the entangled organization of the Sn-nanotubes the standard Barrett-Joyner-Halenda (BJH) pore size distributions was implemented using the Kruk-Jaroniec-Sayari (KJS) correction. The optimized material exhibited outstanding catalytic activity in particular in the direct conversion of glycerol to solketal. This behavior was ascribed to the good insertion of tin within silica framework as well as to the high acidity of the Sn-NTs as proved by FT-IR measurements of ammonia adsorption. The exceptional catalytic performance of the solid allow decreasing the reaction temperature with good results in terms of solketal yield. Moreover, the catalyst proved to be stable under the selected conditions and reusable in multiple runs. The robustness of the Sn-silica nanotubes was also supported via full characterization of the solid after the 4th cycle.

Part II

Introducing the aerosol assisted sol-gel process

In this second part of the manuscript a rather innovative synthetic process, coupling the principles of sol-gel chemistry with aerosol processing, will be presented and meticulously exploited for the synthesis of Sn and Ga substituted structured porous silicates. In the following four chapters we will present the advantages of this very versatile technique for the preparation of porous catalysts and eventually some limitations. It deserves to be mentioned that a wide range of techniques based on the processing of aerosols has been developed for the preparation of different families of materials. Some of the most commonly encountered include spray drying, atomization, aerosol-assisted sol–gel, gas atomization, flame aerosol methods, aerosol-assisted self-assembly process, etc. All of these techniques have in common the atomization of a liquid sample in the form of a fog consisting of small droplets of micronic size[43]. In addition, numerous types of atomization techniques exist, using either pressure, centrifugal, electrostatic or ultrasonic energy to generate the desired feed of dispersed droplets. The main differences among the processes lie in the nature and properties of the sprayed solution or colloidal suspension and in the subsequently applied treatments on the aerosol. A classification of the different aerosol processes has been recently proposed in a review by Debecker et al.[43], identifying four main types (see Figure 1.1): (Type I) Simple drying of pre-existing particles in suspension leading to particles aggregates, (Type II) Molecules in solution are dried by aerosol and precipitate under the effect of solvent evaporation, (Type III) Molecular precursors in solution react via inorganic polycondensation reactions during the aerosol processing to yield a solid which is chemically different from the starting compounds. In the presence of sacrificial texturing agents, porous particles can be obtained and (Type IV) A metal melt, usually obtained from a mixture of different metals, is atomized and cooled to yield micronized metal particles. Our interest will be turned to the Type III class of processes. This class has been even splitted in three subcategories depending on the conditions used to trigger the chemical reactions during aerosol processing and in this manuscript in particular the Type IIIc will be our synthetic tool. In the Type IIIc class, called aerosol assisted sol-gel process, the precursor solution is atomised and the generated aerosol is dried in relatively mild conditions. The drying step triggers inorganic polycondensation reactions under the effect of increasing concentration or, for instance, of

a variation of the pH. In the starting mixture of precursors, we often find templating agents which can be either pre-formed or can self-assemble during the drying process (i.e. surfactants forming micelles). The obtained solids are usually thermally or chemically treated after the process to remove the templating agent and release the porosity or to modify the obtained solid (e.g. reduction to metal nanoparticles, transition from amorphous to crystalline structure, etc.). Often the starting mixture is composed of only molecular species without solid particles, which co-condense and self-assemble in a bottom-up process during the drying step. Compared to the standard solution routes, the aerosol-assisted sol–gel process involves a limited number of steps, may be set up to produce material in a continuous mode with a simple collection of powders and generates low amounts of wastes. Moreover, one interesting advantage if compared with standard precipitation methods is the kinetic quenching associated with droplet formation and fast drying that allows for the "freezing" of materials into metastable states. Looking at this vast panorama of possibilities to tune the properties of the materials, heterogeneous catalysis definitely became a very promising field of application of such preparation technique.

However, compared to the other class of aerosol processes, the controlled coupling between aerosol techniques and sol–gel chemistry is much more recent. The combination between sol–gel chemistry, evaporation-induced self-assembly and aerosol processing was considered as a convenient way to prepare porous materials, with some examples already reported in the literature

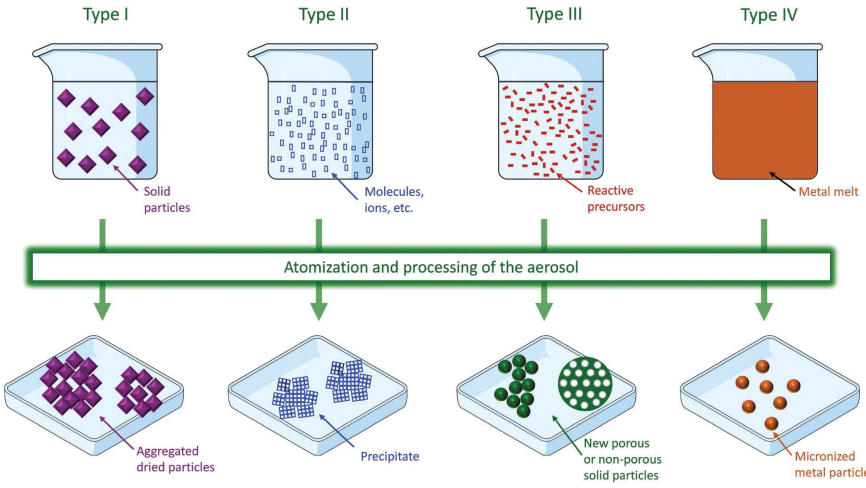

FIGURE 1.1: Classification in four categories of aerosol processes as reviewed by Debecker et al. for the preparation of solid particles[43]

around the 2000[146, 166, 167]. Bruinsma et al. in 1997 were the first to report the synthesis of mesoporous silica solids by spray drying of alkoxide-surfactant solutions[166]. They atomized an aqueous solution of hydrolyzed tetraethylorthosilicate (TEOS) containing also cetyltrimethylammonium chloride as templating agent. After drying of the aerosol and calcination they obtained solids consisting of hollow spherical particles of silica with a mesoporous texture. In 1999, Brinker et al. presented an aerosol-based process for synthesizing well-ordered and spherical silica particles with stable pore mesostructures[146, 168]. Furthermore, Datye et al. described the impact of preparation parameters like the temperature of the drying zone, the surfactant/TEOS ratio, the pH, etc. on the final properties of the obtained mesoporous silica[167]. In these examples, the method relies on the evaporation-induced self-assembly of surfactant molecules, and on the associated condensation of silica precursors in a similar fashion like other classical templated sol–gel syntheses. However, the whole process is confined to individual spherical droplets and occurs during the very short time (few seconds) needed to dry the particle. Considering the process applied to the synthesis of heterogeneous catalysts, the particle morphology is one key property which can participate in the enhanced catalytic performance. The size of the particles is mostly determined by the size of the aerosol droplets and by the composition of the starting solution and can be adapted tuning the proportion of volatile solvent/non-volatile species present in the initial mixture[169]. In addition, depending on the type of atomizer employed in the system, a range of droplets size can be selected[170]. Moreover, to control particle size and particle size distribution, the set-up operating parameters as precursor temperature, spray volume rate, drying gas volume rate can be precisely tuned. As particles formation is the consequence of drying of liquid droplets in their most stable spherical shape, aerosol processes characteristically produce spherical particles. Particle morphology can be adjusted as well and many different types of particle structures have been described in the literature[171]. These can be selectively obtained by a careful work on the drying conditions (type of drying gas, temperature, relative humidity, residence time, etc.). When looking specifically at heterogeneous catalysts, it is evident that the size and textural properties of the particles may have a tremendous importance on catalytic performance. Considering diffusion phenomena, governed by the size of pores and by the path that the reactants and products have to follow, small or hollow particles may be beneficial since they provide shorter diffusion distances[12]. Finally, this process

allows a precise control on the chemistry of the solid that largely governs the performance of a catalyst. Undeniably, an infinite number of combinations become possible when the template-directed sol–gel chemistry is coupled with aerosol processing. Examples of the use of aerosol assisted sol-gel processes for the preparation of heterogeneous catalysts have flourished in the past two decades. Type IIIc aerosol processes have offered marvelous new opportunities for the design of advanced heterogeneous catalysts in the last two decades, yielding a wide range of catalysts with tailored properties as texture, composition and surface functionalities.

Chapter 2

High-Yield Synthesis of Ethyl Lactate with Mesoporous SnSi Mixed Oxide Catalysts Prepared by the Aerosol-Assisted Sol-Gel Process

Abstract

An aerosol assisted sol-gel method is used to prepare mesoporous tin silicate catalysts which exhibit record activity in the synthesis of ethyl lactate from dihydroxyacetone and ethanol. The method is based on the formation of an aerosol from a solution of precursors and surfactant. During the fast drying of the droplets, the surfactant self-assembles and the Sn-silica matrix is formed by polycondensation reactions. After calcination, the resulting material is composed of a true Sn-Si mixed oxide in the form of spherical microparticles with calibrated mesopores of 5-6 nm. Tin species are incorporated in the silica network, mainly in the form of single-sites. This makes these catalysts highly active for the targeted reaction, as shown by record turnover numbers. The catalyst is shown to be recyclable and truly heterogeneous, as it can be reused for several cycles and as it does not leach.

The results presented in this chapter have been published in:

N. Godard[#], A. Vivian[#], L. Fusaro, L. Cannavicci, C. Aprile[*], D.P. Debecker[*], High-Yield Synthesis of Ethyl Lactate with Mesoporous Tin Silicate Catalysts Prepared by an Aerosol-Assisted Sol–Gel Process, ChemCatChem, 9 (2017) 2211-2218.

[#] These authors contributed equally to this work

2.1 Experimental section

In the aerosol-assisted sol-gel process (Figure 2.1), the condensation of the inorganic network occurs during a short drying time, along with the evaporation-induced self-assembly of surfactant molecules serving as sacrificial template to generate pores. The method allows the formation of spherical particles with calibrated porosity and with a precise control on the composition and homogeneity of complex formulations.

Preparation of the solids

Solution A was prepared by hydrolyzing 12 g of tetraethyl orthosilicate (TEOS) in an aqueous solution (20 g) at pH 2 (HCl, 0.01 M). Pluronic P123 (3.9 g) was dissolved in absolute ethanol (45 g) and acid aqueous solution (pH 2, 8 g) to yield solution B. Both solutions were left stirring overnight at room temperature and then tin (IV) chloride ($SnCl_4 \cdot 5H_2O$) was added to solution A in order to have a Si/Sn molar ratio equal to 74 or 37. Solutions A and B were mixed together and then stirred for 30 minutes. The clear solution obtained was atomized with a 6-Jet 9306A atomizer from TSI and the aerosol was dried by passing through a tubular quartz tube heated at 350 °C. The dried powders were collected on a cellulose nitrate filter, aged at 80 °C for one night and calcined under static air at 550 °C for 6 h (heating rate of 1 °C/min). Samples are denoted SnSi-x, where 'x' is the atomic Si/Sn ratio.

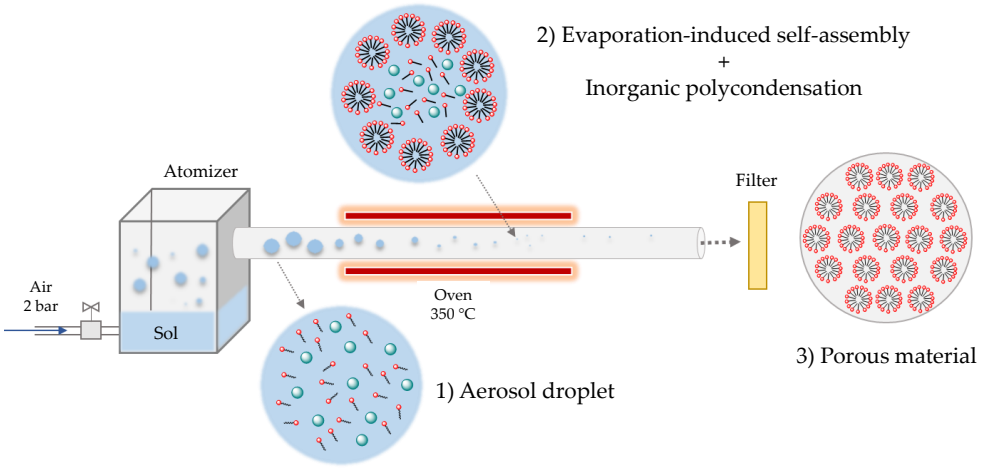

FIGURE 2.1: Schematic view of the aerosol-assisted sol-gel process.

2.2 Results and discussion

Two different tin silicates (SnSi-74 and SnSi-37) were synthesized via the aerosol-assisted sol-gel process. The main advantage of this one-pot synthesis procedure, compared to the traditional sol-gel approaches, is related to the possible formation of a solid catalyst in a continuous way without additional hydrothermal treatments under static conditions. This advantage together with the low waste production, the relatively short synthesis time and the easy collection of the solid allow considering the catalyst preparation as a sustainable procedure. The morphological and textural properties of the tin-silicates bearing respectively a silicon to tin ratio of 74 (SnSi-74) and 37 (SnSi-37) were first addressed via transition electron microscopy (TEM). The catalyst consists of particles with spherical morphology with size-calibrated mesopores of 5-6 nm visible down to the core of the spheres (Figures 2.2). The spherical shape of the solids is a reminiscence of the aerosol droplets from which the solvent evaporates during the drying step. The pores are a reminiscence of the P-123 surfactant micelles, removed by calcination after the drying step.

The particle size distribution was estimated through TEM measurements on 400 particles (Figures 2.3a and A.1b). Despite the presence of a minor

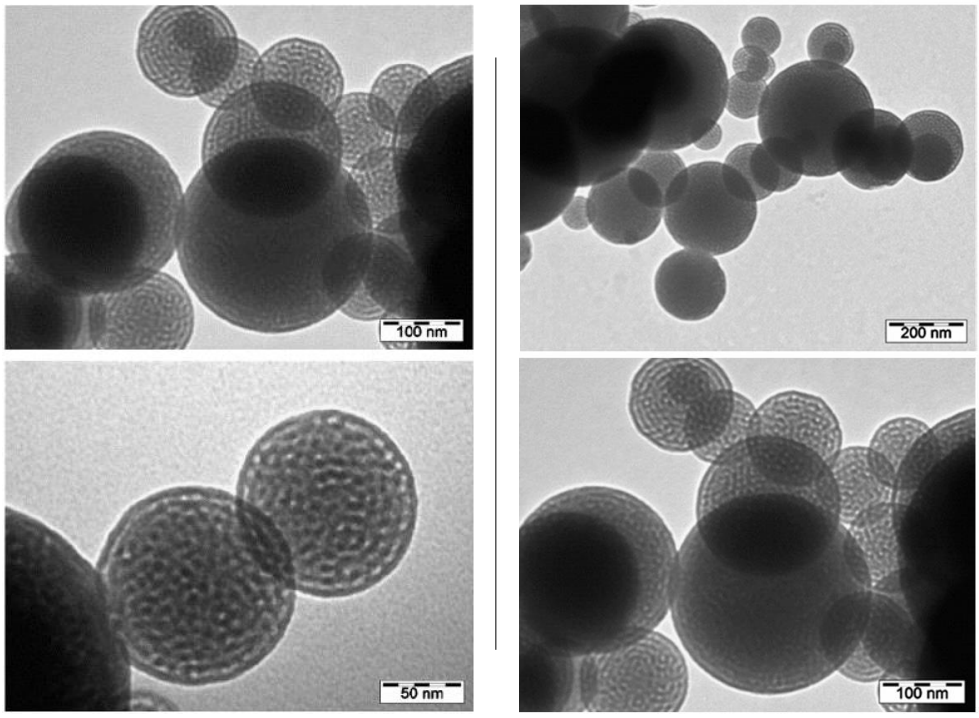

FIGURE 2.2: TEM micrographs of SnSi-74 (left) and SnSi-37 (right) materials.

TABLE 2.1: Physicochemical properties of the SiSn catalysts

Material	$\mathbf{a_0}$ (nm)	**PD** (nm)	**Wall** (nm)	$\mathbf{S_{BET}}$ ($m^2\,g^{-1}$)	**PV** ($cm^3\,g^{-1}$)	**Si/Sn**
SiSn-74	9.6	6.1	3.5	360	0.48	79
SiSn-37	9.0	6.3	2.7	370	0.52	41

Inter-reticular distance $a_0=2d_{100}\sqrt{3}$; PD: pore diameter; Wall thickness determined as the difference between a_0 and the pore diameter; S_{BET}: specific surface area; PV: pore volume; Si/Sn determined by ICP-OES analysis

amount of very large particles (diameter superior to 1000 nm), the majority of the porous spheres (90% of the measured particles) display a relatively narrow distribution and a small size with a particle diameter comprised between 140 nm and 380 nm. The textural properties of the tin silicates were confirmed by N_2 physisorption measurements (Figure 2.3b). Both solids displayed a type-IV isotherm characterized by a H2 hysteresis loop typical of tubular-shaped pores open at both ends. BJH analysis, performed on the adsorption branch of the isotherm, evidenced a narrow pore size distribution (PSD) centred at 6.1 nm in good agreement with TEM observations. This regular PSD corresponds to the thermal removal of P-123 micelles used as structure directing agent[172]. Both tin silicate materials exhibit a high specific surface area and pore volume (Table 2.1) as well as a minor contribution of microporosity corresponding to less than 10% of the total pore volume.

Small-angle XRD patterns (Figure 2.3c) revealed a sharp signal centred at 2theta = 1.1 deg corresponding to the d_{100} reflection together with two smaller contributions due to the d_{110} and d_{200} reflections, confirming the presence of porous structures characterized by large mesopores and long range order. The structural and textural properties of the two solids are summarized in Table 2.1. The chemical composition was verified by inductively coupled plasma optical emission spectroscopy (ICP-OES). The Si/Sn ratios for each material were in good agreement with the nominal composition (Table 2.1). However, in order to prove the insertion of Sn as single site within the silica framework additional characterization tools as diffuse reflectance UV-Vis and ^{119}Sn NMR spectroscopy are required. Diffuse reflectance UV-visible spectroscopy (Figure 2.3d) showed a main absorption band centred at 206 nm, which can be attributed to the presence of Sn(IV) in tetrahedral coordination within the silica

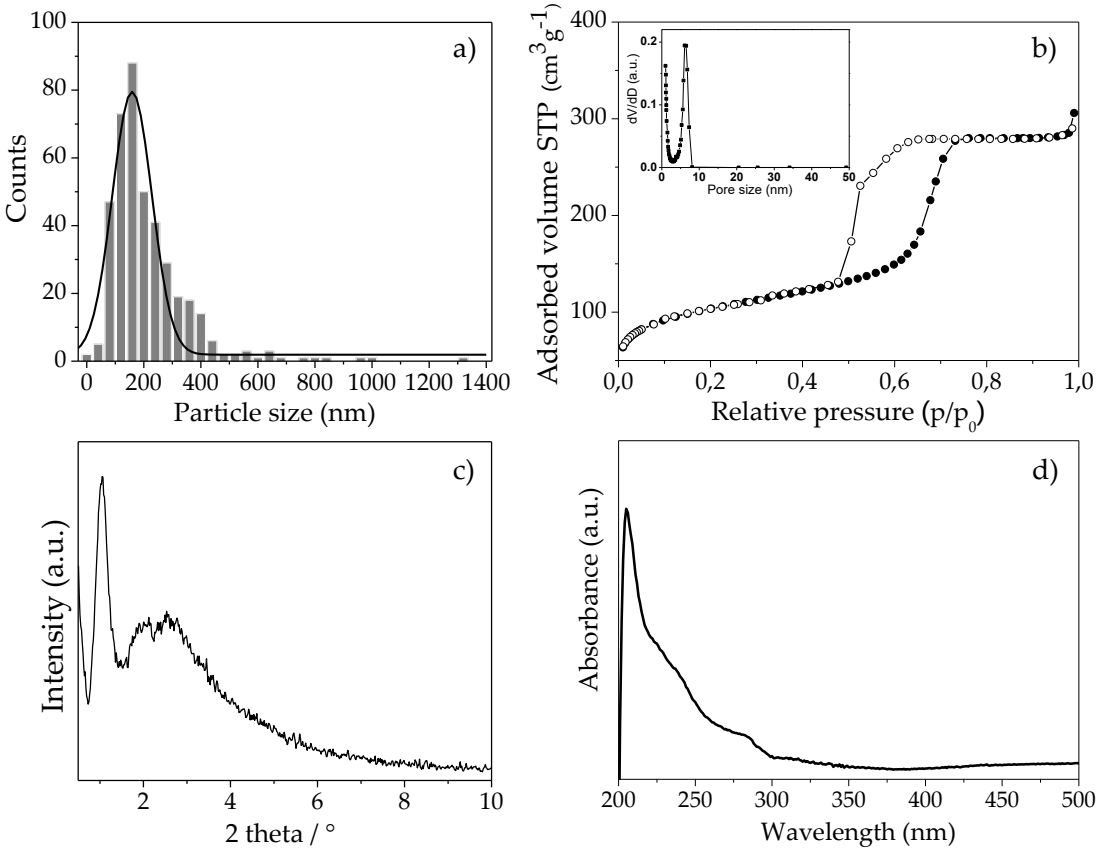

FIGURE 2.3: Particle size distribution (a), Nitrogen adsorption/desorption isotherms and corresponding pore size distribution (insert) (b), small-angle XRD pattern (c), diffuse reflectance UV–Vis spectrum of SnSi-74 catalyst.

architecture[157, 173]. The presence of small contributions at higher wavelengths (240 and 280 nm respectively) can be assigned to distorted tetrahedral or penta-coordinated intra-framework Sn species[173]. In the literature, these two bands are also assigned to extra-framework SnO_2 clusters (240 nm) and hexa-coordinated polymeric Sn–O–Sn type domains (285 nm)[174].

It is known that the synthesis of Sn silicates proceeds via hydrolysis of the precursors followed by condensation[175] with consequent formation of Sn-O-Si and Si-O-Si bonds. The degree of condensation can be addressed via ^{29}Si NMR. Figure 2.4a shows the ^{29}Si CP-MAS (cross-polarization magic-angle-spinning) spectrum of SnSi-74 material where the presence of Q^4 [$(SiO)_4Si$] (-111 ppm) and Q^3 [$(SiO)_3SiOH$] (-102 ppm) signals can be clearly observed. Due to the close proximity of Si atoms with hydroxyl groups in the Q^3 and Q^2 species, the intensities of Q^3 and Q^2 resonance lines are enhanced by the CP pulse sequence. Thus, the spectrum in Figure 2.4a was used to correctly assign the chemical shift of these two contributions, while for a quantitative

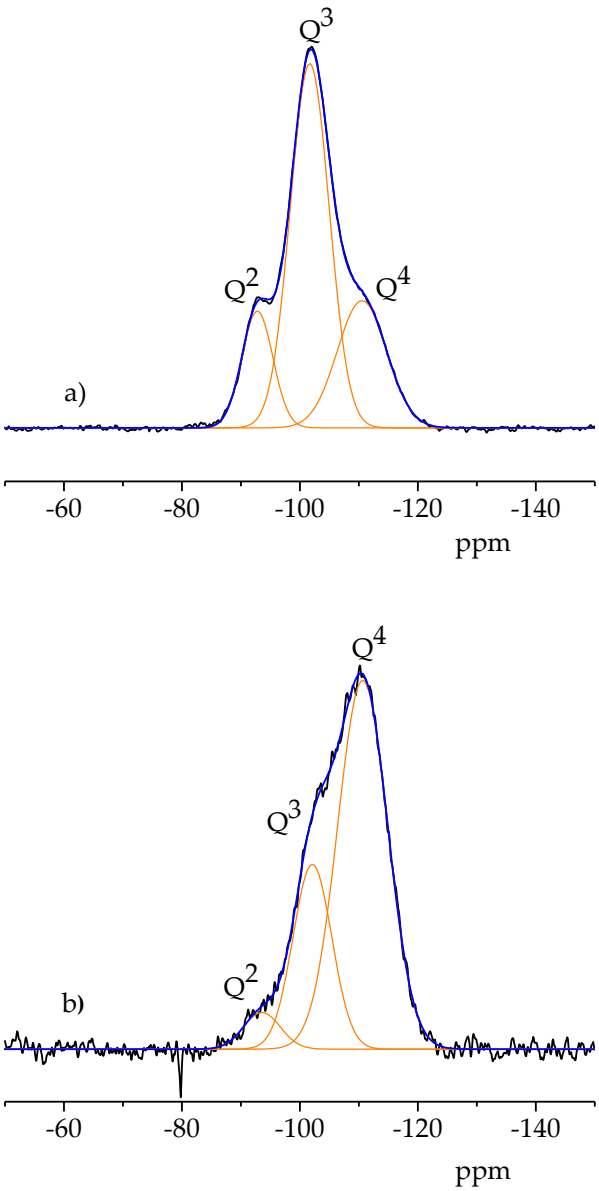

FIGURE 2.4: ^{29}Si solid state MAS NMR spectra of SnSi-74 a) Cross Polarization, b) Direct Excitation

evaluation a direct excitation experiment was performed as well.

Thus, Figure 2.4b displays the quantitative ^{29}Si MAS NMR spectrum obtained by direct excitation of ^{29}Si. The deconvolution analysis using Gaussian functions of the Q^n contributions allows estimating the degree of condensation of the material: $Q^4/(Q^4 + Q^3 + Q^2) = 2.2$. This value indicates a degree of condensation in good agreement with the ones reported for standard silica based solid[176]. ^{119}Sn-NMR performed under static conditions showed unambiguously that Sn was predominantly inserted in tetrahedral coordination.

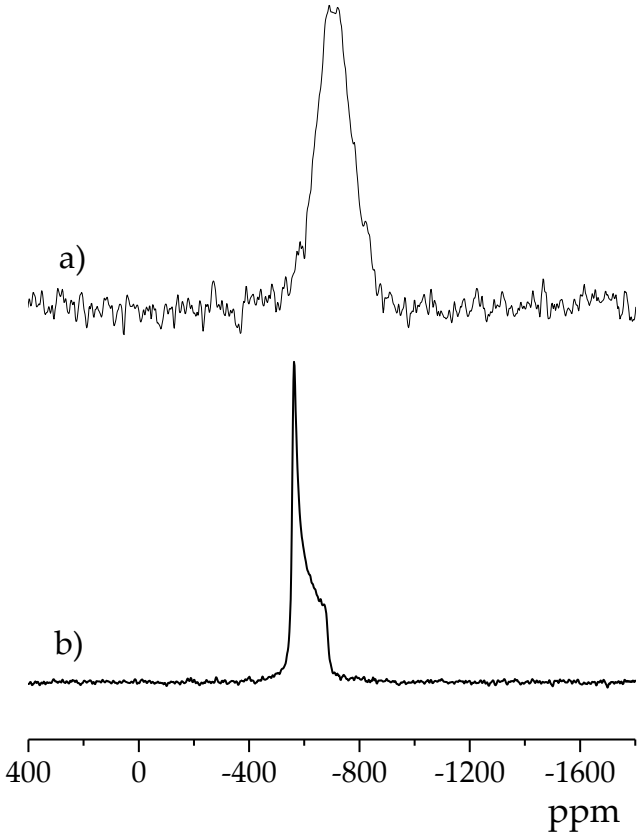

FIGURE 2.5: Solid state ^{119}Sn static NMR spectra of SnSi-74 catalyst a) and pure SnO_2 b)

The signal centred at around –695 ppm (Figure 2.5a) can be attributed to intra-framework Sn(IV) connected to four silicon atoms via oxygen bridges[157, 158] or partially hydrated tin species with an extended coordination shell. The presence of significant amount of SnO_2 was not detected, since such extra-framework Sn(IV) species in octahedral coordination would yield a signal similar to that of pure SnO_2 nanoparticles (Figure 2.5b) at around -600ppm [161, 177]. However, considering the broad linewidth of the signal in Figure 2.5a, the presence of minor amount of extra-framework SnO_2 cannot be completely excluded.

The catalyst displays a significant surface acidity, as probed by NH_3-TPD (Figure 2.6). After adsorption of NH_3 at 50 °C and flushing under inert, 220 $\mu mol\, g^{-1}$ of NH_3 desorb from SnSi-74 in two peaks centred at 120 °C and 200 °C, representative of weak and medium strength acid sites. The catalyst with a higher Sn loading (SnSi-37) displayed very similar textural and structural properties. All the information as well as the complete characterization concerning this catalyst can be found in the Appendix A (see Figure A.1 and A.2).

The previous characterization highlights the favorable features of these materials in the perspective of a catalytic applications. In particular, for the conversion of dihydroxyacetone (DHA) to ethyl lactate (EL), the presence of Sn atoms inserted as single sites within the silica framework as well as the high specific surface area, the open mesoporosity, and possibly the small particle size are important requirements for a good activity. Thus, both SnSi-74 and SnSi-37 were tested as catalysts for the synthesis of ethyl lactate. The solids exhibited excellent catalytic performance in the conversion of dihydroxyacetone to ethyl lactate. The kinetic profiles of the conversion as a function of the time for the two solids are reported in Figure 2.7.

As it can be seen, the selectivity toward EL increased with time. This observation is particularly evident for the catalyst displaying higher Sn loading (Figure 2.7b) and can be ascribed to the formation of the diethyl acetal as the main intermediate of the reaction. According to the literature, the proposed reaction mechanism[132] entails the formation of two main products: ethyl lactate and the diethyl acetal of pyruvic aldehyde. As suggested, the reaction starts with the formation of a pyruvic aldehyde intermediate, which can proceed towards the lactate by rearrangement and incorporation of an ethanol molecule or towards the acetal by addition of ethanol on strong Brønsted acid

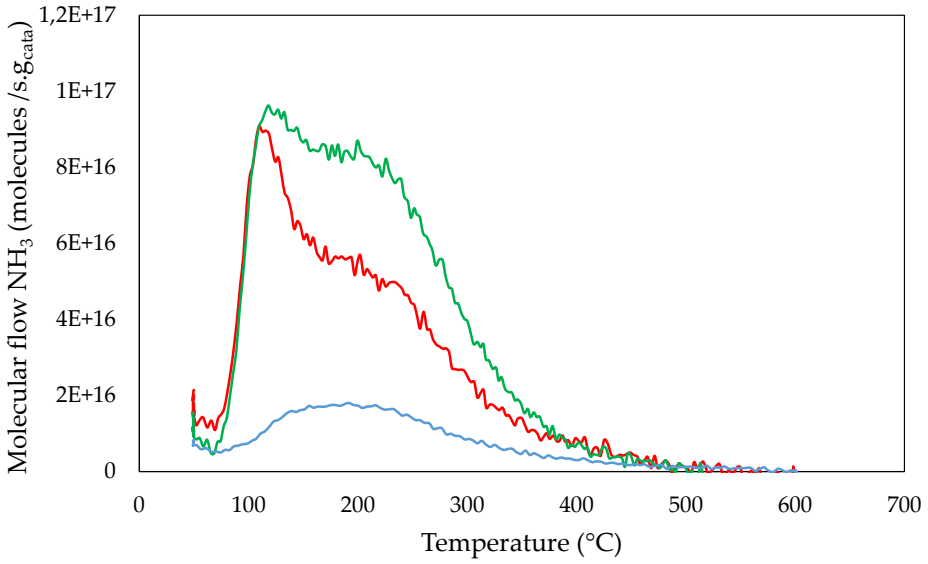

FIGURE 2.6: NH_3-TPD of the two aerosol-made catalysts and a reference catalyst. The total amount of acidic sites is determined by integrating the area under the TPD profile, after calibrating the apparatus with a diluted feed of ammonia of known composition: 220 µmol g^{-1} (SnSi-74), 330 µmol g^{-1} (SnSi-37), and 45 µmol g^{-1} (XS-Sn-MCM-41-A).

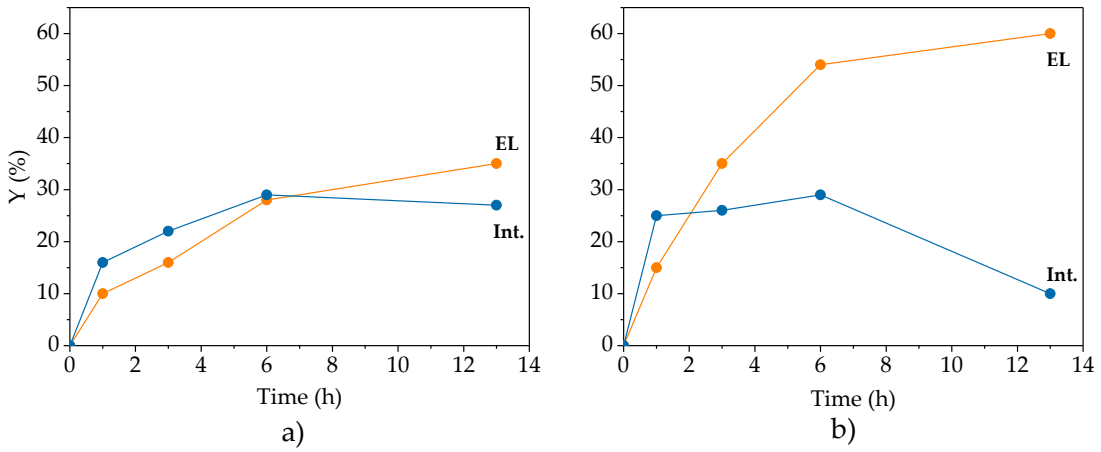

FIGURE 2.7: Kinetic study on SnSi-74 (a) and SnSi-37 (b). Conditions: 50 mg of catalyst, 5 mL of 0.2 M DHA solution in EtOH at 90 °C

sites. It is known, that the isomorphic substitution of silicon with tin, generates a combination of Brønsted and Lewis acid sites[135], thus explaining the presence of the intermediates. Despite the modest selectivity of the reaction in the first 6 h, the kinetic profiles reported in Figure 2.7a show that the yield of EL increased with time while the yield of the intermediate tends to reach a plateau after 6h of reaction. In the presence of SnSi-37 (Figure 2.7b) the yield of the intermediate species decreases after 6 h of reaction and a selectivity higher than 80% can be achieved after 12 h. This behavior can be ascribed to the reversible formation of the diethyl acetal of pyruvic aldehyde under acid catalysis[178].

Increasing the catalyst/reactant ratio, it is possible to push the reaction further. Almost total conversion of DHA with a 95% selectivity toward EL was achieved with SnSi-37 at 90 °C after 13h of reaction under appropriate conditions (100 mg of catalyst, 5 mL of DHA 0.2 M in ethanol). Comparison with recently reported active catalysts was done at lower conversion (Table 2.2). In order to have a straightforward estimation of the activity of the different solids, turnover number (TON defined as mol of DHA converted per mol of tin) was calculated as well. Moreover, the synthesis of one of the best catalysts previously reported in our research group (XS-Sn-MCM-41-A[135], entry 3 in Table 2.2) was repeated and the solid was tested under the same reaction conditions employed for SnSi-74 and SnSi-37 (compare entries 1 to 3 in Table 2.2). The tin silicates prepared via aerosol assisted procedure displayed better performance than the other tin based catalysts reported in the table. Moreover, both SnSi-74 and 37 clearly outcompete gallium and zinc silicates (compare entries 1 and 2 with 5 and 6).

TABLE 2.2: Conversion of DHA into ethyl lactate catalyzed by SnSi catalysts and comparison with literature data

Entry	Catalyst	Si/M	Conv.$_{DHA}$ (%)	Sel.$_{EL}$ (%)	TON (%)	Ref.
1	**SnSi-74**	79	34	36	173	This work
2	**SnSi-37**	41	41	40	107	This work
3	**XS-Sn-MCM-41-A**	63	24	63	113	This work
4	**XS-Sn-MCM-41-A**	65	24	69	117	Ref.[135]
5	**XS-Ga-MCM-41-H**	15	20	60	9	Ref.[11]
6	**XS-Zn-MCM-41-A**	77	26	92	63	Ref.[179]
7	**Sn-MCM-41**	54	32	94	41	Ref.[69]

Reaction condition: 50 mg of catalyst, 5 mL of 0.4 M DHA in EtOH, 6 h at 90 °C. TON =$(n_{DHAconv.}/n_{Sn})$

A direct comparison with other active catalysts reported in literature is difficult owing to the different reaction conditions in terms of temperature, reaction time, loading of active sites, alcohol used, substrate to catalyst ratio, etc. However, SnSi-74 displays better performances in terms of TON than other tin bases catalysts such as Sn-USY[180] (TON = 58, calculated for the reaction between DHA and methanol, at 90 °C, conversion after 5 h) and Sn-beta[68] (TON=120, calculated for the reaction between DHA and methanol at 80 °C, conversion after 24 h).

As indicated by characterization data, the superior activity of the aerosol catalyst may be attributed to the good Sn dispersion and its effective incorporation in the silica network, generating abundant surface acid sites. However, in the evaluation of a heterogeneous catalyst not only the activity but also the possibility of consecutive uses should be considered. SnSi-74 displayed excellent performance in the synthesis of ethyl lactate and it presented the best activity in terms of TON. It was hence selected for further investigations. The recyclability of SnSi-74 solid was tested in consecutive catalytic runs (Figure 2.8, left). Catalytic activity was maintained over 3 reaction runs, attesting of the good reusability of the catalysts. The slight decrease of TON in the third cycle could be ascribed to the presence of small amounts of organic species adsorbed on the surface of the material. In order to further prove the stability of the solids under the selected reaction conditions, leaching tests were performed as well. In this experiment, DHA conversion was evaluated after 1 h of reaction (22% of conversion), the catalyst was removed via hot filtration and

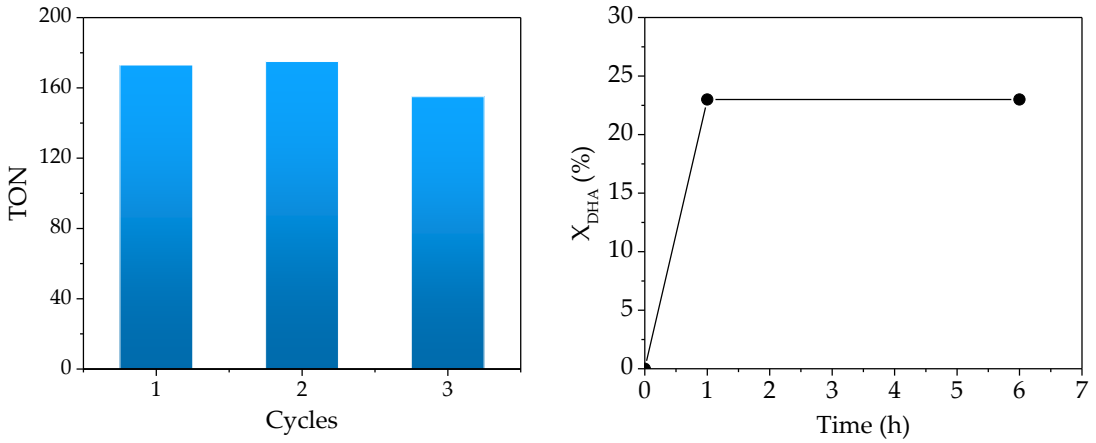

FIGURE 2.8: Recycling test of SnSi-74 catalyst (left). Conditions: 50 mg of catalyst, 15 mL of 0.4 M DHA in EtOH, 6 h at 90 °C. TON calculated as mol of dihydroxyacetone converted per mol of Sn. Leaching test of SnSi-74 catalyst (right). DHA conversion after 1h and 6h (catalyst removed). Conditions: 50 mg of catalyst, 5 mL of 0.4 M DHA in EtOH at 90 °C. (Note: conversion after 6h in the presence of catalyst reached 80%)

the filtrate was further allowed to react in the absence of catalyst and under the same reaction conditions for 5 h.

The conversion remained practically unchanged during the additional 5h reaction (conversion = 23% after 6h), demonstrating the absence of leaching of active sites and confirming that the catalytic reaction is truly heterogeneous (Figure 2.8, right).

2.3 Conclusions

In conclusion, novel mesoporous tin silicates were prepared via an easy, one-pot and continuous mode, using the aerosol-assisted sol-gel process. The synthesis of two solids (SnSi-37 and SnSi-74) bearing a different Sn loading was successfully achieved. The solids display interesting features for catalytic applications such as high surface area, regular mesoporosity and a successful incorporation of isolated Sn within the silica framework. These aerosol-made mesoporous Sn-silicates showed excellent catalytic performance in the conversion of dihydroxyacetone to ethyl lactate. The best catalyst displayed higher turnover number than the reference catalysts previously reported in literature. The catalysts do not leach and truly act in a heterogeneous mode. Moreover, it was successfully used in multiple catalytic cycles thus proving its stability under the selected reaction conditions.

Chapter 3

Mesoporous Methyl-Functionalized Sn-Silicates Generated by the Aerosol Process for the Sustainable Production of Ethyl Lactate

Abstract

In this chapter the aerosol-assisted process was used to prepare in a one-pot procedure a series of methyl-functionalized Sn-silicates with different degrees of methylation. The successful incorporation of isolated Sn as single-site within the silica matrix was confirmed via ^{119}Sn solid state NMR measurements, while ^{29}Si and ^{13}C solid state magic angle spinning NMR experiments revealed a degree of methylation close to the nominal value, hence proving the efficacy of the adopted co-synthetic approach. These materials were tested as catalysts in the conversion of dihydroxyacetone to ethyl lactate. The methylated solids display enhanced performances in terms of both activity and selectivity compared to the non-methylated analogues, highlighting the role played by the hydrophilic/hydrophobic tuning of the catalyst surface. Under proper conditions, a total conversion and a selectivity higher than 95% were achieved. Moreover, the efficient separation and reuse of the heterogeneous catalyst as well as the possibility of an easily recover of the reaction solvent result in a very low waste production protocol with an exceptionally low E factor.

The results presented in this chapter have been published in:

A. Vivian, L. Fusaro, D.P. Debecker*, C. Aprile*, Mesoporous Methyl Functionalized Sn-Silicates Generated by the Aerosol Process for the Sustainable Production of Ethyl Lactate, ACS Sustainable Chemistry & Engineering, 6 (2018) 14095-14103.

3.1 Experimental section

Preparation of the solids

Methyl-functionalized Sn-silicates (Sn-x) were synthesized from a mixture of two silica sources, tetraethyl orthosilicate (TEOS) and methyltriethoxysilane (MTES) and four degrees of functionalization have been selected: 2, 5, 10 and 30 mol% (in terms of molar ratio calculated as: MTES / (MTES + TEOS) x 100%). Pluronic F127 and P123 have been used as templating agents. Solution 1 was prepared by hydrolyzing TEOS and MTES in an HCl, 0.02 M aqueous solution (20 g). Pluronic P123 or F127 (3.9 g) was dissolved in absolute ethanol (45 g) and acid aqueous solution (HCl, 0.02 M, 8 g) to yield solution 2. Both solutions were left stirring overnight at room temperature and then tin (IV) chloride ($SnCl_4 \cdot 5H_2O$) was added to solution 1 in order to have a Si/Sn molar ratio equal to 74. Solutions 1 and 2 were mixed together and then stirred for 30 minutes. The clear solution obtained was atomized with a 6-Jet 9306A atomizer from TSI and the aerosol was dried by passing through a tubular quartz tube heated at 350 °C. The dried powders were collected on a cellulose nitrate filter and dried at 80 °C for one night. The removal of the templating agent was first attempted using solvent extraction, on a non-functionalized solid. Three different procedures were tested and the results are reported in Table 3.1.

TABLE 3.1: Solvent extraction test for the removal of the surfactant

Extraction	**Solvent**	**T** (°C)	**Residual surfact.** (%)
Batch, stirring	100 mL Ethanol + 2 mL 2 M HCl	80	9
Batch, stirring	100 mL Acetone	50	14
Soxhlet	Ethanol	80	10

Extractions performed on 250 mg of as-synthesized material; the amount of residual surfactant was quantified by elemental analysis (CHN).

The incomplete removal of the surfactant obtained by solvent extraction was overcome optimizing a mild calcination treatment at 250 °C that allowed to completely remove the templating agent while preserving the organic functionalization (see Results and discussion section). All the solids were then calcined under air at 250 °C (heating rate of 1 °C/min).

Definition and calculation of the E factor

The E(nvironmental) factor defined in the late 1980s by Roger Sheldon plays a pivotal role in defining new paradigm in the era of "Green Chemistry", where the traditional concept based on chemical yield gives way to a new one that assigns value to maximizing resource efficiency, minimizing waste and avoiding the use of hazardous and toxic chemicals. The E factor, can be defined as the actual amount of waste produced in a process in terms of mass of waste/mass of product, usually expressed as kgs/kg and allows assessing the environmental impact of a manufacturing process. It takes into account the product yield and wastes from all of the auxiliary components, e.g. solvent losses and chemicals used in work-up. In the original definition the authors[181] defined waste as "everything but the desired product", with the exception of water. An example of E factor values, in different segments of the chemical industry, is reported in Table 3.2[181].

TABLE 3.2: Examples of E factors values of chemical industry

Industry segment	**Tonnes per year**	**E factor (kg waste/kg product)**
Oil refining	10^6 - 10^8	<0.1
Bulk chemicals	10^4 - 10^6	<1 -5
Fine chemicals	10^2 - 10^4	5 - 50
Pharmaceuticals	10 - 10^3	25 - >100

A higher E factor means more waste and, consequently, greater negative environmental impact. For this reason, the ideal E factor is zero. In this chapter, the sustainability of the ethyl lactate production using methyl-functionalized tin silicates was evaluated through the calculation of the E factor. For the E-factor calculation a quantitative test was performed at 24h using 200 mg of catalyst, 360 mg of DHA in 7.8g of absolute ethanol. At the end of the test the catalyst was separated by centrifugation and ethanol was recovered by distillation. The EL isolate yield used for the E-factor estimation was obtained via GC analysis. The E factor was calculated using the following equation:

$$\frac{\sum m(raw\ materials) + \sum m(reagents) - m(product)}{m(product)} \tag{3.1}$$

3.2 Results and discussion

Two series of Sn-silicates with different degrees of methyl (Me) functionalities were synthesized using the aerosol-assisted sol-gel process in one-pot co-synthetic approach selecting a Si/Sn atomic ratio of 74[13]. To that end, an aqueous-ethanolic precursor solution containing tin(IV) tetrachloride pentahydrate, tetraethylorthosilicate (TEOS), and methyltriethoxysilane (MTES) – as the source of methyl groups – was atomized and rapidly dried in a tubular furnace set at 350 °C. It must be mentioned that the reproducibility of the synthesis is strongly related to the careful control of all the synthesis parameters (e.g. temperature, pre-hydrolysis time of the precursors, working parameters of the aerosol setup, etc.). Initially, porous Sn-based solids with a low degree of methylation (2 and 5%mol) were synthesized. The influence of two structure-directing agents from the Pluronic family (F127 and P123) on the morphological properties of the materials was studied as well. The materials were denoted as Sn-x-F127 and Sn-x-P123 (where x indicates the nominal percentage of methylation, i.e. the molar MTES / (MTES + TEOS) x 100% ratio). In order to investigate the effect of a higher amount of methyl moieties, two additional solids bearing a theoretical methylation degree of 10 and 30%mol were prepared. For this investigation Pluronic F127 was selected as templating agent. The degree of functionalization of the as-synthesized materials was assessed by quantitative solid state ^{29}Si MAS (magic-angle-spinning) NMR investigation, revealing that the methylation degree was always close to the theoretical value for all solids (see Table 3.3 and Figure A.3). The templating agent has to be removed to release the porosity, while preserving the organic-functionalization. Several procedures have been reported in literature for the removal of Pluronics from as-synthesized nanomaterials, including solvent extraction or calcination[182]. Different solvent extraction procedures, including the one reported by Zhao et al.[183] were initially considered. However, under the selected conditions the total removal of the surfactant was not achieved and a significant template residue (around 10%wt) was found. To overcome the incomplete removal of the surfactant obtained with the extraction technique, a mild calcination treatment was optimized taking inspiration from the work of Grudzien et al.[184]. For this investigation the solid with the highest Me degree (Sn-30-F127) was selected as target material and a calcination screening at different temperatures was performed. The loss of both

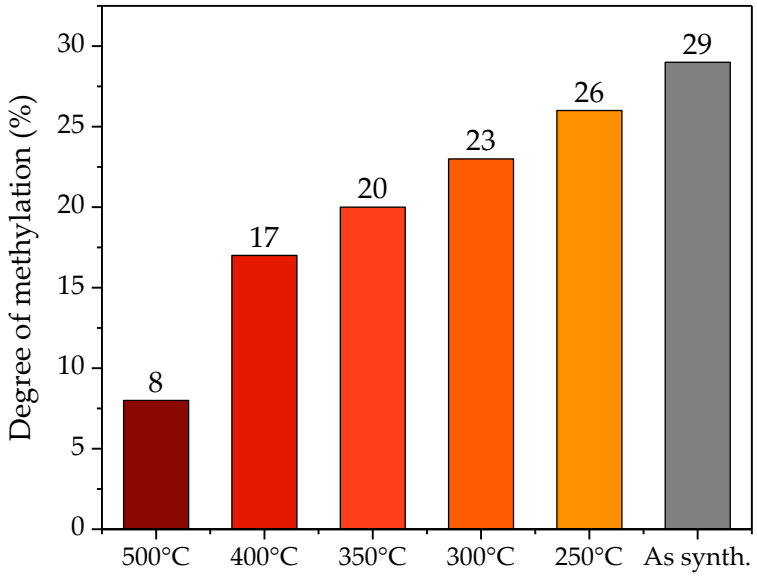

FIGURE 3.1: Calcination screening performed on Sn-30-F127 for the removal of the templating agent. The methylation degrees reported in the graph are calculated from quantitative solid state ^{29} MAS NMR spectra (direct excitation experiments).

templating agent and methyl-functionalization (Figure 3.1, A.4 and A.5) was followed by a combination of ^{29}Si and ^{13}C solid state MAS NMR. The best compromise between a complete removal of the surfactant (see Figure A.5) and only a minor loss of the methyl-functionalization was achieved with a thermal treatment at 250 °C for 8h (Figure 3.1).

Thus, all the solids were calcined at the selected temperature and, as proved by ^{29}Si solid state MAS NMR experiments (Figure 3.2, Table 3.3), the initial amount of methyl moieties was largely preserved in all materials. Similar results were obtained with Sn-x-P123 samples (figure A.6 and Table 3.3), showing that the mild thermal treatment was also applicable to this texturing agent. Figure 3.2 shows the quantitative ^{29}Si direct excitation (DE) MAS spectra of the Sn-x-F127 series, the corresponding spectra of the Sn-x-P123 series can be found in supporting information (Figure A.6). The presence of Q^4 $[(SiO)_4Si]$ (-111 ppm) and Q^3 $[(SiO)_3SiOH]$ (-102 ppm) signals can be clearly observed in all samples. The ^{29}Si spectra of methyl-functionalized solids display two peaks at -66 and -59 ppm, which can be assigned to $MeSi(OSi)_3$ (T^3) and $Me(HO)Si(OSi)_2$ (T^2) species. Due to the very low degree of functionalization in both Sn-2-F127 and Sn-2-P123, the presence of methyl groups was confirmed also by performing cross-polarization (CP) experiments (see Figure 3.2d (inset) and Figure A.6).

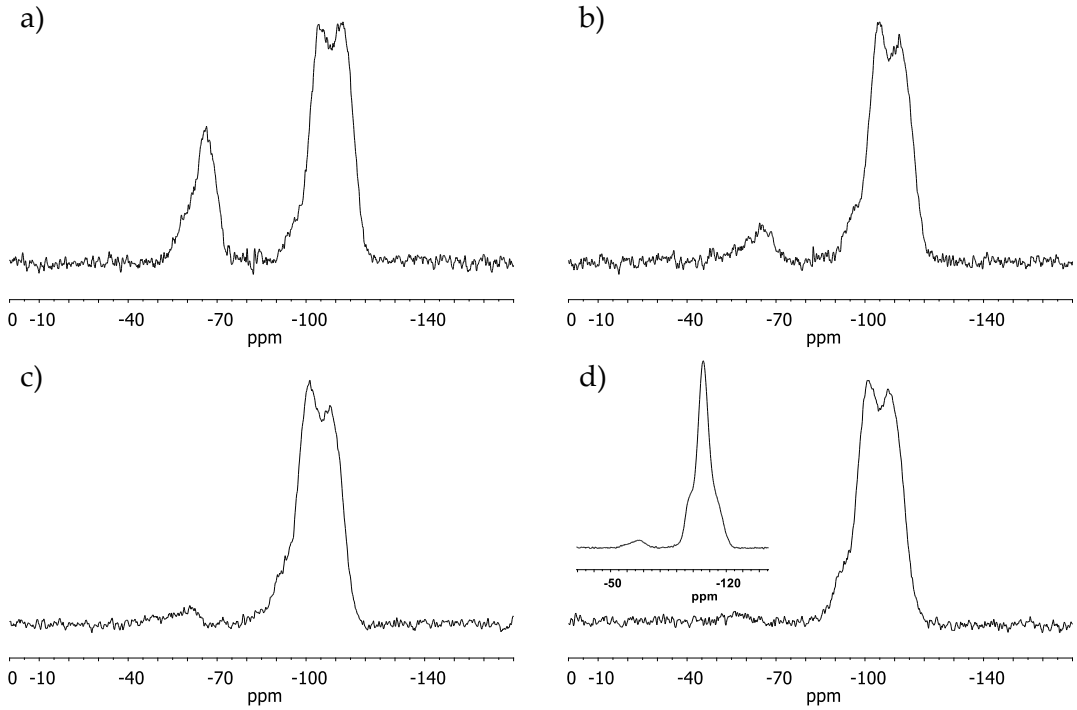

FIGURE 3.2: Solid state ^{29} MAS NMR spectra (direct excitation experiments) of methylated Sn-x-F127 after calcination treatment at 250 °C for 8h. Sn-30-F127 (a), Sn-10-F127 (b), Sn-5-F127 (c) and Sn-2-F127 (d) with cross-polarization experiment (inset).

The Sn loading was quantified by inductively coupled plasma optical emission spectroscopy (ICP-OES). The Si/Sn ratios for each material were in good agreement with the nominal composition (Table 3.3). The successful incorporation of Sn as isolated sites within the silica framework was confirmed via ^{119}Sn solid state NMR. ^{119}Sn NMR performed under static conditions of calcined solids allows evidencing a predominant insertion of Sn in tetrahedral coordination. The observed signal centered at around –700 ppm (Figure 3.3d, 3.3e and A.7) can be assigned to intra-framework Sn(IV) species connected to four silicon atoms via oxygen bridges or partially hydrated tin species with an extended coordination shell. Similar results were obtained for all the Sn-based solids. This investigation allows excluding the presence of important amount of extra-framework SnO_2 species, which would yield a signal presenting a maximum at around -600 ppm. However, considering the broad linewidth of the signals, the presence of minor amount of extra-framework SnO_2 cannot be completely excluded.

In order to elucidate the influence of the thermal treatment on the incorporation of Sn, ^{119}Sn NMR experiments were performed also on the as-synthesized

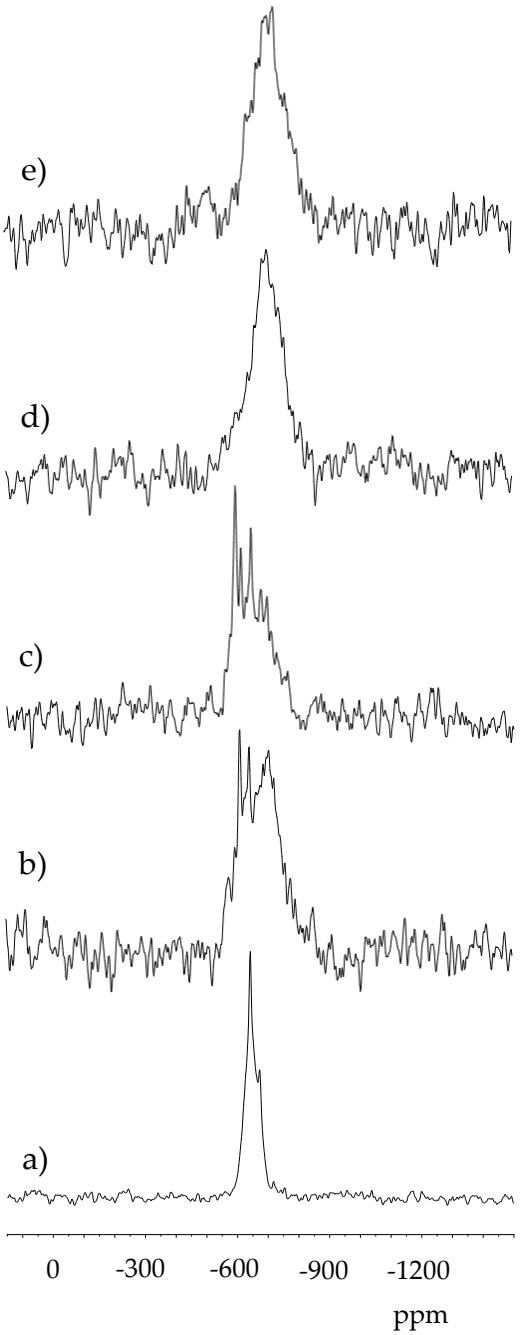

FIGURE 3.3: ^{119}Sn static solid state NMR of $SnCl_4 \cdot 5H_2O$ (a), Sn-2-P123 as-synthesized (b), Sn-2-F127 as-synthesized (c), Sn-2-P123 after calcination at 250 °C (d) and Sn-2-F127 after calcination at 250 °C (e)

samples (i.e. directly recovered from the aerosol process and before calcination). Interestingly, an evident increase of the contribution centered at -700 ppm was observed after treatment of the samples at 250 °C, together with a

shift of the signal toward lower frequency (Figure 3.3d and 3.3e). So, it appears that the thermal treatment was of crucial importance not only for the removal of the templating agent but also to favor the transition of Sn as single site within the silica structure. For comparison and to evidence even more the transition from extra- to intra-framework tin species the solid state ^{119}Sn NMR of $SnCl_4 \cdot 5H_2O$ was added as well (Figure 3.3a). The morphology of the samples was investigated via transmission electron microscopy (TEM). All solids displayed a spherical shape with a mesoporous structure and a pores size distribution in the 5-7 nm range. When F127 was used as a surfactant, a regular cubic mesostructure was obtained with an estimated pore diameter of 7 nm, throughout the particles, even when the organic-functionalization was raised to 30% (see Figure A.8). However, the materials synthesized in the presence of P123 display a substantial deformation of the mesostructure on the periphery of the particles while maintaining a more ordered organization in the core (Figure 3.4a and 3.4b). This difference between the two series of solids (Sn-x-P123 and Sn-x-F127) could be explained as a function of the different hydrophilic-hydrophobic balance of the two triblock polymers.

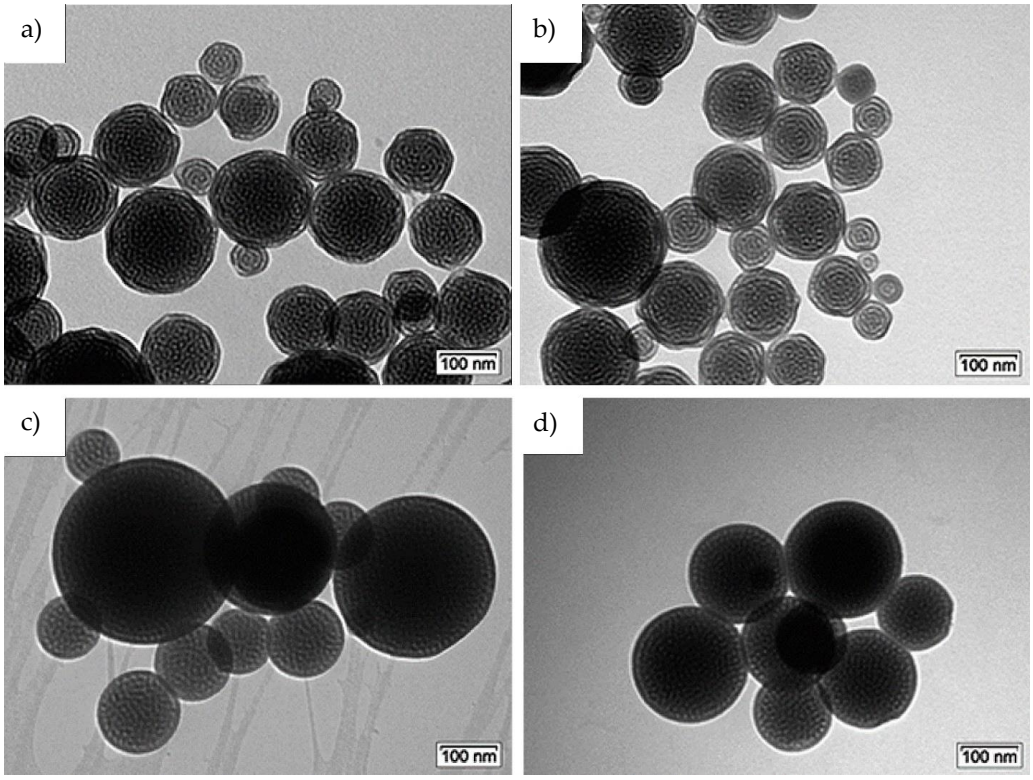

FIGURE 3.4: TEM micrographs of Sn-2-P123 (a), Sn-5-P123 (b), Sn-2-F127 (c), Sn-5-F127 (d)

Both surfactants can be defined by the general formula PEOxPPOyPEOx where PEO stands for poly(ethylene oxide) and PPO represents the poly(propylene oxide) part. In the conditions used for the synthesis of the porous solids, the central PPO block constitutes the hydrophobic core while the PEO represents the hydrophilic shell. The lower amount of hydrophilic units in the P123 may be responsible of an increased affinity with the hydrophobic methyl groups of the MTES which could be oriented toward the hydrophobic shell of the micelles causing a structural deformation of the final solid[159]. The influence of the MTES/TEOS ratio on the phase behavior can be explained since the methyl group is hydrophobic enough to exhibit cosurfactant properties. It will be preferentially adsorbed close to the hydrophobic PPO portion of the micelles and therefore cause a decrease in the interfacial curvature[185, 186], favoring probably the formation of a lamellar phase phase over the hexagonal phase[187]. The low angle powder XRD patterns of Sn-x-P123 materials (Figure 3.5) featured mainly first order d_{100} diffraction peaks (with a d-spacing of 9 nm) typical of ordered mesostructured oxides with 'wormlike' pore channel structures, as expected for materials assembled using a non-ionic surfactants[188]. Particles templated with F127 show one diffraction peak (d_{110} = 11.2 nm) consistent with a face-centered-cubic (FCC) structure[189].

The textural properties of the solids were confirmed by N_2 physisorption measurements. Both solids displayed a type-IV isotherm characterized by an evident H2 hysteresis loop. Barrett-Joyner-Halenda (BJH) analysis, performed

TABLE 3.3: Physicochemical properties of methylated Sn-silicates

Material	**S_{BET}** ($m^2\,g^{-1}$)	**MPS** (nm)	**PD** (nm)	**PV** ($cm^3\,g^{-1}$)	**% Me.** (raw)	**% Me.** (after calc.)	**Si/Sn**
Sn-30-F127	540	160	5.0	0.44	29	26	71
Sn-10-F127	570	175	6.8	0.46	10	9	80
Sn-5-F127	550	185	7.0	0.41	7	4	81
Sn-2-F127	560	170	6.7	0.47	3	2	86
Sn-5-P123	470	180	6.4	0.60	4	3	77
Sn-2-P123	400	185	6.3	0.50	3	2	76

S_{BET}: specific surface area; MPS: mean particle size; PD: pore diameter; PV: pore volume; Si/Sn determined by ICP-OES analysis; %Me: degree of methylation determined by ^{29}Si solid state DE-MAS NMR

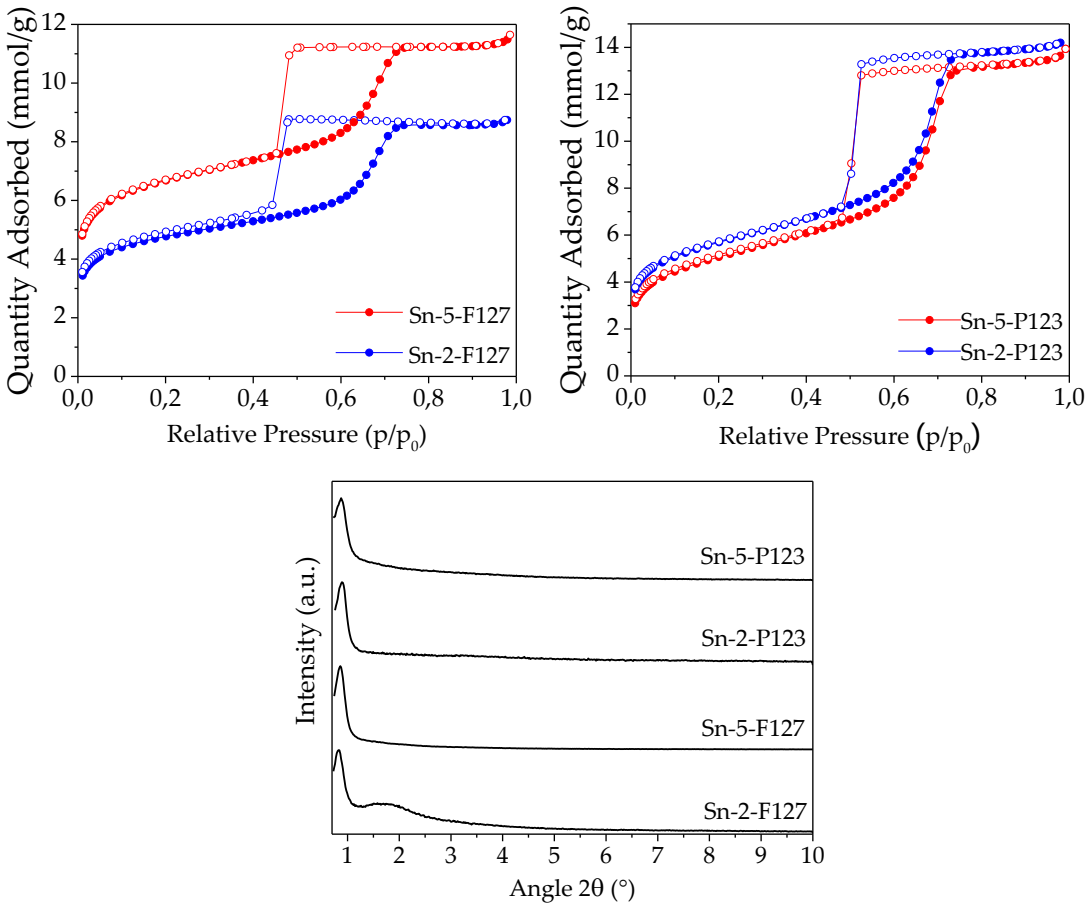

FIGURE 3.5: Nitrogen adsorption/desorption isotherms of Sn-x-F127, Sn-x-P123 solids and Small-angle XRD patterns

on the adsorption branch of the isotherm, evidenced a narrow pore size distribution (PSD) in good agreement with TEM observations. An overview of the textural properties of methylated Sn-silicates is reported in Table 3.3.

The two series of methylated Sn-silicates, displaying successful incorporation of Sn as single site in the silica matrix, high specific surface area and methyl moieties were tested in the conversion of dihydroxyacetone to ethyl lactate (Table 3.4). From a preliminary comparison between Sn-x-F127 and Sn-x-P123 bearing 2 and 5% of methyl-functionalization, it emerged that the solids synthesized using F127 as templating agent display better catalytic performances (compare entries 1 with 3 and 2 with 4 in Table 3.4). The lower activity of the Sn-x-P123 catalysts may be ascribed to the substantial deformation of the surface morphology observed in presence of P123 as well as the slightly lower specific surface area. No relevant improvement in the catalyst performance where observed in presence of Sn-10-F127 (see entry 5). A higher

content of methyl groups in the formulation leads to a lowering of the ethyl lactate yield (see entry 6). Despite the rather high selectivity, the presence of an intermediate (diethyl acetal of pyruvic aldehyde) was always observed.

This can be explained considering the mechanism of the reaction (reported elsewhere) as well as the combination of Brønsted and Lewis acid sites generated by isomorphic substitution of silicon with tin[69]. However, it is worth to mention that a total conversion with a selectivity higher than 95% can be achieved by slightly modifying the reaction conditions (*vide infra*). To verify the reproducibility of the catalytic results, the materials were tested three times under the same reaction conditions. The associated error calculated was around 2%, proving the reproducibility of the tests. In light of these results, the more performing Sn-2-F127 and Sn-5-F127 materials were compared with a non-methylated analogous (Sn-0-F127) synthesized under the same conditions. The full characterization of Sn-0-F127 solid can be found in Appendix (Figure A.9). From this comparison emerged a positive influence of the methylation on the performances of the catalysts (compare entries 1-2 with entry 4 in Table 3.5) both in terms of yield and selectivity. It is important to underline that even a very low degree of methylation was enough to enhance the catalytic activity of the solids.

However, the comparison between the methylated samples and the non-methylated reference catalyst (Sn-0-F127) should be made with care. Indeed, the methylated catalysts were calcined at 250 °C, while the non-methylated solid was directly calcined at 550 °C as in our previous works (entry 4, Table

TABLE 3.4: Catalytic activity of methylated Sn-silicate catalysts in the conversion of DHA to EL

Entry	**Catalyst**	**Calc. T** (°C)	**Yield.**$_{EL}$ (%)	**Conv.**$_{DHA}$ (%)	**Sel.**$_{EL}$ (%)	**TON** (%)
1	**Sn-2-P123**	250	27	39	68	67
2	**Sn-5-P123**	250	31	42	73	74
3	**Sn-2-F127**	250	46	62	76	127
4	**Sn-5-F127**	250	50	65	76	125
5	**Sn-10-F127**	250	50	64	78	120
6	**Sn-30-F127**	250	33	47	69	90

Reaction conditions: 50 mg of catalyst, 5 mL of 0.4 M DHA solution in absolute ethanol, 6 h at 90 °C under 1200 rpm stirring. TON $=(n_{DHAconv.}/n_{Sn})$

TABLE 3.5: Catalytic activity of methylated Sn-silicate catalysts in the conversion of DHA to EL and comparison with non-methylated solid

Entry	Catalyst	Calc. T (°C)	Yield.$_{EL}$ (%)	Conv.$_{DHA}$ (%)	Sel.$_{EL}$ (%)	TON (%)
1	**Sn-2-F127**	250	46	62	76	127
2	**Sn-5-F127**	250	50	65	76	125
3	**Sn-5-F127**(a)	250	89	99	76	45
4	**Sn-0-F127**(b)	550	22	37	60	67
5	**Sn-0-F127**(b)	250	28	43	65	76
6	**Sn-2-F127**	550	30	51	59	104
7	**Sn-MCM-41**[69]	550	30	32	94	37
8	**Sn-MCM-41**[69](a)	550	98	100	98	30

Reaction conditions: 50 mg of catalyst, 5 mL of 0.4 M DHA solution in absolute ethanol, 6 h at 90 °C under 1200 rpm stirring. (a) 200 mg of catalyst, 5 mL of 0.4 M DHA solution in absolute ethanol, 24h at 90 °C under 1200 rpm stirring, (b) Non-methylated material synthesized in the same condition as entry 1-2. TON =$(n_{DHAconv.}/n_{Sn})$.

3.5). So, an additional test was performed after calcining the Sn-0-F127 material at 250 °C (entry 5, Table 3.5). Only a minor difference in the activity of the catalyst was observed (compare entries 4 and 5, Table 3.5), strengthening the positive results obtained with methylated silicates. As a countercheck, a significant loss of activity was observed when testing Sn-2-F127 (entry 6) after a thermal treatment at 550 °C where a complete removal of the methyl-functionalization is expected. It is relevant to highlight that the calcination may affect also the physicochemical properties of the materials such as specific surface area and surface hydroxyl content. For this reason, to even better isolate and evidence the influence of the surface methylation the activity of Sn-0-F127 (entries 5 and 6) and of Sn-2-F127 (entries 1 and 6) was normalized with the specific surface area (Figure 3.6) both after calcination at 250 °C and 550 °C.

From this analysis, the catalyst Sn-2-F127 again emerged as the most active when the surface methylation is preserved at 250 °C. From a direct comparison with an active catalyst reported in literature (Table 3.5), the methylated solids displayed better performances in terms of TON under the same reaction conditions (compare entries 2 and 3 with entries 7 and 8). To further support the importance of the methylation on ethyl lactate yield, different thermal treatments at increasing temperature were performed on both Sn-2-F127 and

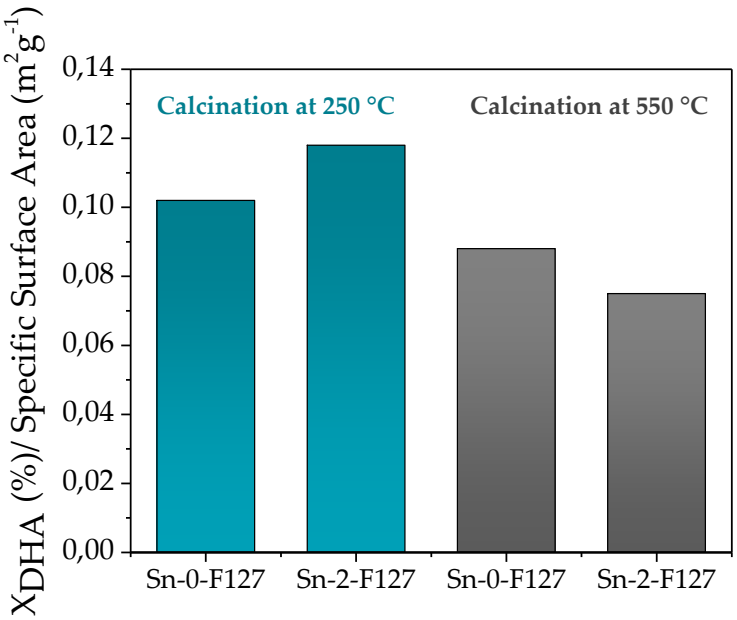

FIGURE 3.6: Activity comparison of Sn-0-F127 and Sn-2-F127 calcined at different temperatures normalized by the specific surface area.

Sn-5-F127 (Figure 3.7).

A progressive decrease in the catalytic activity of the solids was observed with increasing calcination temperature which can be related to the progressive removal of the organic functionalities. The enhanced activity of the methylated materials could be ascribed to the lower interaction of water with the more hydrophobic surface of the catalysts. Water molecules represent the side

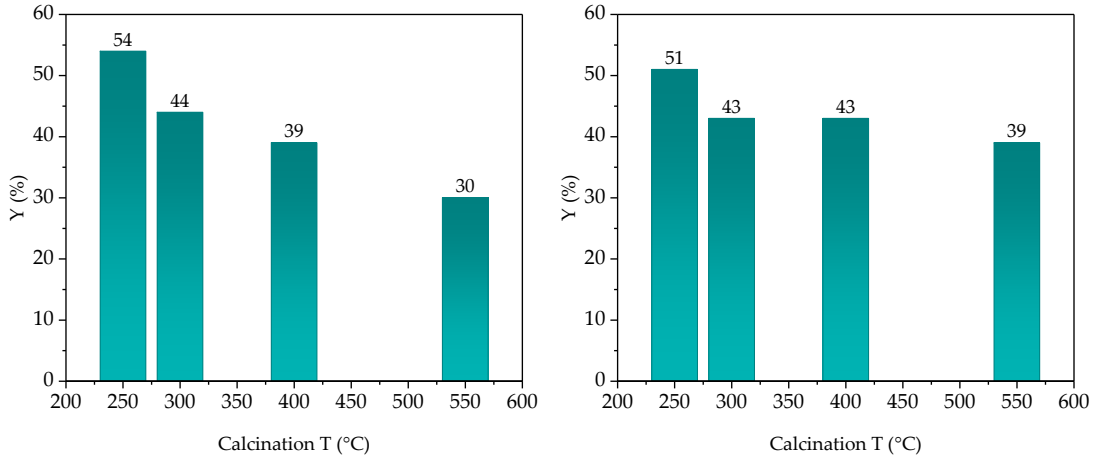

FIGURE 3.7: Influence of the calcination temperature on the activity of Sn-2-F127 (left) and Sn-5-F127 (right) catalysts. Reaction conditions: 50 mg of catalyst, 5 mL of 0.4 M DHA solution in absolute ethanol, 6 h at 90 °C.

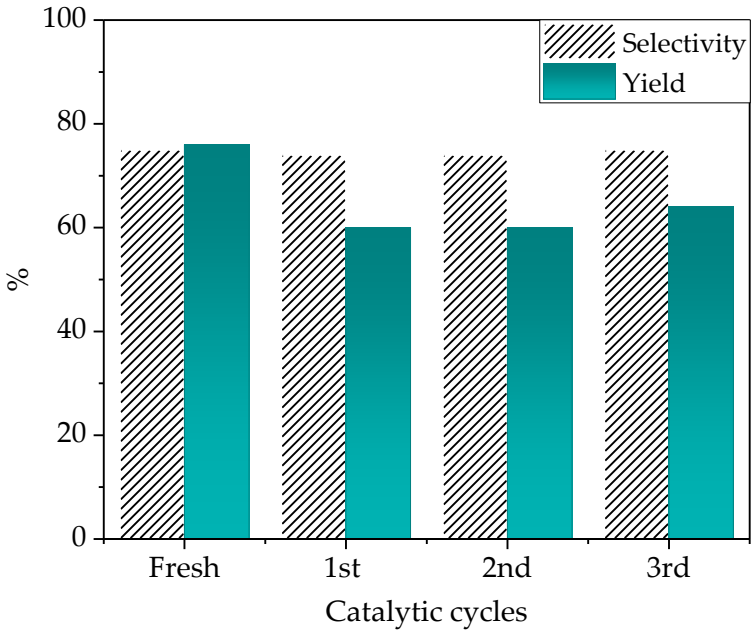

FIGURE 3.8: Recycling test of Sn-5-F127. Conditions: 100 mg of catalyst, 100 mg of DHA in 5mL EtOH, 3h at 90 °C.

product of the synthesis of EL. As previously discussed, the local removal of water in proximity of the active sites would shift the dehydration equilibrium through the formation of the PA intermediate with a consequent increase of the overall EL yield.

However, at relatively high methylation degrees, surface methylation seemed to have a detrimental effect, possibly related to the fact that a lower proportion of Sn sites are available at the surface or that the adsorption of a hydrophilic substrate such as DHA is hindered. A good compromise is, hence, achieved in presence of Sn-5-F127 which displays a relatively low methylation degree. These results further support the importance of a precise tuning of the hydrophobic/hydrophobic balance of the catalyst surface[116, 148, 164]. The excellent activity of the Sn-5-F127 catalyst was further evidenced with a quantitative experiment. An almost total conversion of DHA with a 92% selectivity toward EL was achieved at 90 °C after 24 h of reaction increasing the catalyst/reactant ratio (see experimental). This test was also selected to evaluate the sustainability of our ethyl lactate production process. After reaction, the catalyst was removed by centrifugation and the solvent was recovered through distillation. The E-factor was calculated following the formula: E-factor = [(0.360g DHA + 7.8g EtOH – 6.2g EtOH recovered by distillation – 0.418g EL) / 0.418g EL] = 3.7.

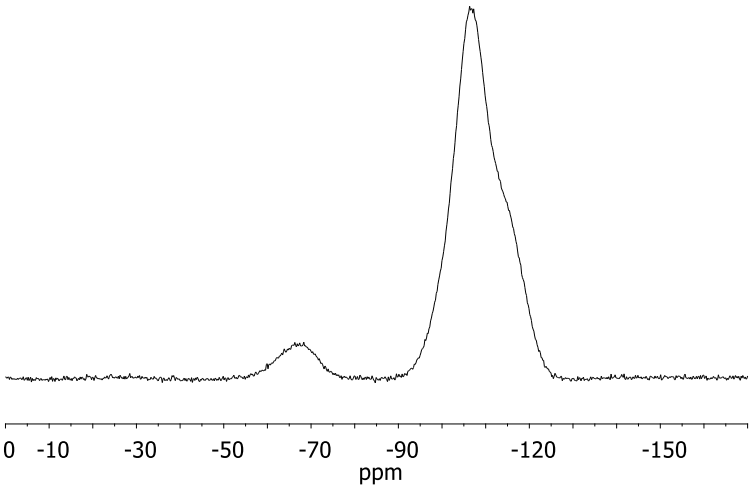

FIGURE 3.9: Solid state ^{29}Si MAS NMR spectrum (cross-polarization experiment) of Sn-5-F127 after the 3rd recycle

The efficient separation and reuse of the heterogeneous catalyst as well as the possibility to easily recover the reaction solvent result in a very low waste production protocol. A promisingly low E-factor was obtained, competitive with the E factor reported in Table 3.2 for the industrial production of bulk chemicals. When working in heterogeneous conditions, conversion, TON and selectivity do not represent the only parameters that should be considered. A key role is played by the stability of the catalyst under the reaction conditions which determines the possibility to reuse it in multiple catalytic cycles, or to envisage the design of a continuous flow process. The reusability of the Sn-5-F127 solid was investigated in consecutive runs (Figure 3.8). After each cycle the catalyst was separated via filtration from the reaction mixture, washed and thermally regenerated (see experimental section). From this study emerged that the good selectivity of the catalyst was preserved with the cycles, while the activity suffered of a slight decrease after the first run followed by a stabilization of the catalytic performances. The initial activity drop is not ascribed to a partial removal of the Me groups that would occur during regeneration since ^{29}Si solid state MAS NMR spectroscopy (see Figure 3.9) revealed a constant loading of methyl moieties even after the 4th cycle. Hence, it is put forward that the decrease in EL yield after the first cycle is linked to the presence of organic species adsorbed on the surface of the material. It is indeed known from the literature[11] that a full regeneration of similar stannosilicate materials can be achieved with a thermal treatment at higher temperature (>300 °C), which would however not be applicable in the present case as the methyl groups have

to be preserved. In order to further prove the stability of the solids under the selected reaction conditions, a hot filtration test was performed on Sn-5-F127. After 1 h of reaction, the conversion of DHA was evaluated and the catalyst was removed via hot filtration. The filtrate was further reacted in the absence of catalyst under the same reaction conditions for 5 h. The absence of leaching of active sites (Figure 3.10) was confirmed by the unchanged conversion obtained after 5h of reaction, demonstrating the stability of the incorporated metal sites.

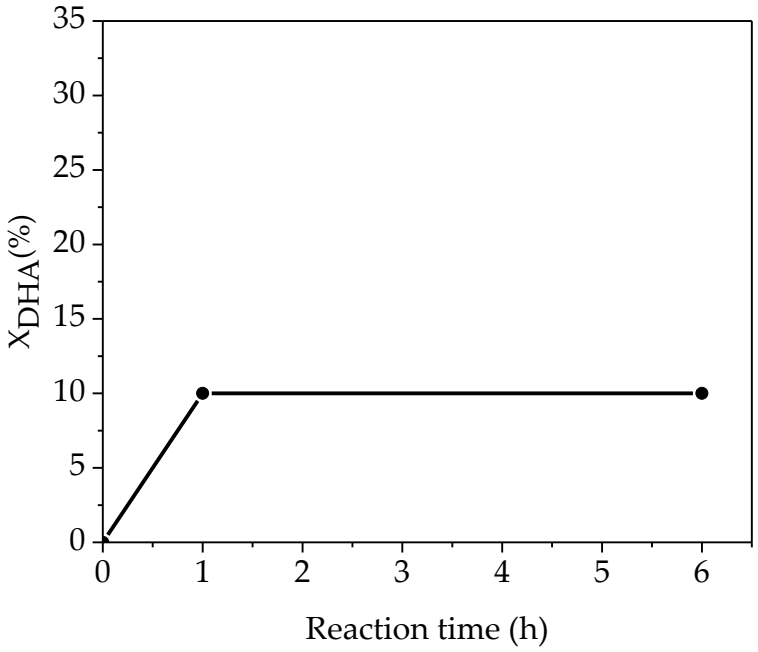

FIGURE 3.10: Hot filtration with Sn-5-F127 as catalyst. DHA conversion after 1h and 6h (catalyst removed).

3.3 Conclusion

The aerosol-assisted sol-gel process was used to synthesize a series of Sn-silicates with different degrees of methylation in a co-synthetic approach. A simple procedure for the effective removal of the surfactant was optimized using a mild calcination treatment. The materials displayed promising features for catalytic applications such as high specific surface area, controlled mesoporosity and narrow particles size distribution. A successful incorporation of isolated Sn as single site within the silica framework was confirmed via

^{119}Sn solid state NMR. Moreover, ^{29}Si and ^{13}C solid-state MAS (magic-angle-spinning) NMR experiments revealed a degree of methylation close to the theoretical value, hence proving the efficacy of the adopted procedure. Methylated Sn-silicates were tested in the conversion of dihydroxyacetone to ethyl lactate. A positive influence of the methylation on the performances of the catalysts presenting a low degree of functionalization in terms of both activity and selectivity compared to the non-methylated solid was proved. Furthermore, it was observed that even a very low degree of methylation (i.e. 2%) is effective to enhance the catalytic performance of the materials. In particular, the best results were obtained with the solids synthesized using F127 as templating agent. In order to further prove the stability of the catalysts under the selected reaction conditions, hot filtration tests were performed, demonstrating the absence of leaching of active sites. Moreover, the best catalyst was successfully used in multiple catalytic cycles thus proving its stability under the selected reaction conditions.

Chapter 4

Synthesis and In-Depth Characterization of Ga-Based Structured Catalysts: Enhancing Glycerol Conversion

Abstract

Mesoporous Ga-silicates were efficiently prepared using a sustainable and continuous synthesis procedure. The novel solids showed record activity in the synthesis of solketal from glycerol and acetone. Three different Si/Ga ratios of 34, 74 and 148 were investigated and all materials displayed favorable features for catalytic applications such as high specific surface area and calibrated mesoporosity. The insertion of Ga predominantly as single site in tetrahedral coordination in the silica framework was elucidated by XPS, using the Auger parameter of Ga in a Wagner plot representation. The speciation of Ga was further clarified using solid state ^{71}Ga NMR spectroscopy, confirming the formation of mainly isolated Ga species. Consistently, the aerosol-made Ga-silicates displayed outstanding turnover frequencies (up to 677 h^{-1}) and selectivity, markedly outcompeting other reference metallosilicate catalysts reported in literature. Moreover, the most active catalyst was successfully reused in multiple catalytic cycles thus proving its stability under the selected reaction conditions.

The results presented in this chapter have been submitted in:

Vivian, A., Soumoy, L., Fusaro, L., Louette, P., Felten, A., Debecker, D.P.*, Aprile, C.*, Synthesis and in-depth characterization of Ga-based structured catalysts: enhancing glycerol conversion, (2019) Applied Catalysis B: Environmental

4.1 Experimental section

Synthesis of Ga-silicates

Solution A was prepared by pre-hydrolysis of TEOS (97%; $5.5 \cdot 10^{-3}$ mol; 12 g, TCI) in HCl 0,01 M (0,6 mol; 20 g; pH 2). Solution B was prepared by solvating the structuring agents ($0.68 \cdot 10^{-3}$ mol; 3.9 g Pluronic P123, Sigma Aldrich) in absolute ethanol (45 g) and HCl 0.01 M (0.22 mol; 8 g; pH 2). Solutions A and B were stirred (300 rpm) at room temperature for 40 minutes and 15 hours, respectively. The gallium precursor ($Ga(NO_3)_3 \cdot 8H_2O$, ROTH) was then added to solution A at the desired Si/Ga molar ratio (the amount of Ga in the metal precursor was determined by ICP-OES). When the metal precursor was dissolved, solution B was added to solution A and the mixture was stirred for 30 minutes (300 rpm). The sol was then atomized (2 bar) using a TSI 6-Jet 9306A atomizer, resulting in aerosol droplets that were dried by passing through a quartz tube heated to 350 °C. The obtained powder was collected on a cellulose filter (0.45 µm), dried overnight at 80 °C and then calcined in air at 550 °C for 5 hours (ramp: 1 °C/min).

Synthesis of Ga-impregnated

A gallium nitrate solution was prepared by adding 500 µL of 0.02 M HCl and then 1 mL of absolute ethanol to $Ga(NO_3)_3 \cdot xH_2O$ (25 mg ; Si/Ga = 37). In a 10 mL beaker, 150 mg of a silica-based aerosol solid was impregnated, drop by drop, with the gallium nitrate solution. The catalyst was then dried in an oven at 65 °C for two hours, and then calcined in air at 550 °C for 5 h.

Auger parameter and Wagner plot

The definition of the Auger parameter[190] is reported in equation (4.1):

$$\alpha = E_K(C_1C_2C_3) - E_K(C) \tag{4.1}$$

where $E_K(C_1C_2C_3)$ is the kinetic energy of the Auger transition involving three electrons from C_1, C_2, C_3 core levels and $E_K(C)$ is the kinetic energy of the photoelectron from core level C. The emission of an Auger electron results from a relaxation mechanism. After the ionization of a core level, an outer shell electron can fill the core hole, resulting in the simultaneous emission of an Auger electron from a higher orbital. From the definition of the original Auger parameter, Gaarenstroom and Winograd[191] proposed the modified Auger parameter (α'), independent of the X-ray source and calculated as follows, where $E_B(C)$ is the binding energy of the C level:

$$\alpha^{'} = \alpha + h\nu \tag{4.2}$$

$$\alpha^{'} = E_K(C_1C_2C_3) - E_B(C) \tag{4.3}$$

Since any shifts due to surface charging will be of the same magnitude, but of opposite direction in each of these two components, they will be automatically cancelled out in $\alpha^{'}$ making the determination of this parameter more accurate especially in the case of insulating and semiconducting materials. It is usually accepted, following the derivation by Moretti[190, 192], that the $\Delta\alpha^{'}$ between two chemical states can be written as:

$$\Delta\alpha^{'} \approx 2\Delta R \tag{4.4}$$

Where ΔR is the shift in the polarization energy at the core-ionized atom [190, 192]. Equation (4.4) provides an estimation of the final state effects. Final state effects result from changes in polarization within the electron cloud of the atom after the photoemission and from relaxation of the surrounding atoms. Final state effects are often more relevant when dealing with compounds that have the potential for significant polarization[193]. The graphical representation of the most intense photoelectron line binding energies (abscissa) versus the kinetic energy position of the sharpest Auger line (ordinate) is known as a Wagner plot. The Auger parameter is the intercept of the linear relationship in equation (4.5):

$$E_K = \alpha^{'} - E_B \tag{4.5}$$

and can be represented in a Wagner plot on straight lines with slope 1. Moreover, it is possible to show that the relation between E_K and E_B in a Wagner plot can be expressed by the equation (4.6)[190, 192]:

$$E_K = [const + 2(V_M + kQ)] - 3E_B \tag{4.6}$$

$$I = [const + 2(V_M + kQ)] \tag{4.7}$$

The value [const + 2(V_M + kQ)] is related to the initial state of the ionized atom, where V_M is the local Madelung potential, Q is the ground-state valence charge and k is the change in core potential resulting from the removal of a valence electron[192]. Equation (4.6) shows that compounds with similar initial state effects will appear in a Wagner plot on a straight line with slope 3.

Initial state effects can be seen as shifts in the orbital energies of an atom before it is subject X-ray irradiation. These effects are generally considered to represent the "chemical shift" as a result of ground state electronic structure and are a function of the valence structure of the core atom. These shifts are related to the electronic states and structural parameters of the bonded atoms. The Auger parameter and the Wagner plot representation has been used for multiple elements to study the dependence of the local electronic structure on the atomic environments. In this chapter, the Auger parameter and the Wagner plot have been used to investigate the single-site insertion of Ga in the silica matrix of the synthesized solids.

4.2 Results and discussion

The aerosol-assisted sol-gel process was employed to synthesize three different Ga-silicates, bearing respectively a nominal silicon to gallium ratio of 37 (Ga-37), 74 (Ga-74) and 148 (Ga-148). All the materials were characterized using several techniques, inter alia, transmission electron microscopy (TEM), X-ray photoelectron spectroscopy and ^{71}Ga solid-state NMR spectroscopy, N_2 physisorption, and ICP-OES. All solids consist of spherical particles originating from the very fast drying of the atomized aerosol droplets (Figure 4.1). The thermal removal of P123, used as templating agent, allows obtaining well visible "wormlike" mesopores of 6-7 nm in the core together with lamellar domains in the external part of the particles. The Ga loading was quantified by inductively coupled plasma optical emission spectroscopy (ICP-OES) and the resulting Si/Ga ratios for all the materials were in good agreement with the nominal composition (Table 4.1). An in-depth characterization to assess the coordination environment of the Ga metal centers present in the silica matrix is of fundamental importance. In this work, the chemical environment of gallium for all the synthesized solids was elucidated using both X-ray photoelectron spectroscopy (XPS) and solid-state ^{71}Ga NMR.

The XPS results for the solid Ga-148 are not presented due to the too low Si/Ga ratio, close to the lower limit of sensitivity. Hydrated gallium oxide (Ga_2O_3) was chosen as the reference compound and an additional material called "Ga-impregnated" was synthesized taking inspiration from Liu et al.[194] to obtain extra-framework gallium species. This material was synthesized by

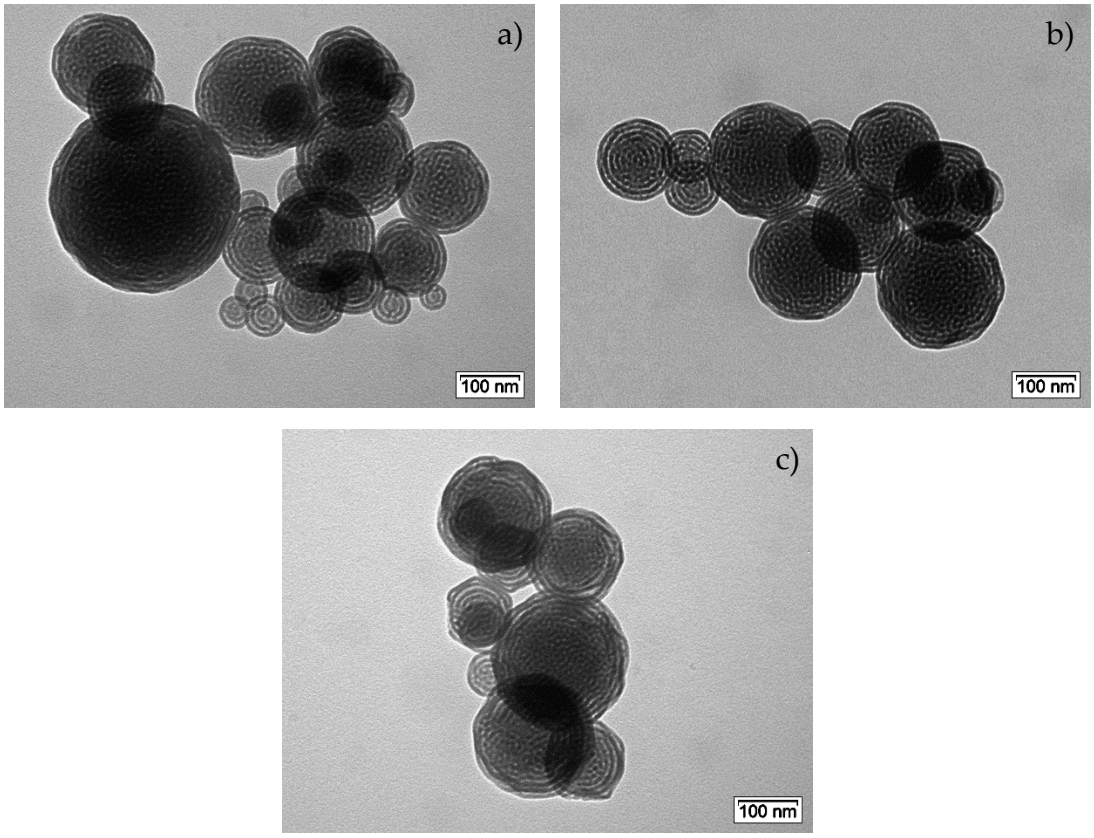

FIGURE 4.1: TEM pictures of Ga-37 (a), Ga-74 (b) and Ga-148 (c) calcined at 550 °C

impregnating an aerosol material consisting of pure silica with a gallium nitrate solution to obtain a theoretical Si/Ga ratio of 37 (see experimental section). The XPS analysis of gallium core levels 2p in Ga-37, Ga-74 and Ga_2O_3 solids do not allow to differentiate significantly the energy contributions associated with the different Ga species (see Figure 4.2). In the literature, only few studies address the determination of the chemical state of gallium by XPS[193, 195]. The standard use of only chemical shifts of binding energies can be in some cases difficult since shifts can be small and surface charging effects on insulating materials may affect the results. For this reason, to better discriminate different energy contributions the use of the Auger parameters is worth to be considered. The Auger parameter and the Wagner plot representation has been used for multiple elements to study the dependence of the local electronic structure on the atomic environments. An example is represented by the study conducted by Bourque et al.[193], where a Wagner plot was used as a tool to differentiate the chemical state of gallium in gallium-cryptand complexes.

In addition, Collard et al.[179] showed that it was possible to distinguish,

using the Wagner plot, contributions related to zinc as an isomorphic substituent of silicon atoms and extra-structural zinc within the same Zn-MCM-41 sample. The Wagner plot presented in Figure 4.3 shows the graphical representation of the most intense photoelectron line binding energies of $3d_{5/2}$ photoelectrons (x) versus the kinetic energy of the most intense core-core-core Auger line (y) for Ga-37, Ga-74, Ga-impregnated and bulk Ga_2O_3. On the Wagner plot, the modified Auger parameters are represented by the plain lines with a slope of 1 and the initial state effects I is represented by the dashed lines with a slope of 3. According to the study conducted by Wagner and Bourque et al. on the elemental Auger parameter and chemical state plots[193, 195], compounds present on a line with a slope of 3 usually show similar initial state properties (before the interaction with a photon) of the element inside the compound, while in the case of compounds gathered on a line with a slope of 1 (identical modified Auger parameters) similar final state effects are expected (after the interaction with a photon). In Figure 4.3, all the studied Ga-containing solids are sitting on the same line with a slope of 3 but on different lines with slopes of 1, which suggest that they present differences that can be explained mostly in terms of final state effects[193, 196]. These differences could be attributed to various characteristics such as the particle size, electronic valence, coordination number or the nature of ligands, although some of these can also produce

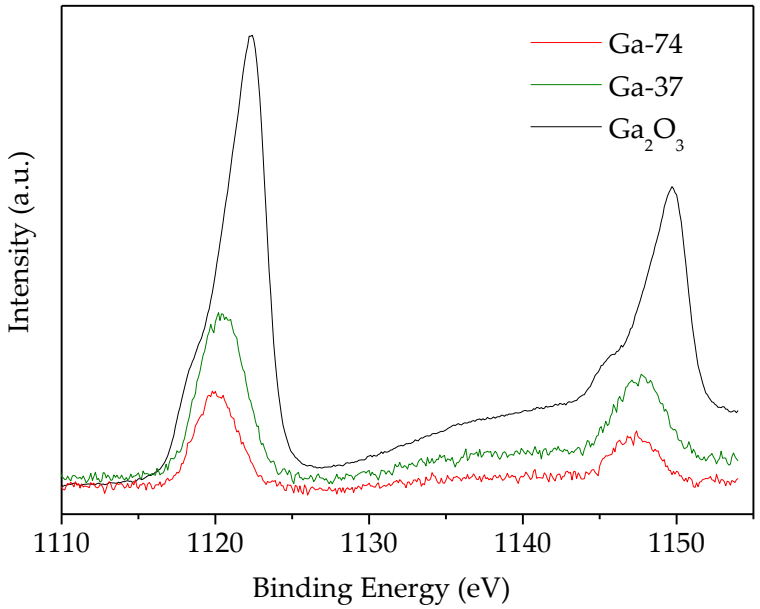

FIGURE 4.2: XPS analysis of 2p levels on Ga-74, Ga-37 and hydrated Ga_2O_3

initial state effects. In the case of gallium in hydrated Ga_2O_3, where the coordination environment of gallium is expected to be mainly octahedral, we observe the highest modified Auger parameter (1082.8 eV).
The modified Auger parameter of the impregnated Ga-solid is 1081.9 eV and this difference compared to bulk Ga_2O_3 could be attributed to the occurrence of finely dispersed gallium oxide nanoparticles interacting with the silica surface, as reported by Liu et al.[194]. The modified Auger parameter associated with Ga-37 and Ga-74 solids is clearly lower and distinct from those of Ga-impregnated and bulk Ga_2O_3. This lower value of the Auger parameter suggests the presence of tetrahedral Ga inserted in the silica framework. This interpretation is analogous to the work done by Collard et al.[179] on Zn-based materials. It can be noted that the proximity of the energy contributions associated with Ga-37 and Ga-74 solids does not allow to appreciate any difference in the chemical environment of gallium in these two materials.

To further investigate the coordination of gallium, solid state ^{71}Ga NMR spectroscopy was exploited. It is known that solid state NMR spectroscopy is a powerful tool to investigate the coordination number/geometry of metal centers inserted as single site within the silica matrix. Gallium has two NMR active nuclei, ^{69}Ga and ^{71}Ga, both with a nuclear spin of 3/2 and a natural abundance of 60.1 and 39.8 respectively. It deserves to be mentioned that due to the large second-order quadrupolar broadening, solid state investigation of $^{69/71}$Ga NMR is challenging. Hence, despite to its lower natural abundance, ^{71}Ga was selected in this work the study due to its smaller quadrupolar moment and slightly higher absolute sensitivity compared to ^{69}Ga.

In addition to the intrinsic difficulties of ^{71}Ga, our materials display an unfavorable combination of features for solid state NMR investigations: the presence of an amorphous skeleton together with a low wt% of gallium. In order to obtain precise insights on the coordination of gallium, investigations were performed under magic angle spinning (MAS) at 25 kHz at a high magnetic field (11.7 T). A sample of β-Ga_2O_3 was first measured as standard compound for our NMR investigation. The corresponding spectrum, in agreement with literature data[197], is reported in Figure A.10. Figure 4.4 shows the MAS NMR spectra of a hydrated sample of gallium oxide, Ga-impregnated, Ga-148, Ga-74 and Ga-37 respectively. The MAS NMR analysis of hydrated gallium oxide shows the presence of a signal centered at 0 ppm with respect to the reference. This signal is attributed to octahedral gallium[198]. The NMR analysis of Ga-37 revealed the presence of a major contribution centered at 140 ppm with

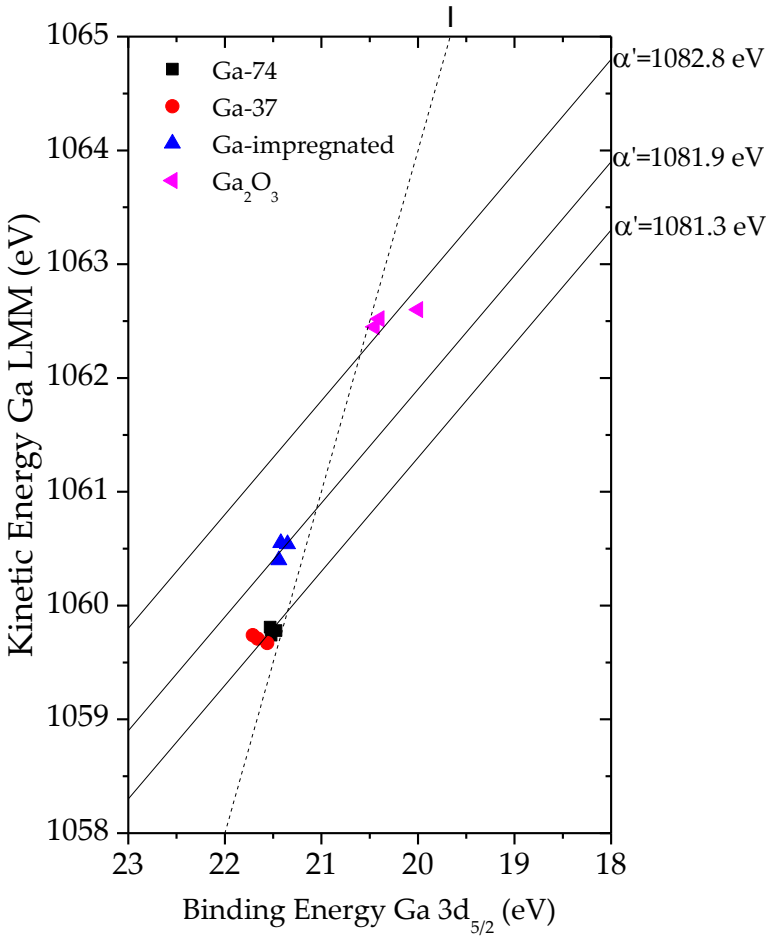

FIGURE 4.3: Wagner plot (Ga LMM Auger vs. XPS $Ga3d_{5/2}$) of Ga-74, Ga-37, Ga-impregnated and hydrated Ga_2O_3

respect to the reference. This contribution has already been observed for other gallo-silicates and is ascribed to tetra-coordinated gallium[198–200]. Nevertheless, the signal shows also a second contribution centered at 0 ppm, which can be associated to the presence of extra-framework gallium.

These extra-framework species are expected[11] to have an octahedral environment and to be catalytically inactive. The analysis of Ga-74 evidences a narrower contribution centered at 140 ppm and a contribution at 0 ppm which is proportionally less important, as compared to the case of Ga-37. This indicates the presence of a lower proportion of extra-framework Ga in Ga-74. The ^{71}Ga NMR pattern of Ga-148 was similar to Ga-74, suggesting a similar degree of dispersion in both solids. This finding clearly indicates that among the three synthesized solids a Si/Ga ratio of 74 represents the best compromise

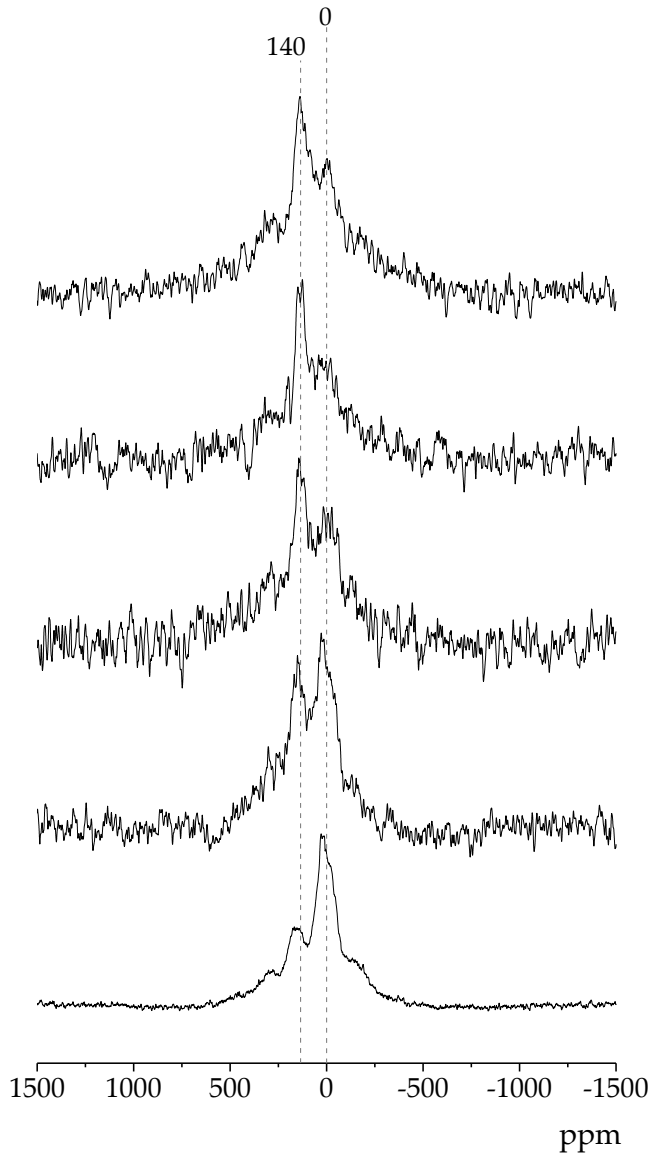

FIGURE 4.4: ^{71}Ga solid state MAS NMR spectra of hydrated Ga_2O_3 (a), Ga-impregnated (b), Ga-148 (c), Ga-74 (d) and Ga-37 (e)

between Ga loading and isomorphic substitution and highlights the Ga-74 material as the most promising catalyst of the series. As expected (see XPS investigation via Wagner plot), the Ga-impregnated solid displays a combination of intra- and extra-framework species which is intermediate between Ga_2O_3 and Ga-37. This behavior can be ascribed to the presence of finely dispersed extra-framework species at the surface, some of them in a distorted tetrahedral environment.

The textural properties and the structure of the solids were examined using N_2-physisorption and powder XRD. An overview of the textural properties of

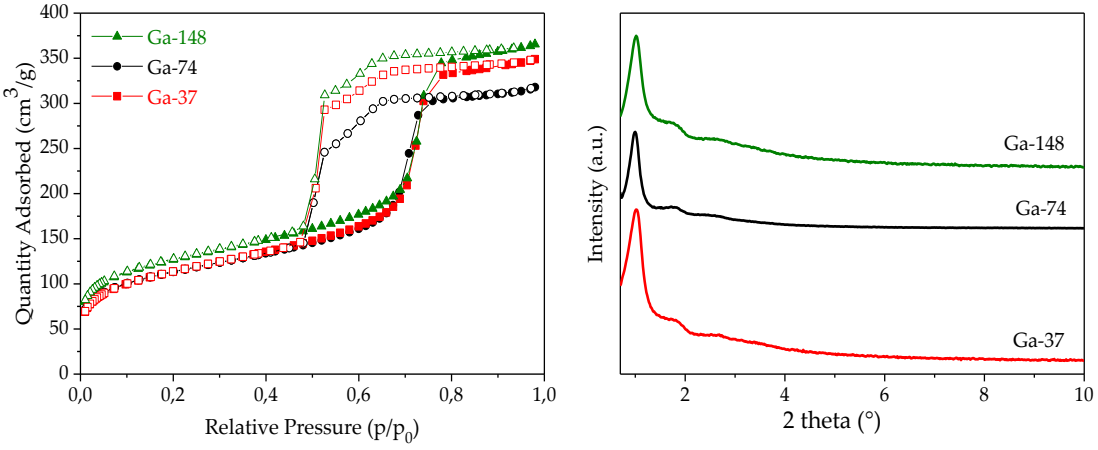

FIGURE 4.5: Nitrogen adsorption/desorption isotherms of Ga-silicate solids (left) and small-angle XRD patterns (right)

the synthesized Ga-silicates is reported in Table 4.1. All solids prepared by aerosol had similar texture with a specific surface area around 350 $m^2\,g^{-1}$ and a pore volume around 0.5 $cm^3\,g^{-1}$.

They all showed a type-IV isotherm characterized by an evident hysteresis loop that can be classified as a combination of types H1 and H2 (Figure 4.5, left). The combination of two types of hysteresis may be attributed to the presence of a combination of tubular pores opened at both ends and a more disordered porosity in good accord with TEM observations. The analysis performed using BJH on the adsorption branch of the isotherm showed a narrow pore size distribution centered at around 7.5 nm for all the solids. The low angle powder XRD patterns of the materials (Figure 4.5, right) featured an intense first order d_{100} diffraction peak centered at 2theta = 1° accounting for

TABLE 4.1: Textural properties and composition of Ga-silicate solids

Material	**S_{BET}** ($m^2\,g^{-1}$)	**PD** (nm)	**PV** ($cm^3\,g^{-1}$)	**Si/Ga**
Ga-37	350	7.5	0.5	38
Ga-74	350	7.0	0.5	79
Ga-148	380	7.7	0.5	160

S_{BET}: specific surface area; PD: pore diameter; PV: pore volume; Si/Ga determined by ICP-OES analysis

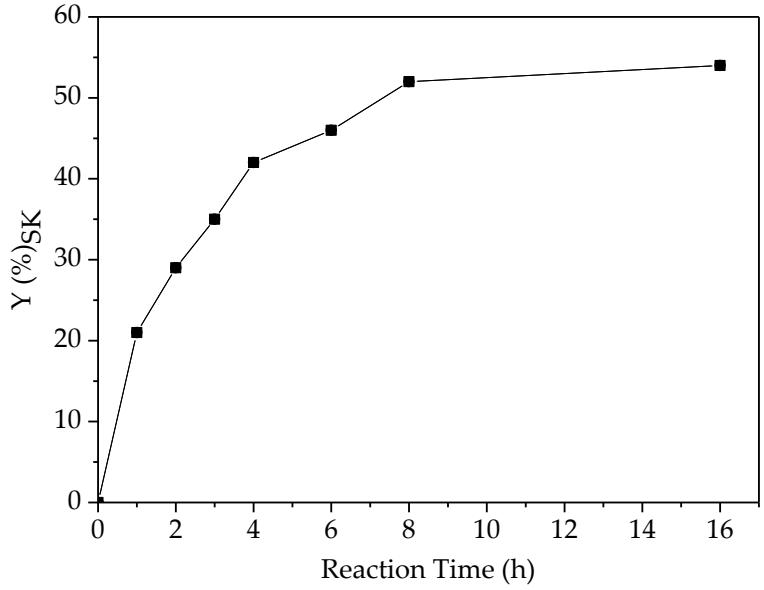

FIGURE 4.6: Kinetic study performed using Ga-74 catalyst

mesostructuration of these solids. A second weaker contribution can be observed and is assigned to the d_{110} reflection. From TEM, N_2-physisorption and powder XRD investigation, no major differences emerged comparing the morphology and textural properties of the three samples. Therefore, we can argue that raising the concentration of Ga, in the selected range, does not influence the morphology, texture and structure of the solids. Hence, the eventual catalytic differences can be mainly ascribed to different Ga loading and to different insertion/coordination of Ga in the silica structure. All the synthesized Ga-silicates present favorable features for their application in heterogeneous catalysis. The targeted reaction selected in this work is represented by the acetalization of glycerol with acetone to produce solketal. A kinetic study was performed using Ga-74 as catalyst and the formation of solketal over time was followed in the range of 1 h to 16 h, reaching a solketal yield of about 55% (Figure 4.6). Extending the reaction time did not result in a further improvement in the conversion. A similar behavior was already observed in literature[201].

This suggests that the thermodynamic equilibrium is reached and that any further improvement in solketal yield could only obtained by the modifications of reaction conditions (e.g. reactants ratio, or product removal) which can shift the equilibrium to the formation of the desired product. The kinetic study was used to select an adequate reaction time to compare the catalytic activity of the solids. A reaction time of 2h was selected as the best compromise

TABLE 4.2: Catalytic activity of Ga-silicates in the conversion of glycerol to solketal

Entry	Material	Si/Ga	Yield $_{SK}$ (%)	Sel.$_{SK}$ (%)	TOF (%)
1	**Ga-37**	38	30	85	361
2	**Ga-74**	79	28	85	677
3	**Ga-148**	160	10	79	487
4	**Ga-impregnated**	37	2	-	-
5	**Ga_2O_3**	-	2	-	-

Si/Ga ratios determined by ICP-OES analysis; Reaction conditions: 10 mg of catalyst, 0.01 mol of glycerol, 0.04 mol of acetone, 50 °C, 2 h; TOF =$(n_{solketal}/n_{Ga})h^{-1}$.

between an acceptable solketal yield (around 30%) enabling an accurate quantification and a meaningful comparison among the catalysts, but far enough from the equilibrium conversion[202]. Thus, the initial specific activity was approached by considering the activity at 2h, expressed in terms of turnover frequency (TOF, defined as moles of solketal produced per moles of Ga and per hour). To verify the reproducibility of the catalytic tests, all the solids were tested three times under identical reaction conditions. The error measured on the solketal yield was around 2%, confirming the good reproducibility of the presented tests. From a first comparison among Ga-37, 74 and 148 (Table 4.2) emerged that the catalytic activity does not increase proportionally with the gallium loading. In particular, very similar solketal yields were observed when a Si/Ga ratio of 37 and 74 were used (compare entries 1 and 2, Table 4.2). The decreased turnover number of the solid Ga-37 compared to Ga-74 can be explained considering the presence of a higher quantity of extra-framework gallium, as revealed by ^{71}Ga MAS NMR.

Extra-framework gallium species are not active in the selected target reaction, as demonstrated here experimentally with bulk gallium oxide and Ga-impregnated which displayed no catalytic activity (see entries 4 and 5, Table 4.2). Concerning Ga-148 catalyst, its decreased activity could be attributed to its low Ga loading resulting in the presence of a limited amount of Ga inserted as single sites. All the materials present a very high selectivity and the only secondary product detected was the six-membered ring compounds (2,2-dimethyl-1,3-dioxan-5-ol). The best TOF was obtained employing the Ga-74

catalyst. While we show that the reaction can be run effectively in solventless conditions, several works report the use of solvents for the selected reaction. For this reason, in order to allow a meaningful comparison of our best catalyst with reference solids reported in the literature[8, 11], an additional catalytic test was performed, using t-butanol as solvent. The results gathered in Figure 4.7 evidence the outstanding catalytic performance of Ga-74 compared not only to previously reported Ga-based catalyst but also to other metal-containing silicates reported in literature. This behavior could be due to a favorable combination of features such as high specific surface area, accessible mesoporosity and insertion of gallium mainly as single site in the silica architecture. Although the activity of a heterogeneous catalyst is an important parameter, the possibility of using the catalyst in multiple catalytic runs should not be neglected. Recycling tests for the catalyst showing the best activity (Ga-74) are presented in Figure 4.8. In order to prove the reusability of the catalyst, four consecutive catalytic tests were performed, including reactivation of the catalyst by washing with acetonitrile and calcination at 450°C for two hours (see experimental section). Recycling tests showed that Ga-74 catalyst always maintained an excellent selectivity and an almost stable catalytic activity over

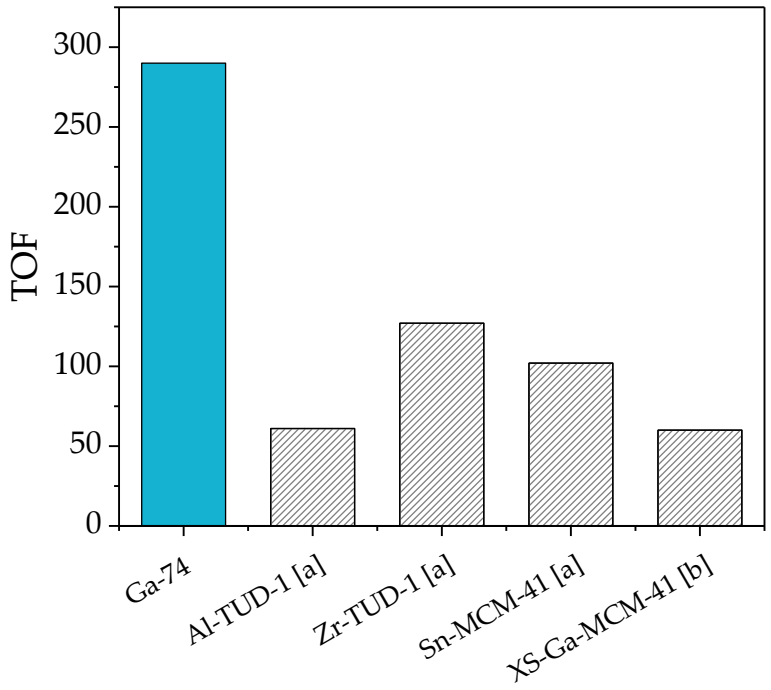

FIGURE 4.7: Catalytic activity of Ga-74 in the conversion of glycerol to solketal compared to metal-silicates reported in the literature: [a][8], [b][11]. Reaction conditions: 0.01 mol of glycerol, 1 eq. of acetone, 0.02 mol of t-butanol, 2h and 25 mg of catalyst

four cycles. The absence of leaching of gallium species in solution was verified by ICP-OES analysis on the used catalyst. At the end of the last cycle, no change was observed in term of Si/Ga ratio between the fresh and reused catalyst. In addition, the characterization of the catalyst after recycle via N_2 physisorption and ^{71}Ga NMR did not display major differences in comparison to the fresh solid (see Figure 4.9 and Table 4.3).

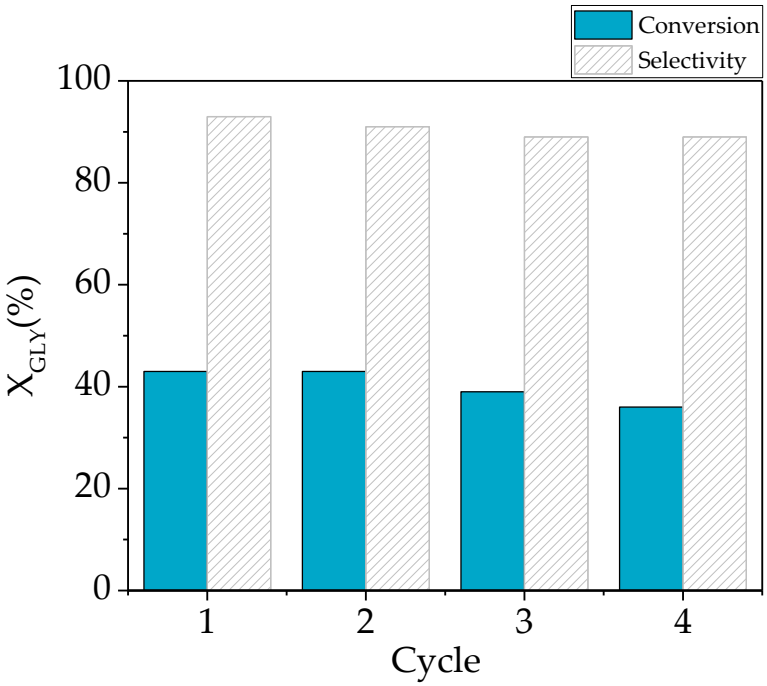

FIGURE 4.8: Recycling tests using Ga-74

TABLE 4.3: Textural properties and composition of Ga-74 catalyst before and after the 4th catalytic cycle

Material	**S_{BET}** ($m^2\,g^{-1}$)	**PD** (nm)	**Si/Ga**
Ga-74	350	7.0	79
Ga-74-4th cycle	335	6.8	76

S_{BET}: specific surface area; PD: pore diameter; Si/Ga determined by ICP-OES analysis

In order to investigate the stability of the active sites under the selected reaction conditions, a hot filtration test was performed as well (Figure 4.10, see

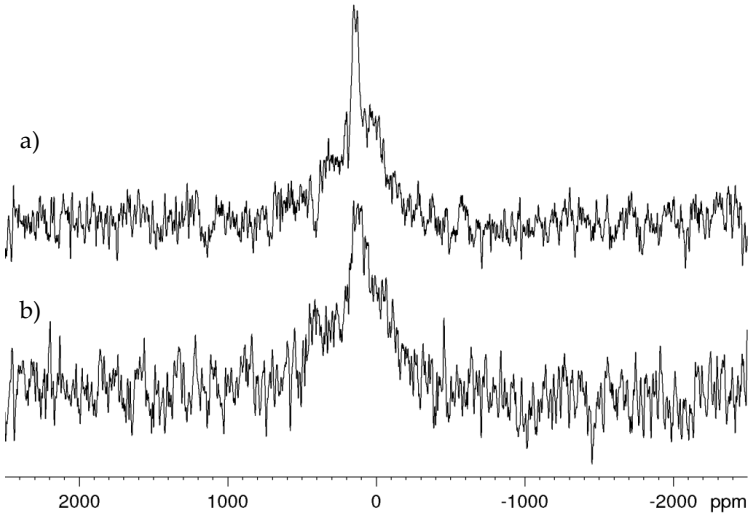

FIGURE 4.9: ^{71}Ga solid state MAS NMR spectra of fresh Ga-74 catalyst (a) and used Ga-74 after the 4th catalytic cycle

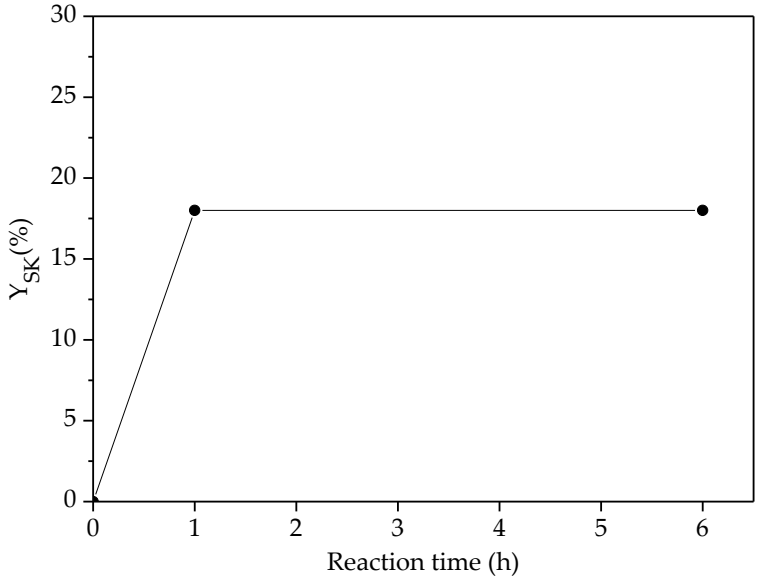

FIGURE 4.10: Hot filtration test with Ga-74. Reaction conditions: 25mg of catalyst, glycerol (0.92 g, 0.01 mol), absolute EtOH (0.70 mL) acetone (2.32 g, 4 equiv.). After 1 h, the catalyst was separated from the reaction mixture by hot filtration (50 °C) (see experimental part).

experimental section for reaction conditions). The solketal yield was quantified after one hour of reaction. The catalyst was then separated from the reaction medium by hot filtration (50°C) and the filtrate was further reacted at 50°C for additional five hours. Figure 4.10 shows that the solketal yield remained unchanged, indicating the absence of leaching of active sites.

4.3 Conclusions

The aerosol process has been used here for the first time as a straightforward synthetic procedure for the synthesis of Ga-silicate catalysts. The solids were fully characterized via transmission electron microscopy, ICP-OES analysis, and N_2 physisorption measurements. The catalysts can be described as spherical gallosilicate particles with well-calibrated mesopores, synthesized with an excellent control on the composition. An advanced XPS analysis using the Wagner plot and ^{71}Ga solid state MAS NMR spectroscopy allowed to deeply investigate the coordination environment of Ga. Importantly, this allowed to evidence the successful isomorphic substitution of Ga in the silica matrix. The best material, Ga-74, exhibited outstanding catalytic activity in the direct conversion of glycerol to solketal under solventless conditions. This material clearly outcompetes previously reported Ga-based catalysts. This high performance was ascribed to the efficient insertion of gallium as single site within the silica framework. Moreover, the catalyst proved to be stable under the selected reaction conditions and reusable in multiple runs. The stability of the catalyst was also supported via full characterization of the solid after the 4th cycle where no major differences were found.

Chapter 5

Reusable Surface-Functionalized Mesoporous Gallosilicate Catalysts for the Sustainable Upgrading of Glycerol

Abstract

Two series of functionalized mesoporous Ga-silicates prepared using different alkyl-silanes were synthesized in a straightforward and sustainable one-pot procedure. The efficacy of the adopted co-synthetic approach has been proved by ^{29}Si solid-state NMR experiments revealing a degree of functionalization close to the theoretical value. The successful incorporation of isolated Ga as single site within the silica framework was confirmed via ^{71}Ga solid state magic-angle-spinning NMR measurements. These materials were tested as catalysts in the synthesis of solketal from glycerol at low temperature and under solventless conditions. A systematic study evidenced the importance of a careful tuning of surface polarity, achievable with surface functionalization as well as with different thermal treatments. The methyl-functionalized solids displayed enhanced performances compared to the non-functionalized analogues, highlighting a strong beneficial role of surface hydrophobicity. The best functionalized catalysts proved to be easily reusable for multiple catalytic runs.

5.1 Experimental section

Preparation of the solids

Functionalized Ga-silicates, Ga-P-x-Me and Ga-F-x-Me (where P or F indicates the employed templating agent: P123 or F127 respectively and x indicates the nominal percentage of functionalization) were synthesized from a mixture of two silica sources, tetraethyl orthosilicate (TEOS) and methyltriethoxysilane (MTES). The quantity of MTES was adjusted to achieve three degrees of functionalization: 5, 10 and 15 mol%. A 5%mol functionalization was selected for the preparation of Ga-P (or F)-5-Pr and Ga-P (or F)-5-Ph (where 5 indicates the percentage of functionalization, Pr or Ph indicates the presence of propyl or phenyl moieties respectively). N-Propyltriethoxysilane (PrTES) was used for the synthesis of propyl functionalized solids and phenyltriethoxysilane (PhTES) for phenyl functionalized solids. For all the solids, solution 1 was prepared by hydrolyzing TEOS and MTES (PrTES or PhTES) in an aqueous solution of HCl 0.02 M (20 g). Pluronic P123 or F127 (3.9 g) was dissolved in absolute ethanol (45 g) and aqueous solution of HCl 0.02 M (8 g) to yield solution 2. Solutions 1 and 2 were left stirring during 15 hours and 40 minutes at room temperature, respectively. Then, the gallium precursor $(Ga((NO)_3)_3)\cdot 8H_2O$ was added to solution 1 in order to have a Si/Ga molar ratio equal to 74 (the amount of Ga in the metal precursor was determined by ICP-OES). Solutions 1 and 2 were mixed together and then stirred for 30 minutes. The clear solution obtained was atomized with a 6-Jet 9306A atomizer from TSI and the aerosol was dried by passing through a tubular quartz tube heated at 350 °C. The dried powders were collected on a cellulose nitrate filter, dried at 80 °C for one night and calcined under static air at 250 °C for 8 hours (heating rate of 1 °C/min).

5.2 Results and discussion

Two series of Ga-silicates functionalized using three different alkyl-silanes: methyl, propyl and phenyltriethoxysilane were synthesized using the aerosol-assisted sol-gel process in a co-synthetic approach selecting a Si/Ga atomic ratio of 74. In addition, two structure-directing agents from the Pluronic family (F127 and P123) were selected in order to study their impact on the morphological properties of the materials. Initially, Ga-based solids with three degrees of

methylation: 5, 10 and 15%mol were synthesized. The materials were denoted as Ga-P-x-Me and Ga-F-x-Me (where **P** or **F** indicates the employed templating agent: P123 or F127 respectively and x indicates the nominal percentage of functionalization). In order to investigate the effect of different alkyl moieties on the textural and surface properties of the solids, four additional functionalized materials were synthesized using propyl and phenyltriethoxysilane. A 5%mol functionalization was selected and the materials were denoted as Ga-P (or F)-5-Pr and Ga-P (or F)-5-Ph (where 5 indicates the percentage of functionalization, Pr or Ph indicates the presence of propyl or phenyl moieties respectively). All the above-mentioned functionalized Ga-silicates were then compared to their non-functionalized analogues synthesized under the same conditions, respectively named Ga-P-0 and Ga-F-0. After the synthesis, before the removal of the templating agent, all the as-synthesized materials were first analyzed by quantitative direct excitation (DE) solid state ^{29}Si MAS (magic-angle-spinning) NMR, revealing a functionalization degree always close to the nominal value for all the solids (see Table 5.1).

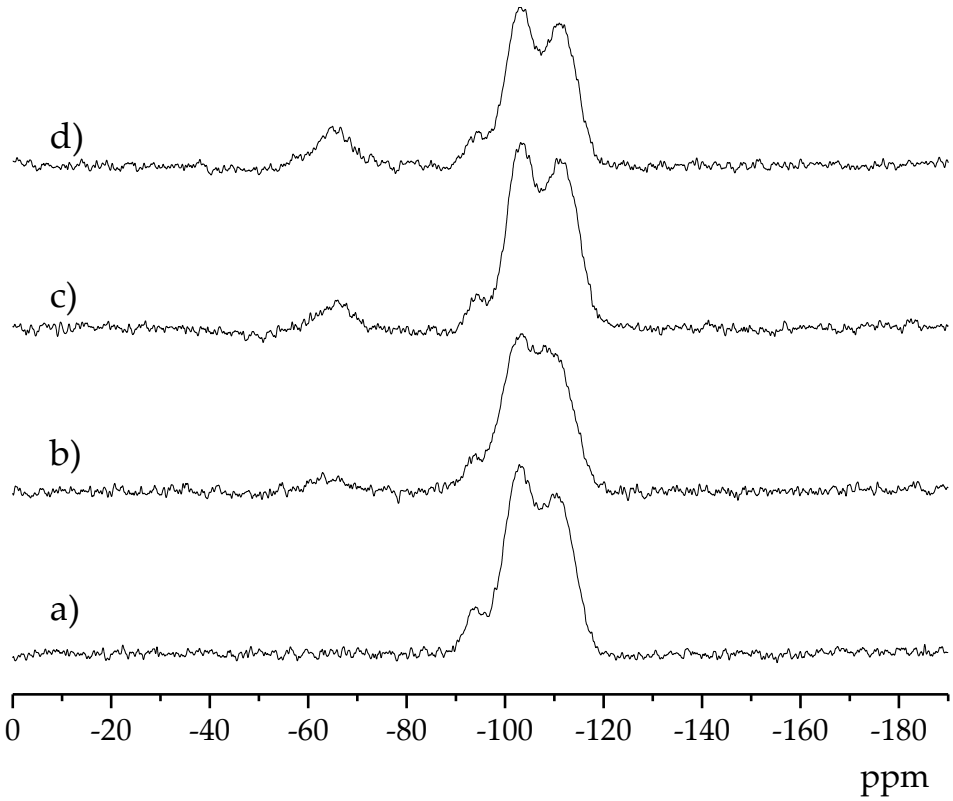

FIGURE 5.1: Solid-state ^{29}Si DE-MAS NMR spectra of (a) Ga-P-0 (b) Ga-P-5-Me (c) Ga-P-10-Me (d) Ga-P-15-Me after calcination at 250°C for 8h

It must be mentioned that the reproducibility of the synthesis is strongly related to the careful control of all the synthesis parameters (e.g. temperature, pre-hydrolysis time of the precursors, working parameters of the aerosol setup, etc.). To release the materials porosity the templating agent has to be removed, while preserving the organic-functionalization. Several procedures have been reported in literature for the removal of Pluronic from silica-based porous solids, including solvent extraction or calcination. However, taking inspiration from one of our previous work, a mild calcination treatment was here selected[203]. The best compromise between a complete removal of the surfactant and only a minor loss of the functionalization was achieved with a thermal treatment at 250 °C for 8h. This mild thermal treatment was successfully applicable to both P123 and F127 templating agents. Thus, all the solids were calcined at the selected temperature and as proved by ^{29}Si solid state MAS NMR experiments, the initial amount of organic moieties was largely preserved in all materials. Figure 5.1 shows an example of quantitative^{29}Si DE-MAS spectra of the methyl-functionalized P123 templated series. The corresponding spectra of Ga-P-5-Pr, Ga-P-5-Ph and the F127 templated solids can be found in Appendix (Figure A.11 to A.14).

The characteristic contributions proper to an amorphous silica matrix can be observed. Clear Q^4 [$(SiO)_4Si$] (around -111 ppm), Q^3 [$(SiO)_3SiOH$] (around

TABLE 5.1: Textural properties and composition of Ga-silicate solids

Material	**S_{BET}** ($m^2\,g^{-1}$)	**PD** (nm)	**PV** ($cm^3\,g^{-1}$)	**% Funct.** (after calc.)	**Ga** ($mmol\,g^{-1}$)
Ga-P-0	443	7.8	0.6	-	2.0
Ga-P-5-Me	405	7.1	0.6	4	1.9
Ga-P-10-Me	428	7.3	0.5	8	1.8
Ga-P-15-Me	477	6.6	0.5	13	1.8
Ga-P-5-Pr	500	7.0	0.6	<3	1.8
Ga-P-5-Ph	461	6.6	0.5	<3	2.0
Ga-F-0	546	7.8	0.5	-	2.1
Ga-F-5-Me	502	7.5	0.4	3	1.8
Ga-F-10-Me	457	6.9	0.4	8	1.9
Ga-F-15-Me	494	6.8	0.4	14	1.9
Ga-F-5-Pr	553	7.1	0.5	<3	2.0
Ga-F-5-Ph	477	6.3	0.4	<3	2.0

S_{BET}: specific surface area; PD: pore diameter; PV: pore volume; amount of Ga determined by ICP-OES analysis

-102 ppm) and Q^2 [$(SiO)_2Si(OH)_2$] (around -92 ppm) signals can be found in all samples. The ^{29}Si spectra of methyl-functionalized solids display two peaks at -66 and -59 ppm, assigned respectively to $RSi(OSi)_3$ (T^3) and $R(HO)Si(OSi)_2$ (T^2) species[203]. These signals can be found as well in the whole series of functionalized solids (see Appendix A10-A13) and they attest the successful functionalization of the surface. The Ga loading was quantified by inductively coupled plasma optical emission spectroscopy (ICP-OES). The experimental composition – expressed in mmol g^{-1} of Ga – was very close to the nominal composition (where Si/Ga=74 corresponds to 2 mmol g^{-1} of Ga) for all the solids (see Table 5.1). The generation of active acid sites, fundamental for the application of these solids as catalysts, is strictly related to the insertion of Ga as single site in the structure able to generate the right balance of Brønsted and Lewis acid sites[11]. The coordination environment of gallium was analyzed selecting solid state ^{71}Ga NMR spectroscopy. Due to the low wt% of gallium, replacing silicon in an amorphous environment, the investigations were performed under magic-angle-spinning (MAS) at 25 kHz, using high magnetic field (11.7 T).

Here we report only the ^{71}Ga NMR characterization of the methylated P123 series of materials (Figure 5.2). Figure 5.2 shows the MAS NMR spectra of Ga-P-0, Ga-P-5-Me, Ga-P-10-Me, Ga-P-15-Me. A sharp peak at +140 ppm, observed for all the materials, is ascribed to tetrahedral framework gallium and is the evidence of the incorporation of mainly single-site Ga in the silica framework. This contribution has already been observed for other gallo-silicate solids already reported in literature[199, 200]. The presence of an additional weak contribution at 0 ppm can be assigned to the presence of low amounts of octahedral extra-framework Ga (see Figure 4.4 for a comparison with a pure Ga_2O_3 sample). These extra-framework species are expected to have an octahedral environment and have been already reported to be catalytically inactive[11]. Similar results were obtained analyzing the environment of Ga in the case of the F127 templated solids and an example can be found in Figure A.19.

The samples morphology was investigated starting by transmission electron microscopy (TEM). All solids displayed a spherical shape with a mesoporous structure and a pores size distribution between 6 and 7 nm, typical of solids synthesized using the aerosol assisted process[13, 203]. When F127 was used as a surfactant, a rather regular cubic mesostructure was obtained with an estimated pore diameter of 7 nm, even when the organic-functionalization was raised to 15% (see Figure 5.3e to 5.3h). Interestingly, the materials synthesized

in the presence of P123 display a slight deformation of the cubic mesostructure in the periphery of the particles (see Figure 5.3a to 5.3d). This deformation was more evident with the increasing amount of functionalization. Major modification of the structure with the appearance of some "onion like" organizations appeared raising the functionalization to 15%. Longer organic chains as in the case of propyl moieties or bulkier phenyl groups, did not provoke at low functionalization degrees a substantial deformation of the structure (see Figure A.15).

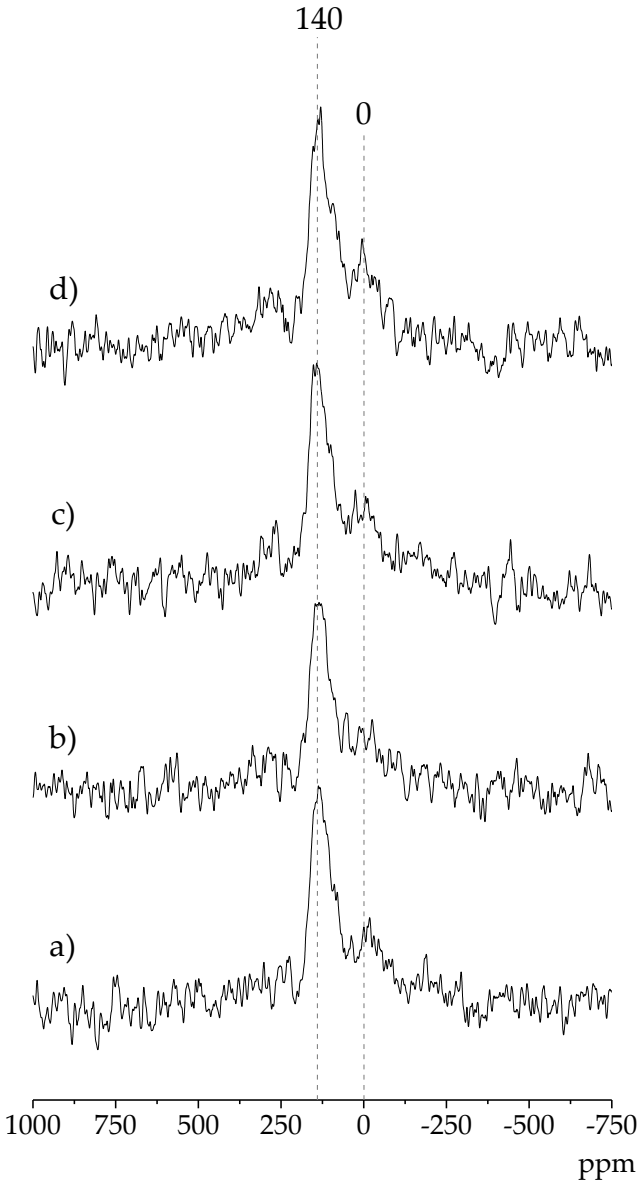

FIGURE 5.2: Solid-state ^{71}Ga MAS NMR spectra of (a) Ga-P-0 (b) Ga-P-5-Me (c) Ga-P-10-Me (d) Ga-P-15-Me after calcination at 250 °C for 8h

This behavior was previously observed and it has been ascribed to the different balance among the hydrophilic and hydrophobic parts of the two triblock polymers. The lower amount of hydrophilic units in the P123 may be responsible of an increased affinity with the hydrophobic methyl groups of

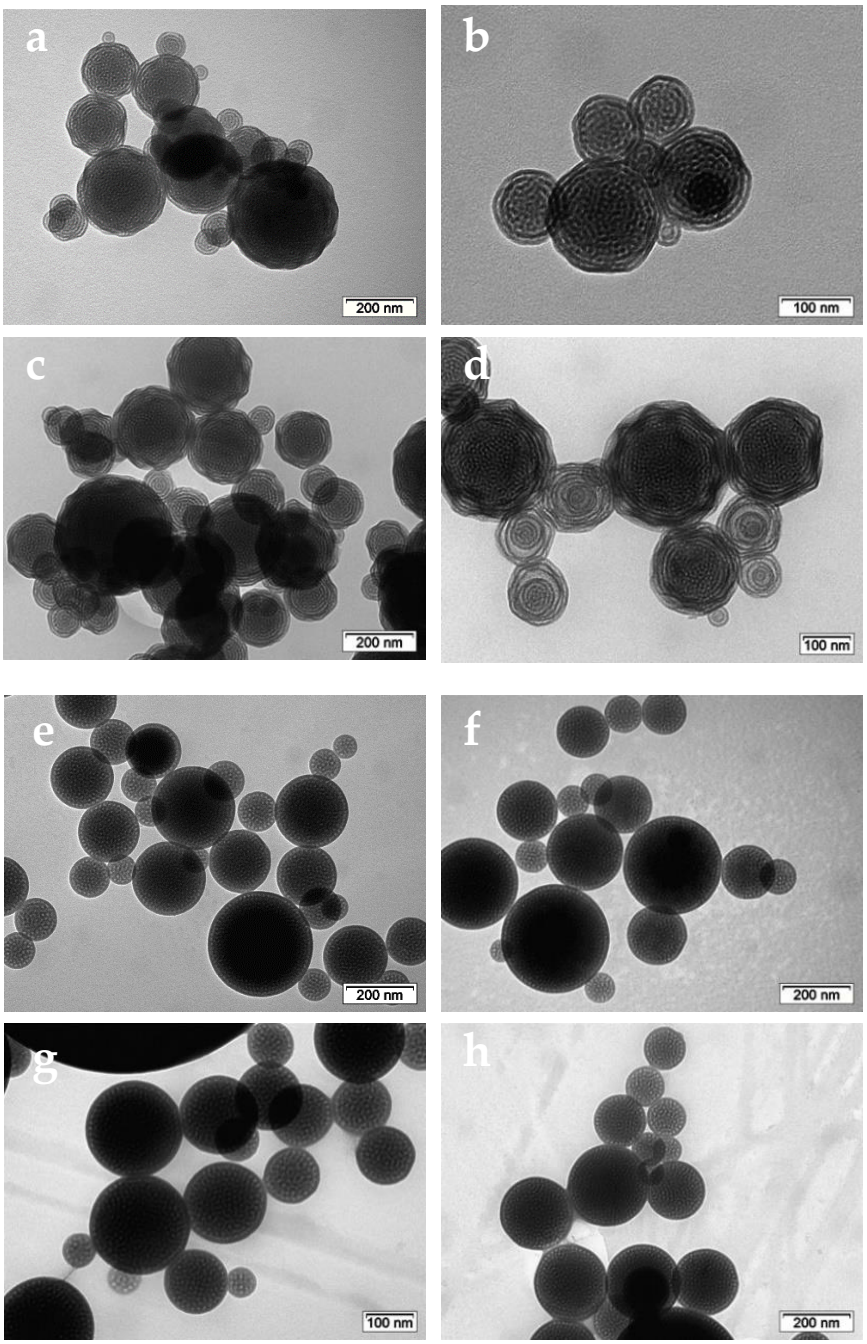

FIGURE 5.3: TEM micrographics of (a) Ga-P-0 (b) Ga-P-5-Me (c) Ga-P-10-Me (d) Ga-P-15-Me and of (e) Ga-F-0 (f) Ga-F-5-Me (g) Ga-F-10-Me (h) Ga-F-15-Me

the MTES which could be oriented toward the hydrophobic shell of the micelles causing a structural deformation of the final solid. The low angle powder XRD patterns of Ga-silicates templated with P123 (Figure A.16) featured mainly first order d_{100} diffraction peaks (with a d-spacing of 9 nm) typical of ordered mesostructured silicates assembled using a non-ionic surfactant, forming P6m hexagonal arrays of mesopores. Particles templated with F127 show one diffraction peak (d_{110} = 11.2 nm) consistent with a face-centered-cubic (FCC) structure (see Figure A.18). For both series, N_2 physisorption measurements showed a type-IV isotherm characterized by a considerable hysteresis loop. P123 templated solids present a H1 hysteresis loops with steeper branches, typical of mesoporous materials with one type of mesopores (Figure 5.4 and A.17).

The pore size distribution was narrow, with a mean pore diameter of 7 nm. F127 templated materials exhibit a H2 hysteresis loop characteristic of cage-type mesopores with a mean pore diameter of 7 nm (Figure 5.4 and A.18). An overview of the textural properties of the two series of functionalized Ga-silicates is reported in Table 5.1. The target reaction selected in this work is represented by the acetalization of glycerol with acetone to produce solketal. The effective insertion of single-site tetrahedral gallium, proved by solid-state ^{71}Ga NMR, should give rise to the desired acidic properties essential in promoting the upgrade of glycerol into solketal. In Table 5.2 the catalytic performances of the whole set of solids are presented. Considering as a key aspect the sustainability of the process, the tests were carried out under solvent free

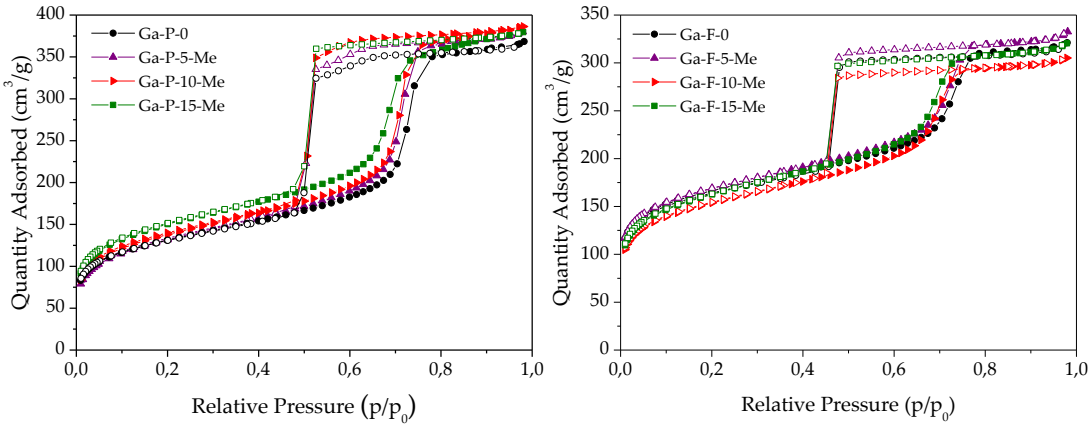

FIGURE 5.4: Nitrogen adsorption/desorption isotherms of Ga-P-0, Ga-P-5-Me, Ga-P-10-Me and Ga-P-15-Me (left) and Ga-F-0, Ga-F-5-Me, Ga-F-10-Me and Ga-F-15-Me (right) after calcination at 250°C for 8h

TABLE 5.2: Catalytic activity of Ga-silicates in the conversion of glycerol to solketal

Entry	Material	$Yield_{SK}$ (%)	$Sel._{SK}$ (%)	TOF	TON
1	**Ga-P-0**	22	84	532	1063
2	**Ga-P-5-Me**	25	85	663	1326
3	**Ga-P-10-Me**	18	82	506	1012
4	**Ga-P-15-Me**	18	82	500	1000
5	**Ga-P-5-Pr**	17	83	462	923
6	**Ga-P-5-Ph**	13	79	328	656
7	**Ga-F-0**	10	81	242	484
8	**Ga-F-5-Me**	16	83	434	867
9	**Ga-F-10-Me**	12	82	311	622
10	**Ga-F-15-Me**	9	79	240	479
11	**Ga-F-5-Pr**	10	80	243	485
12	**Ga-F-5-Ph**	9	77	224	447

Reaction conditions: 10 mg of catalyst, 0.01 mol of glycerol, 0.04 mol of acetone, 50 °C, 2h; TOF = $(n_{solketal}/n_{Ga})h^{-1}$; TON =$(n_{solketal}/n_{Ga})$.

conditions at 50 °C, selecting a reaction time of 2h. To verify the reproducibility of the catalytic results, the materials were tested three times under the same reaction conditions. The associated error calculated was around 2%, proving the reproducibility of the tests.

The comparison between functionalized and non-functionalized analogous, synthesized under the same conditions (compare entries 1 and 7 with 2 and 8 in table 5.2), revealed that the 5% methylated solids Ga-P-5-Me and Ga-F-5-Me present the best catalytic activity in terms of TON, even when the activity is normalized to the BET specific surface area (see Figure A.20). From this comparison emerged a positive influence of the methylation on the performances of the catalysts. It is important to underline that even a very low degree of methylation was apparently enough to enhance the catalytic activity of the solids. It appears that the observed enhancements in terms of TON could be explained by reactivity differences arising from the functionalization of the surface instead of different environments of the catalytic sites, supporting the beneficial role of the hydrophilic/hydrophobic tuning of the surface properties. The slightly more hydrophobic surface may locally shift the equilibrium to the formation of solketal, helping the removal of formed water from the active sites. No further improvement in the catalyst performance was observed

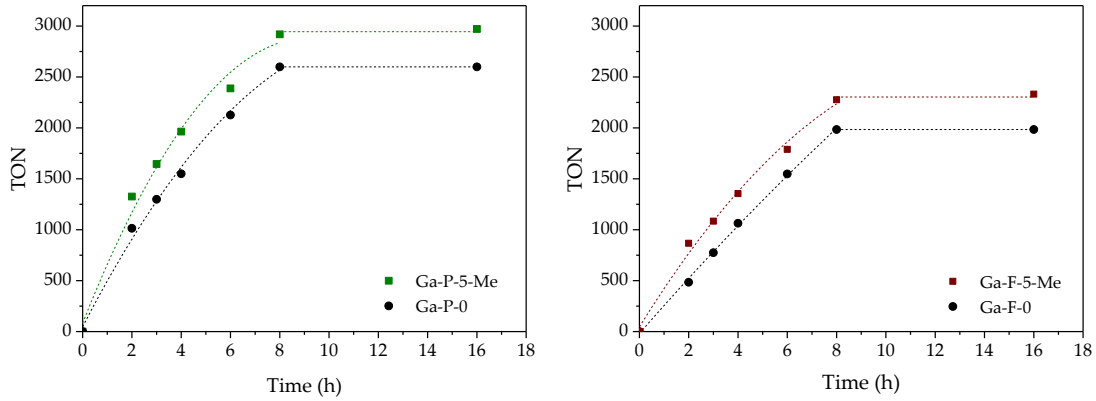

FIGURE 5.5: Evaluation of the catalytic activity over time. Comparison between Ga-P-5-Me and Ga-P-0 (left), Ga-F-5-Me and Ga-F-0 (right)

when the methylation degree is brought to 10% (Entries 3 and 9). An even higher content of methyl groups (15%) in the formulation or the presence of bulkier functional groups (see entries 5, 6 and 10, 12) leads to a lowering of the activity. The presence of a too high concentration or too bulky hydrophobic moieties could have a detrimental effect, hindering the adsorption of glycerol in proximity of the active sites. Surprisingly the solids synthesized employing P123 as surfactant display better catalytic performances than the corresponding materials of the F127 series. However, the insertion of Ga as single site is very similar on both series of solids and no important difference can be observed comparing the other textural parameters. The only important difference is the presence of a "onion-like" organization in the case of P123. This difference was previously ascribed to a better affinity of the methyl moieties with the more hydrophobic P123 surfactant. This affinity could be responsible of a more homogenous distribution of methyl groups on the internal and external surface of the solid. Therefore, this may result in a lower percentage of non-accessible groups that remain trapped in the walls. This hypothesis could be confirmed via H_2O adsorption/desorption measurements which are programmed in the next future. Moreover, NH_3 TPD analysis of the solids will be performed as well in order to obtain more insights on the acidity of the samples.

The catalytic activity of the best materials was also evaluated over time (in terms of TON, defined as moles of solketal produced per mole of Ga). Regardless of the catalyst considered, the TON increased rapidly during the first 8h of reaction followed by a plateau, suggesting that the reaction is approaching

equilibrium. In addition, regardless of the reaction time selected, the functionalized materials have a higher TON compared to non-functionalized materials (see Figure 5.5). This difference is more pronounced at short reaction times, confirming that 2h was the best compromise between an adequate solketal yield allowing an accurate quantification and a meaningful comparison among the catalysts far enough from the equilibrium conversion.

In the perspective of sustainable processes promoted by heterogeneous catalysts, a key role is played by the stability of the catalyst under the selected reaction conditions, which determines the possibility to reuse it in multiple catalytic runs. The reusability of Ga-P-5-P123, presenting the most promising performances, was investigated in consecutive runs (Figure 5.6). After each cycle the catalyst was separated via filtration from the reaction mixture, washed and thermally regenerated. The calcination treatment is of fundamental importance since it was already reported that the activity gradually decreases upon reuse if the catalyst is only washed with the reaction solvent. From this study emerged that the good activity and selectivity of the catalyst was preserved at least for four catalytic cycles, proving the robustness and the truly heterogeneous nature of the catalyst.

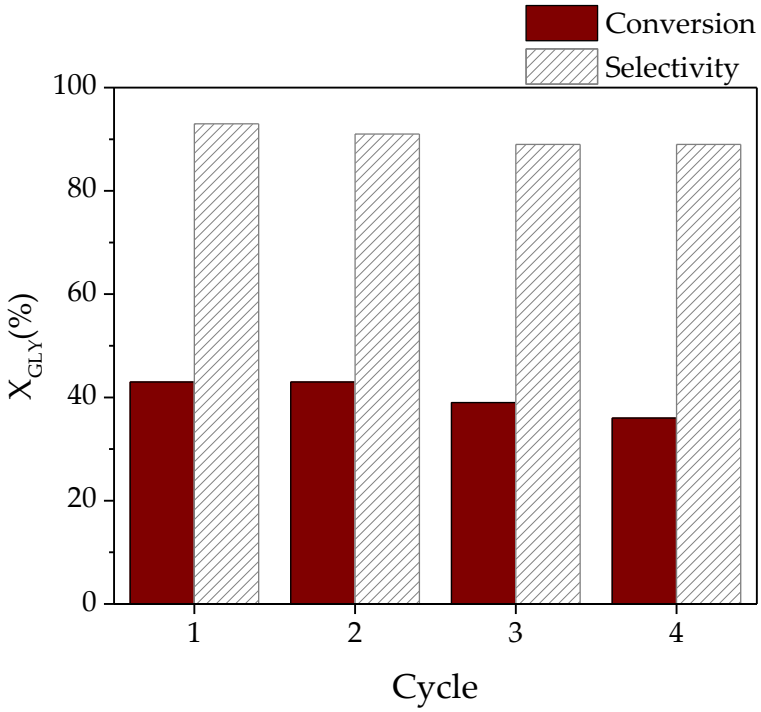

FIGURE 5.6: Recycling tests using Ga-P-5-Me

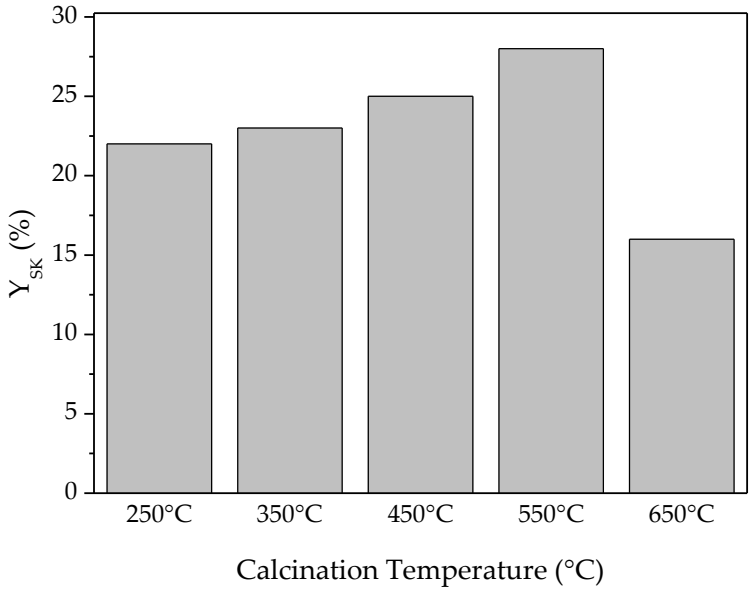

FIGURE 5.7: Study of the influence of the calcination temperature on the catalytic activity of Ga-P-0

As mentioned at the very beginning of this work, the importance of preserving the organic functionalities on the surface of the solids while removing efficiently the structuring agent, determined the adoption of a mild thermal treatment at 250 °C. However, in the literature, analogous non-functionalized metal-silicates are usually subjected directly to a thermal treatment ranging from 500 °C to 600 °C to effectively remove the templating agent[11, 204, 205].

It is relevant to highlight that the calcination temperature may affect also the physicochemical properties of the materials such as specific surface area and surface hydroxyl content, responsible of the hydrophilic character of the surface. For this reason, we selected to investigate the catalytic behavior of Ga-P-0 at different calcination temperatures. As reported in Figure 5.7, the increase of the calcination temperature from 250 °C to 550 °C had a beneficial impact on the catalytic performance of the non-functionalized solid. Considering the physico-chemical properties of the material after calcination at 550 °C, no major differences were observed in terms of BET specific surface area or pore size distribution (see characterization of the analogous Ga-74, in Chapter 3).

Therefore, these observations may suggest the beneficial role played by the temperature on the modification of the surface polarity. The surface of silica is dehydrated as the temperature of the thermal treatment increases with the removal of the adsorbed water and thermal dehydration reaction, where two

neighboring silanols condense into a siloxane bridge. The experimental results reported in the literature demonstrated that increasing the temperature of the thermal treatment the silica surface becomes hydrophobic due to the condensation of surface hydroxyls and the formation of siloxane bridges[206–208]. The reduction of the hydroxyl groups population, was here proved by the higher degree of condensation estimated by quantitative direct excitation ^{29}Si MAS NMR visible in Figure 5.8. This could be an interesting route to modify the hydrophilic/hydrophobic balance of the surface proving again its beneficial role in particular on the selected reaction.

Finally, raising the calcination temperature to 650 °C resulted in a rather remarkable loss of catalytic activity that in this case could be ascribed to a major loss of specific surface area (around 200 $m^2\,g^{-1}$). The results of this work can be seen as two parallel paths, both leading to the improvement of catalyst performance around the same final concept of hydrophilic hydrophobic tuning of the surface. In this work we proved that not only a straightforward functionalization of the surface may be used to introduce a partial hydrophobic character at the surface of silica-based solids but also the proper calcination temperature may allow to control the population of surface silanols. Considering the quite similar catalytic performances of the best catalysts, we may anyway point out that the functionalized solids can be obtained using the same straightforward one-pot synthetic procedure used for the non-functionalized solids but present the advantage of a less energy-consuming thermal treatment at mild temperature. For these reasons they may be considered the best option, balancing sustainability and performances.

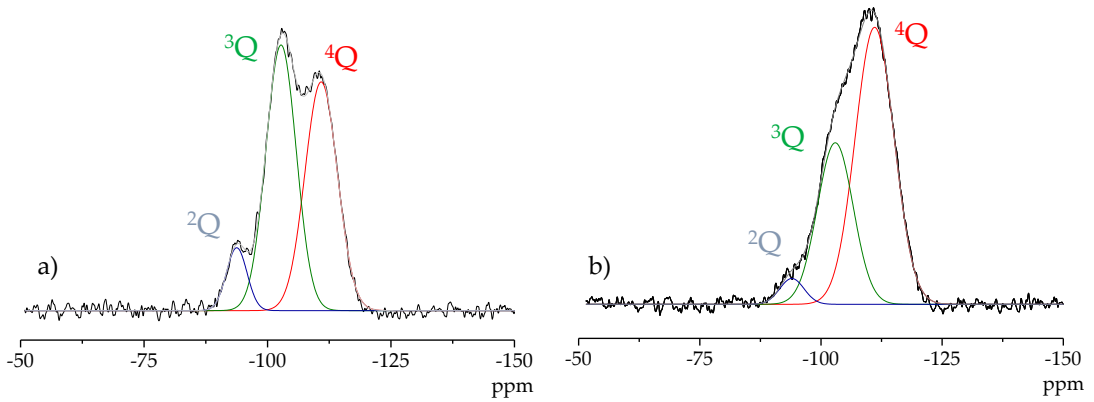

FIGURE 5.8: ^{29}Si direct excitation MAS NMR spectra of Ga-P-0 calcined at 250 °C (top) and 550 °C (bottom)

5.3 Conclusion

The synthesis of a series of functionalized Ga-silicates was achieved using the aerosol process demonstrating the versatility of this synthesis technique for the one pot preparation of functionalized solids. The efficient incorporation of isolated Ga as single site within the silica framework was confirmed via ^{71}Ga solid state NMR and the stability of the organic moieties has been assessed using ^{29}Si solid-state MAS NMR. All the materials were tested in the acetalization of glycerol with acetone to yield solketal and in particular the materials synthesized using P123 as templating agent demonstrated the best catalytic activity. A positive influence of the functionalization emerged, especially in presence of methyl moieties. The methylation proved to have a beneficial effect on the performances of all the catalysts in terms of both activity and selectivity compared to the non-methylated solid. Furthermore, it was observed that a very low degree of methylation was effective to enhance the catalytic performance of the materials shifting locally the equilibrium to the production of solketal. Moreover, the best catalyst was successfully used in multiple catalytic cycles thus proving its stability under the selected reaction conditions. Moreover, a systematic study evidenced the importance of a careful tuning of surface polarity, achievable not only with surface functionalization but also with different thermal treatments applied to non-functionalized solids. The control of the hydroxyl groups population on the surface, possible with a control on the calcination temperature, allowed to obtain as well a high catalytic activity.

General Conclusion and Future Work

General conclusion

Across this work we presented the ambitious challenge that stays in the connection between the development of novel metal-substituted porous silicates catalysts and the growing interest in the application of these solids in the valorization of a new generation of feedstock coming from renewable resources and biomasses.

For this purpose, sol-gel chemistry demonstrated to be a powerful tool providing a wide range of parameters that can be tuned to obtain tailored structural and textural features. The exploration of new routes allowed the design of robust and active catalysts for these applications always considering sustainability parameters.

A novel silica based solid displaying a 1D tubular structure, bearing Sn inserted as single site in the framework was successfully prepared for the first time allowing to explore the aspect of the influence of the catalyst morphology and porosity on its catalytic activity. The incorporation of isolated Sn sites in this particular morphology, obtained using a relatively straightforward synthesis protocol in the absence of additional thermal treatments, was never reported before. The optimized material, presenting a proper balance of Brønsted and Lewis acid sites and enhanced accessibility, exhibited outstanding catalytic activity in particular in the direct conversion of glycerol to solketal. The high catalytic performance of the solid allowed decreasing the reaction temperature to 25 °C maintaining good results in terms of solketal yield. This behavior was ascribed to the single-site insertion of tin within silica framework as well as to the high acidity of the Sn-NTs as proved by FT-IR measurements

of ammonia adsorption. The catalyst proved to maintain its stability and conserve its morphology even after multiples catalytic runs.

The insertion of Sn in the silica matrix to synthesize active and selective catalysts was approached as well presenting another original sol-gel synthetic route that allow to obtain unique morphologies and to control structural and textural properties. Novel mesoporous tin silicates were prepared via an easy, one-pot and continuous mode, using the aerosol-assisted sol-gel process. The synthesized solids, presenting different tin loading, presented high surface area, regular mesoporosity and a successful incorporation of isolated Sn within the silica framework, fundamental to obtain the correct combination of acid sites. These aerosol-made mesoporous Sn-silicates showed excellent catalytic performance in the conversion of dihydroxyacetone to ethyl lactate, reaching as well a very high selectivity. The best catalyst, obtained selecting a Si/Sn ratio of 74, displayed higher turnover number than the reference metal-silicates catalysts previously reported in literature. In addition, the adopted synthetic approach allowed to obtain a robust catalyst that did not leach and was successfully used in multiple catalytic cycles thus proving its stability under the selected reaction conditions. In the perspective of developing better heterogeneous catalysts, considering the second objective of this thesis, the deep understanding of the impact of the hydrophobic/hydrophilic balance on the catalytic activity was considered as well in the context of ethyl lactate production.

The aerosol-assisted sol-gel process was used for a selective tuning of the surface properties with the aim of optimizing the global efficiency of the catalysts. A series of Sn-silicates with different degrees of methylation was successfully synthesized using a co-synthetic approach. The process is characterized by a low waste generation and a more sustainable procedure for the effective removal of the surfactant was optimized using a mild calcination treatment. The organic functionalization was always conserved as proved by ^{29}Si and ^{13}C solid state NMR characterization. Methylated Sn-silicates were tested in the conversion of dihydroxyacetone to ethyl lactate and a positive influence of the methylation on the performances of all the catalysts in terms of both activity and selectivity compared to the non-methylated solid was proved. Even a 2% of methylation was effective to enhance the catalytic performance of the materials. The anchored methyl moieties demonstrated to be very stable not only after multiple catalytic cycle but also to mild thermal treatment used for the regeneration of the catalyst.

Inspired by the results obtained using the aerosol assisted sol-gel process for the insertion of Sn, we selected to investigate the insertion of Ga to continue our research. Despite the use of Ga hold a minor role at this time in biomass valorization, its insertion as single-site was expected to introduce a promising balance of Lewis and Brønsted acidity especially favorable for the acetalization of glycerol into solketal. The aerosol process was used for the first time for the synthesis of Ga-silicate catalysts with well-calibrated mesopores, synthesized with an excellent control on the composition. Since the understanding and the quantification of the different active species is of fundamental importance, allowing to strongly correlate the final properties of the solids with the metal coordination. To investigate the coordination number/geometry of Ga inserted as single site within the silica matrix, a deep structural investigation of the materials was performed via solid state NMR of ^{71}Ga under magic angle spinning (MAS) and advanced XPS analysis using the Wagner plot. The characterization study demonstrated that the best catalyst of the series was obtained selecting a Si/Ga ratio of 74, as the best compromise between amount of Ga and its efficient insertion as isolated active sites in the silica matrix. The best material, Ga-74, exhibited outstanding catalytic activity in the direct conversion of glycerol to solketal under solventless conditions at 50°C. This material presented higher activity compared not only to previously reported Ga-based catalysts but also to other metal silicates. The stability of the catalyst was also supported via full characterization of the solid after the 4th catalytic cycle.

To deal again with both the objectives of this thesis, the promising performances of Ga-silicates has been exploited with the aim of expanding the knowledge on the impact of the hydrophobic/hydrophilic balance of the catalyst surface, this time applied to the production of solketal. Two series of functionalized mesoporous Ga-silicates were prepared using different alkyl-silanes demonstrating again the versatility of this synthesis technique for the one pot preparation of functionalized solids. Isolated Ga as single site within the silica framework was efficiently incorporated and the stability of the organic moieties has been assessed using ^{29}Si solid state MAS (magic-angle-spinning) NMR. All the materials proved to be active in the acetalization of glycerol but in particular the materials synthesized using P123 as templating agent demonstrated the best catalytic activity. The screening of the catalytic performance showed a positive influence of the functionalization, especially in presence of methyl moieties. The methylation proved to have a beneficial effect on the

performances of all the catalysts in terms of both activity and selectivity compared to the non-methylated solid. This behavior, observed even in presence of a low methylation degree, was assigned to the shift of the local equilibrium to the production of solketal in presence of slightly more hydrophobic surface. Moreover, the best catalyst was successfully used in multiple catalytic cycles thus proving its stability under the selected reaction conditions. In addition, a systematic study evidenced the importance of a careful tuning of surface polarity, achievable not only with surface functionalization but also with different thermal treatments applied to non-functionalized solids. A proper calcination temperature may allow as well to control the population of surface silanols and hence the polarity of the surface. The results of this last chapter can be seen as two parallel paths, both leading to the improvement of catalyst performance around the same final concept of hydrophilic/hydrophobic tuning of the surface.

In summary, during this PhD project numerous catalytic systems for the synthesis of valuable chemicals from biomass derived feedstock were successfully developed. In addition, a systematic study was devoted to the deep understanding of the impact of the hydrophobic/hydrophilic balance on the catalytic activity. The control of surface polarity proved to be a powerful tool for the optimization of the global efficiency of the catalysts.

Future work

Future work following for the results presented in this thesis may consider the optimization of the synthesis procedure to obtain 1D tubular nanostructures exploring the insertion of other metals presenting potentially different combinations of Lewis and Brønsted acidity. On the one hand, based on the results presented in this work, Sn-silica nanotubes showed the best performances in the ethyl lactate production compared to the aerosol-made solids. On the other hand, the insertion of Ga appeared to be more promising for the production of solketal. For this reason, we may speculate that the synthesis of Ga-silica nanotubes should be studied to obtain even more active catalysts for the production of solketal. The application of this morphology may be even considered to design heterogeneous and recyclable catalysts for the direct conversion of glycerol into lactates and lactic acid. The ideal catalyst should present excellent activity and selectivity, controlling the oxidation and dehydration/rehydration

step required for this type or reactions.

The one-pot and continuous mode, using the aerosol-assisted sol-gel process, may be also exploited to incorporate different metals (i.e. Hf or Zr) and to develop new solids with different functionalities and highly homogeneous composition. New functionalities may be explored to develop better heterogeneous catalysts. One possible alternative to the use of methyl groups for the functionalization of the surface, may be the insertion fluorinated moieties or the direct fluorination of silica, taking advantage of the possible beneficial role of the hydrophobic/hydrophilic tuning of the catalyst surface. A better comprehension of the role played by surface polarity may be envisaged considering a deeper characterization (i.e. water adsorption measurements) for a direct evaluation of hydrophobicity/philicity. Special care may be taken also to discriminate between the effect of polarity of the samples from the textural effects.

Finally, a more ambitious goal from an applied point of view may be to synthesize catalysts able to work in presence of crude glycerol (less expensive than commercially available highly pure glycerol) whose water content is close to 20 wt%. This possibility is of great industrial interest because it will closely influence the economic viability of biofuels and impulse a new generation biomass-based industry.

Appendix

A.1 Chapter 2: High-yield synthesis of ethyl lactate with mesoporous SnSi mixed oxide catalysts prepared by the aerosol-assisted sol-gel process

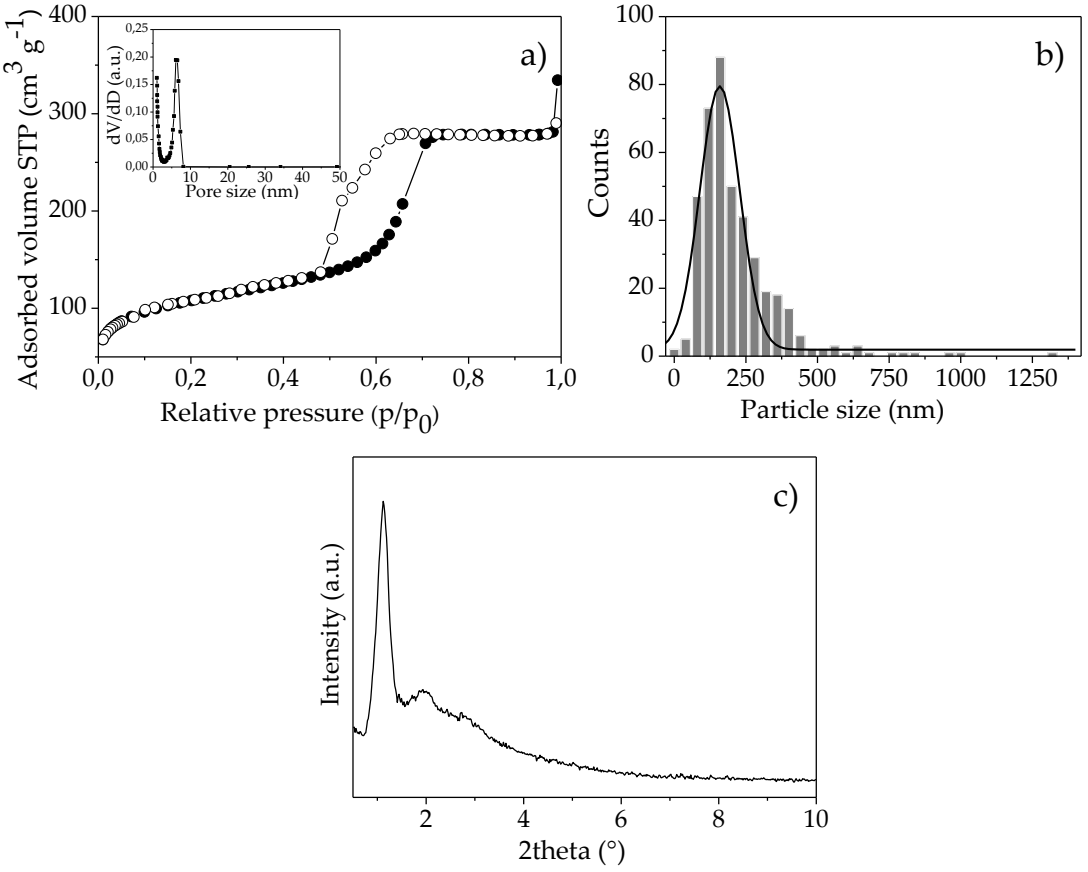

FIGURE A.1: Nitrogen adsorption/desorption isotherms and corresponding pore size distribution (insert) (a), Particle size distribution (b) and Small-angle XRD pattern of SnSi-37 catalyst (c)

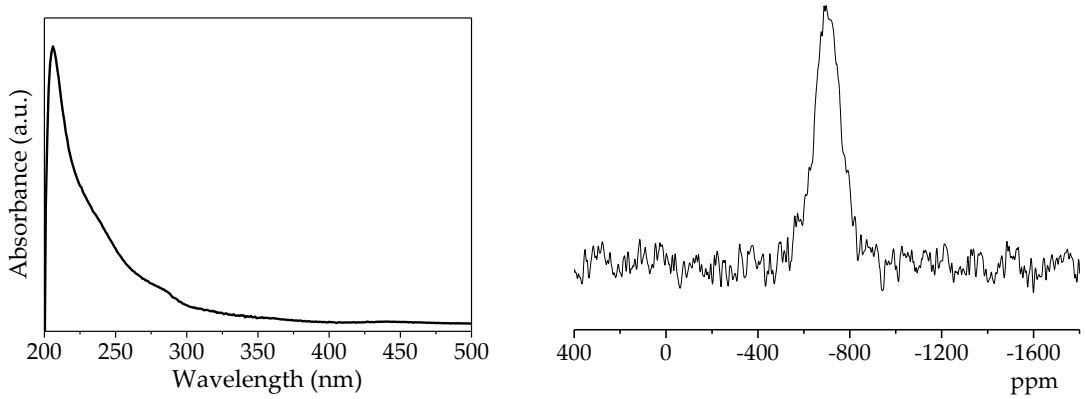

FIGURE A.2: Diffuse reflectance UV–Vis spectrum (left) and solid state ^{119}Sn static NMR spectrum (right) of SnSi-37 catalyst

A.2 Chapter 3: Mesoporous methyl-functionalized Sn-silicates generated by the aerosol process for the sustainable production of ethyl lactate

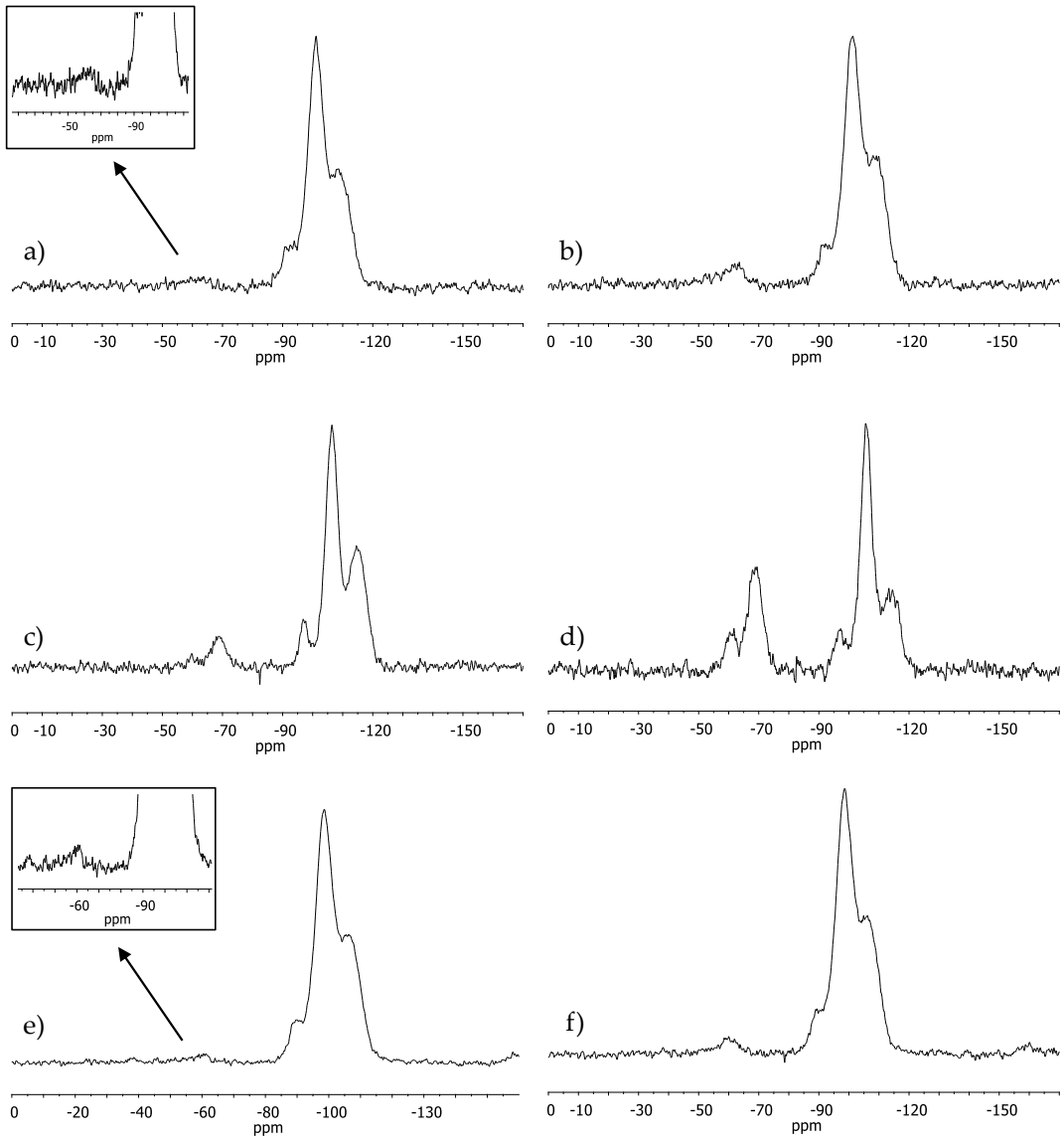

FIGURE A.3: Solid state ^{29}Si MAS NMR spectra (direct excitation experiments) of as-synthesized (not calcined) methylated Sn-x-F127 and Sn-x-P123. Sn-2-F127 (a), Sn-5-F127 (b), Sn-10-F127 (c), Sn-30-F127 (d), Sn-2-P123 (e) and Sn-5-P123 (f)

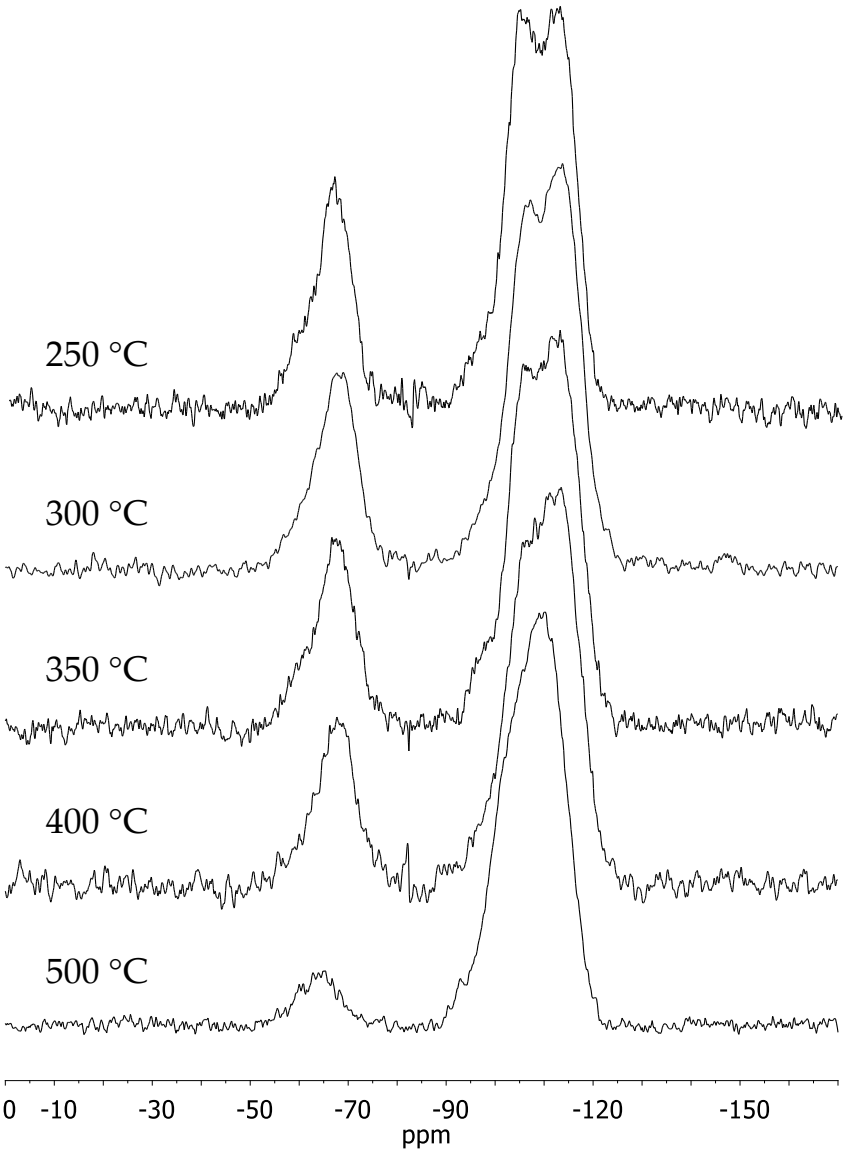

FIGURE A.4: Solid state ^{29}Si MAS NMR spectra (direct excitation experiments) of Sn-30-F127 calcined at different temperatures.

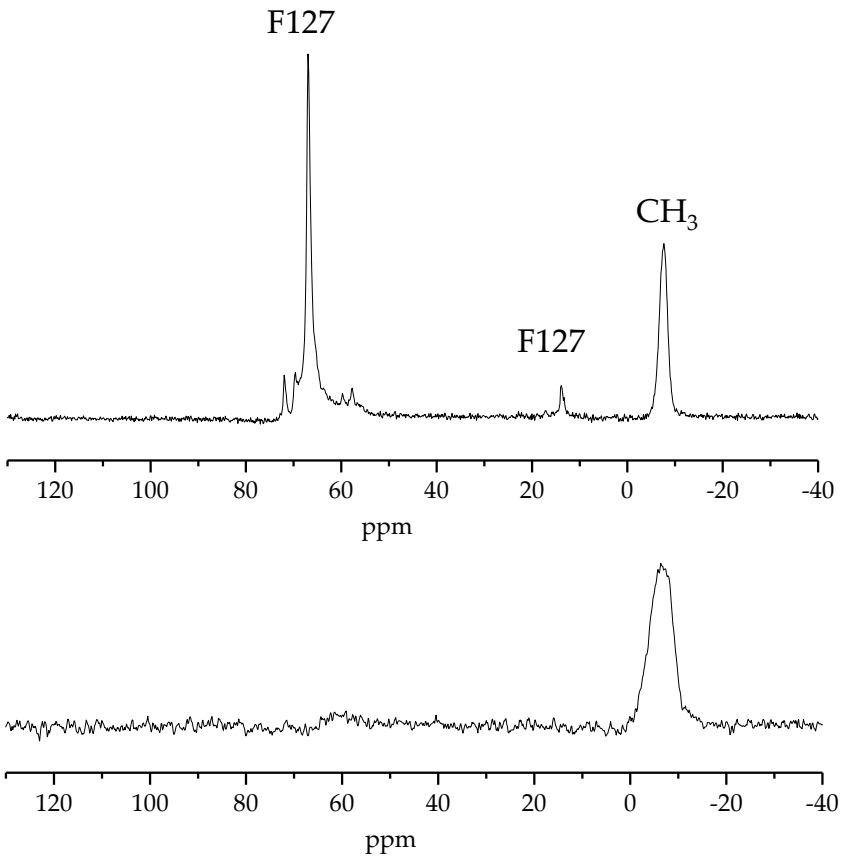

FIGURE A.5: Solid state ^{13}C MAS NMR spectra (cross polarization experiments) of as synthesized Sn-30-F127 (top) and after calcination at 250 °C (8h)

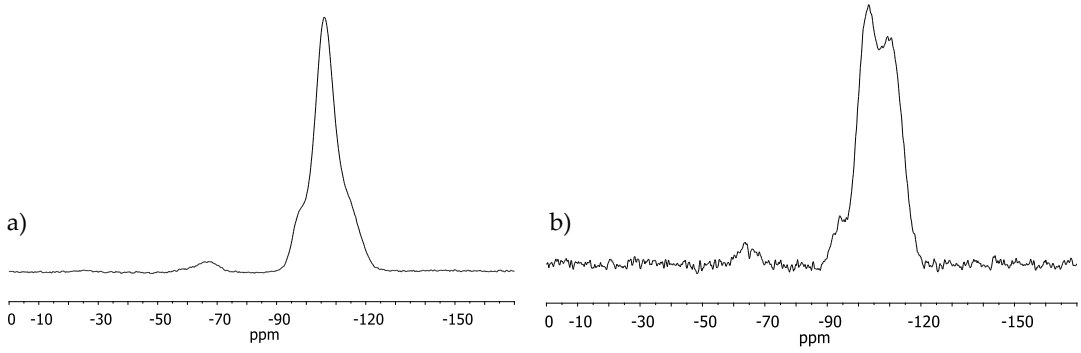

FIGURE A.6: Solid state ^{29}Si MAS NMR spectra of Sn-2-P123 (cross-polarization experiment) (a) and Sn-5-P123 (direct excitation experiments) (b) calcined at 250°C (8h)

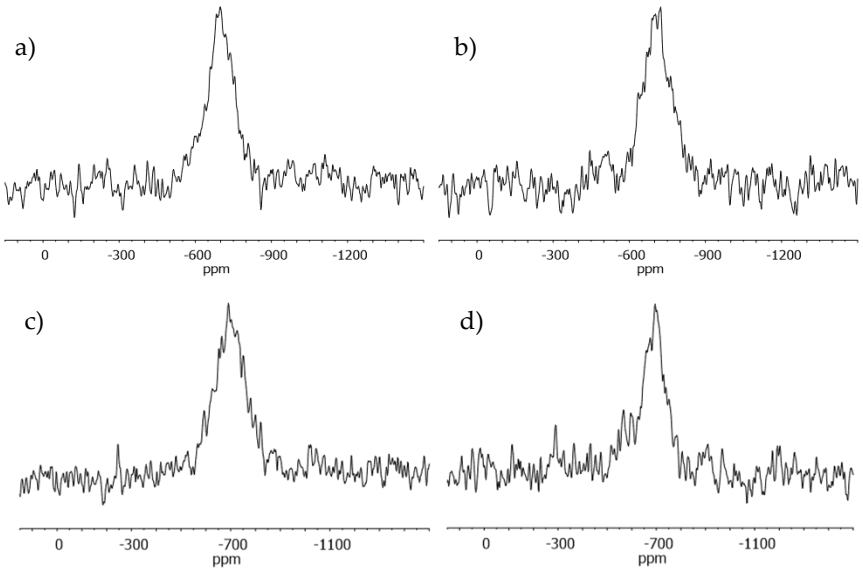

FIGURE A.7: ^{119}Sn static solid state NMR of Sn-2-P123 (a), Sn-2-F127 (b), Sn-5-F127 (c) and Sn-5-P123 (d) after calcination at 250 °C

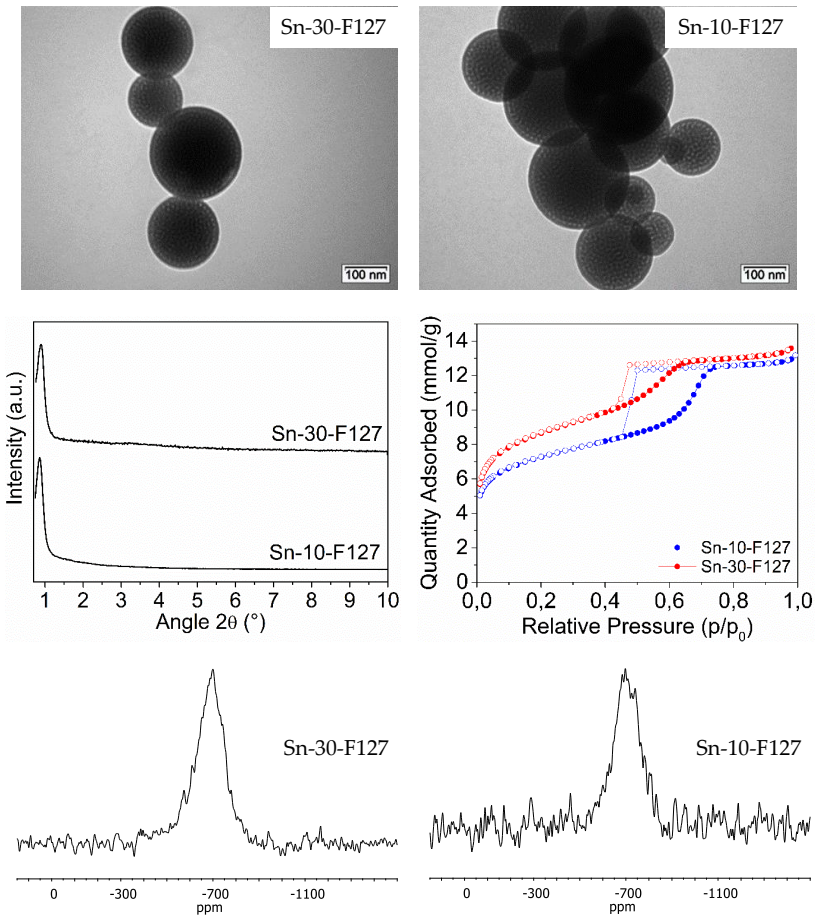

FIGURE A.8: TEM micrograph, nitrogen adsorption/desorption isotherms, Small-angle XRD patterns, ^{119}Sn static solid state NMR of Sn-10-F127 and Sn-30-F127

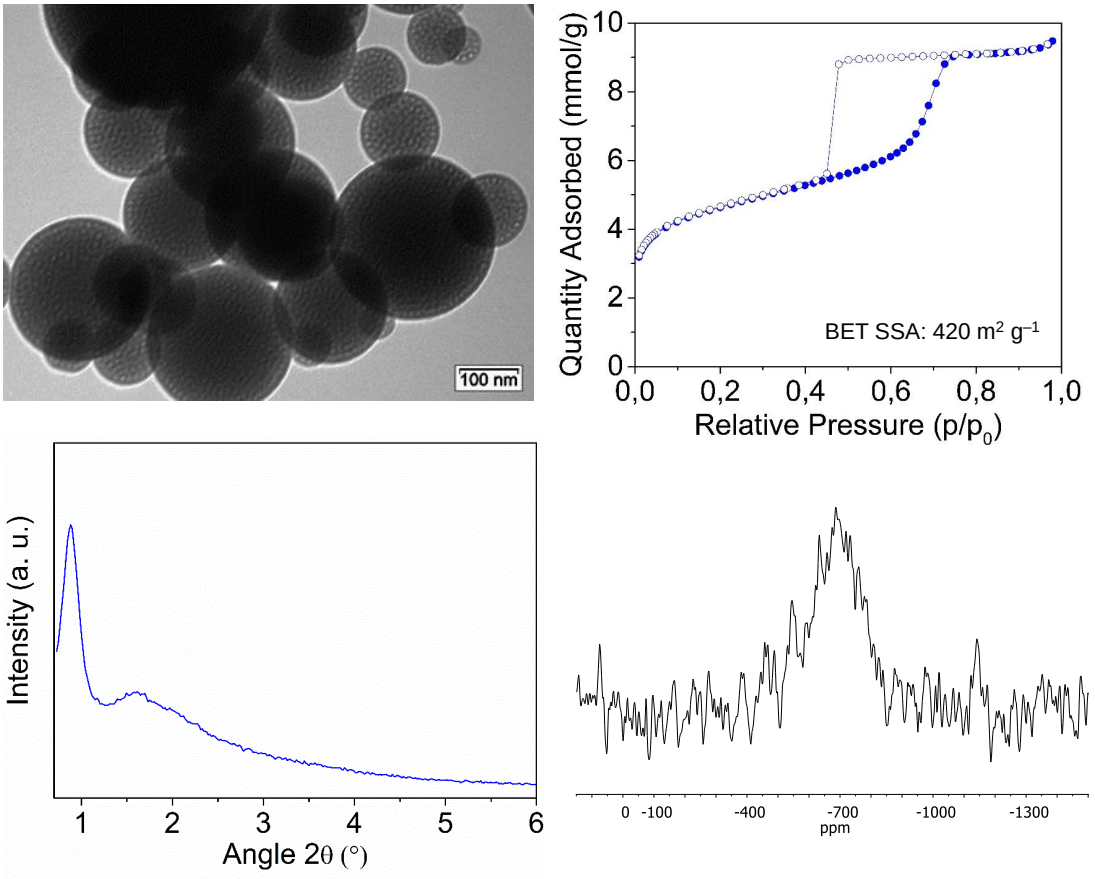

FIGURE A.9: TEM micrograph, nitrogen adsorption/desorption isotherms, Small-angle XRD patterns, ^{119}Sn static solid state NMR and physicochemical properties summary of Sn-0-F127

A.3 Chapter 4: Synthesis and in-depth characterization of Ga-based structured catalysts: enhancing glycerol conversion

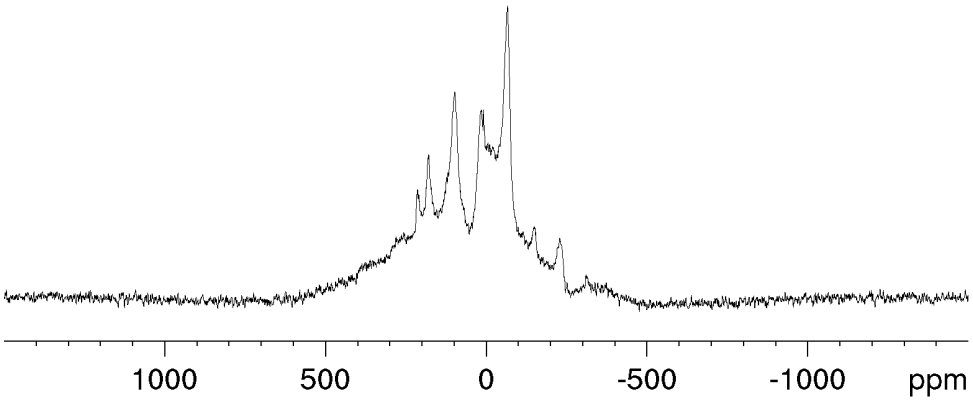

FIGURE A.10: ^{71}Ga solid state MAS NMR spectrum of pure β-Ga_2O_3, registered at 12.5 kHz, used as NMR reference compound. The spectrum presents the same pattern of signals, as reported in the literature by [D. Massiot, I. Farnan, N. Gautier, D. Trumeau, A. Trokiner and J. P. Coutures, Solid State Nuclear Magnetic Resonance, 1995, 4, 241-248.]

A.4 Chapter 5: Reusable surface-functionalized mesoporous gallosilicate catalysts for the sustainable upgrading of glycerol

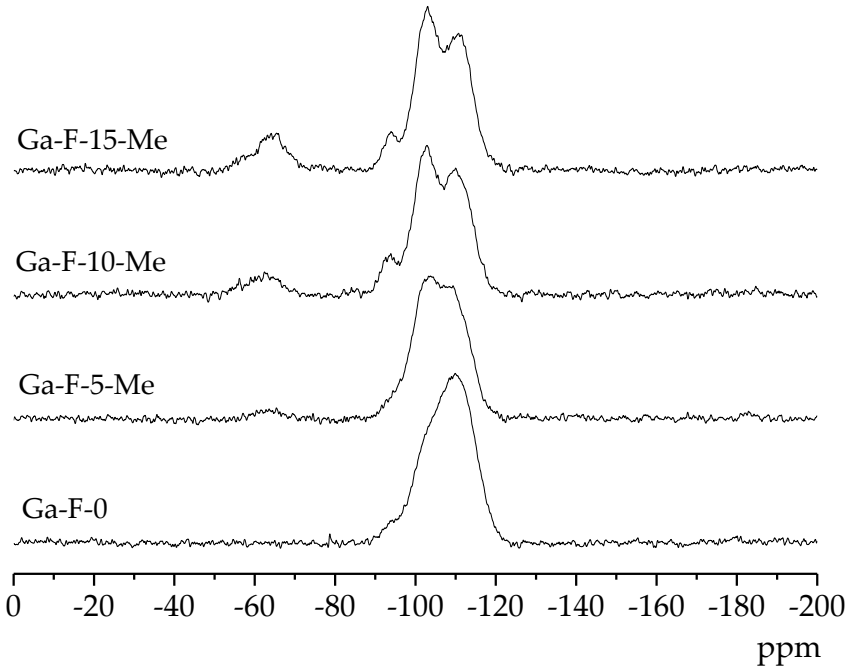

FIGURE A.11: ^{29}Si solid state MAS NMR spectra of Ga-F-0, Ga-F-5-Me, Ga-F-10-Me and Ga-F-15-Me after calcination at 250 °C for 8h (direct excitation experiment)

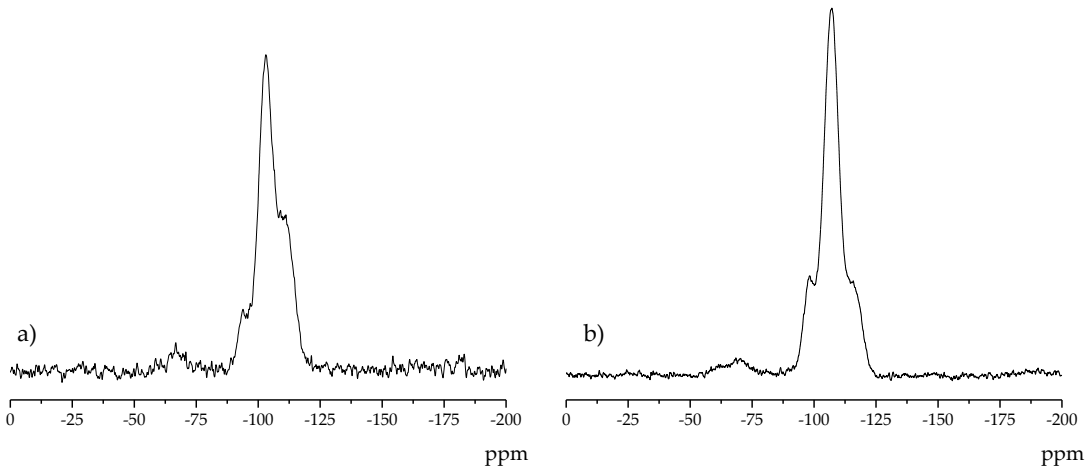

FIGURE A.12: ^{29}Si solid state MAS NMR spectra of Ga-P-5-Pr, (a) before calcination (direct excitation experiment) and (b) after calcination at 250 °C for 8h (cross-polarization experiment)

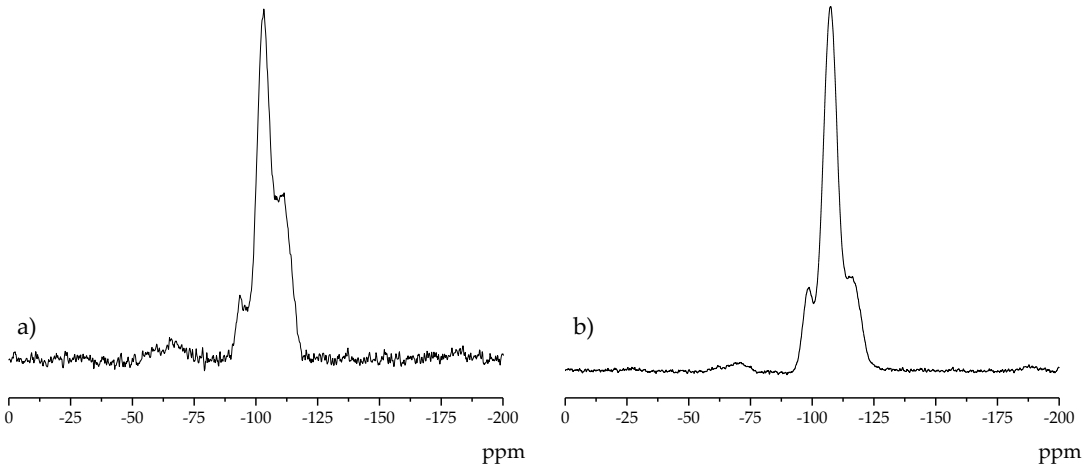

FIGURE A.13: ^{29}Si solid state MAS NMR spectra of Ga-F-5-Pr, (a) before calcination (direct excitation experiment) and (b) after calcination at 250 °C for 8h (cross-polarization experiment)

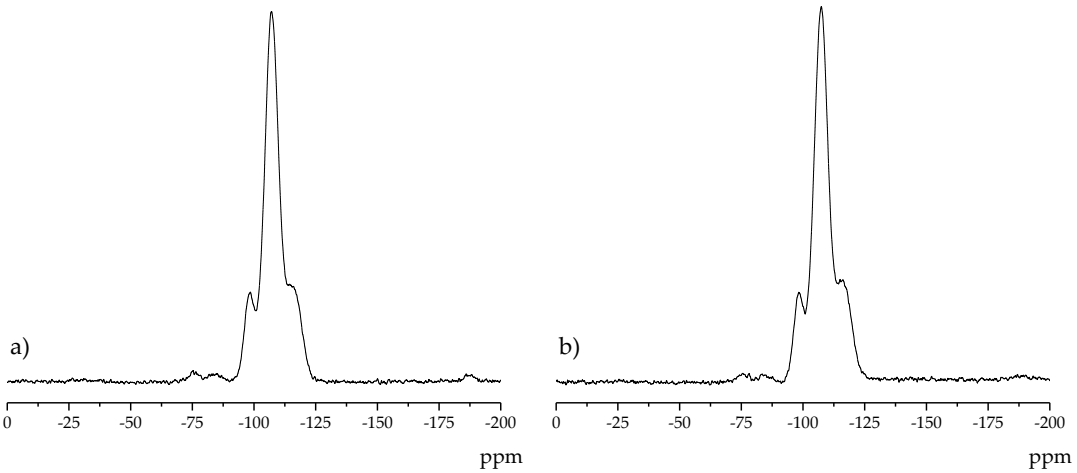

FIGURE A.14: ^{29}Si solid state MAS NMR spectra of (a) Ga-P-5-Ph and (b) Ga-F-5-Ph after calcination at 250 °C for 8h (cross-polarization experiments)

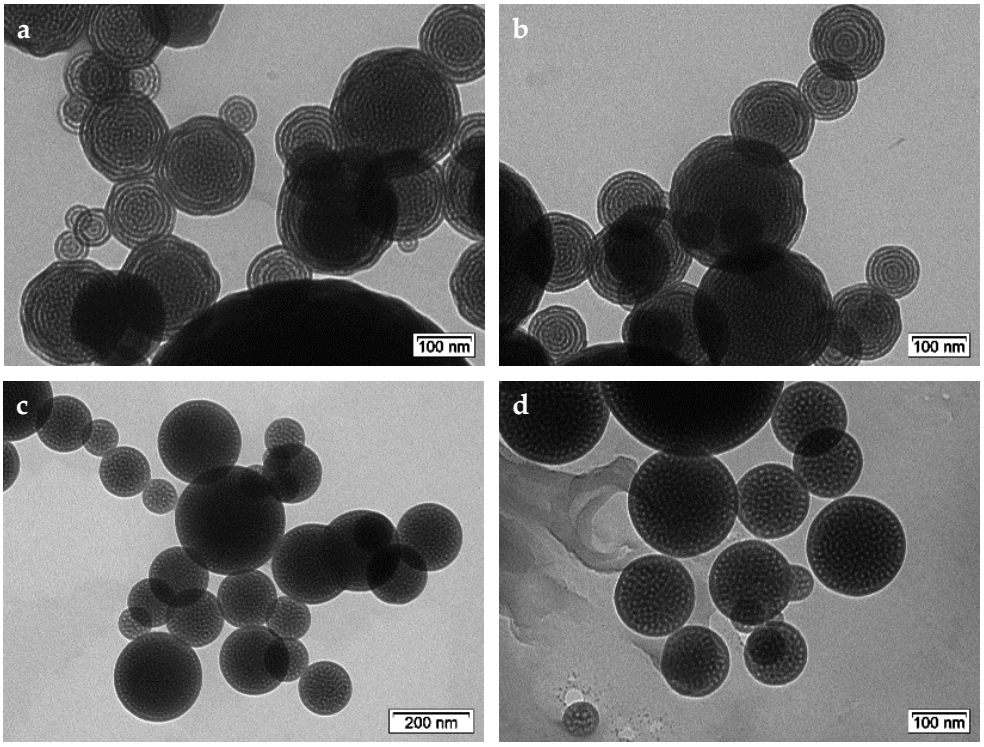

FIGURE A.15: TEM pictures of (a) Ga-P-5-Pr, (b) Ga-P-5-Ph, (c) Ga-F-5-Pr and (d) Ga-F-5-Ph

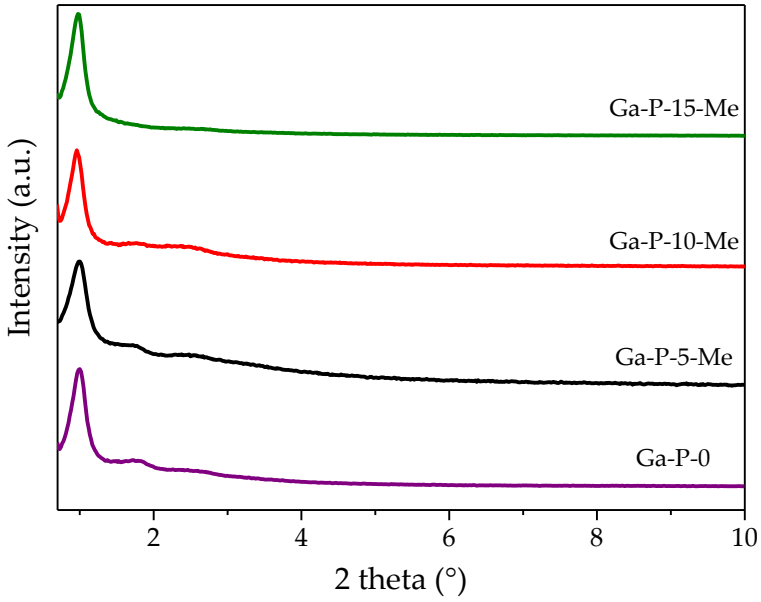

FIGURE A.16: XRD patterns of Ga-P-0, Ga-P-5-Me, Ga-P-10-Me and Ga-P-15-Me

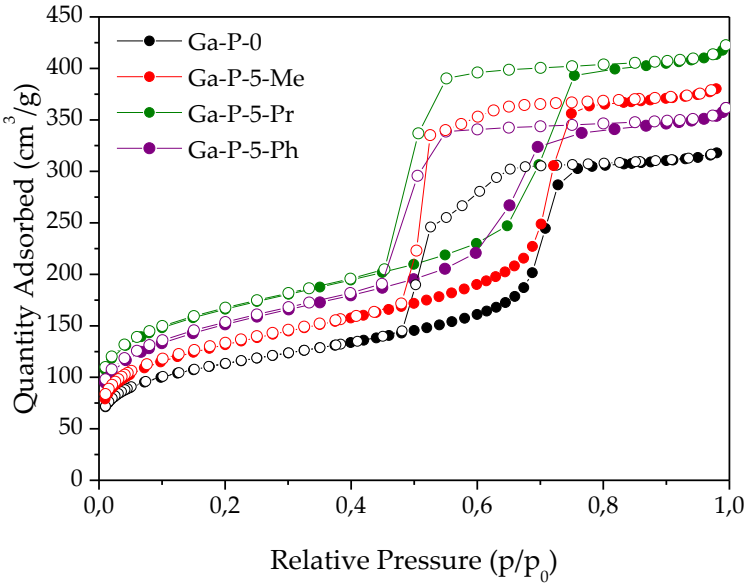

FIGURE A.17: Nitrogen adsorption/desorption isotherms of Ga-P-0, Ga-P-5-Me, Ga-P-5-Pr and Ga-P-5-Ph after calcination at 250 °C for 8h

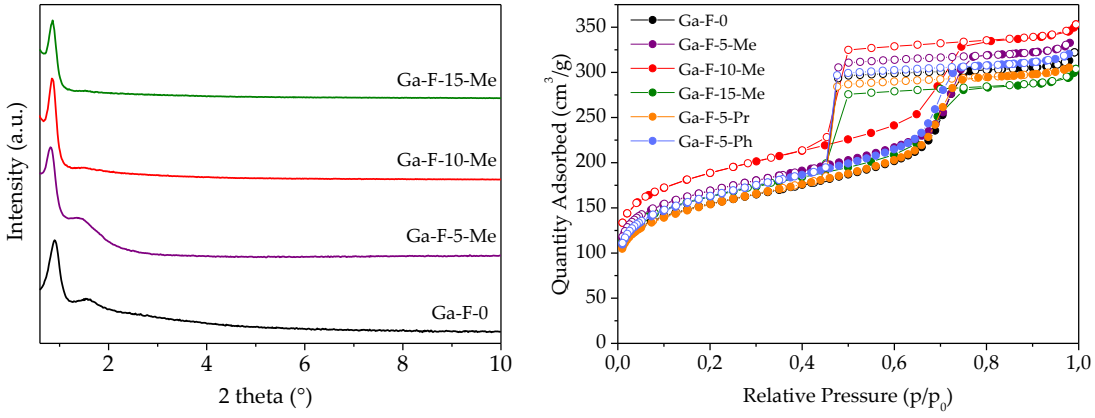

FIGURE A.18: XRD patterns of Ga-F-0, Ga-F-5-Me, Ga-F-10-Me and Ga-F-15-Me (left) and nitrogen adsorption/desorption isotherms of Ga-F-0, Ga-F-5-Me, Ga-F-10-Me, Ga-F-15-Me, Ga-F-5-Pr and Ga-F-5-Ph after calcination at 250 °C (right)

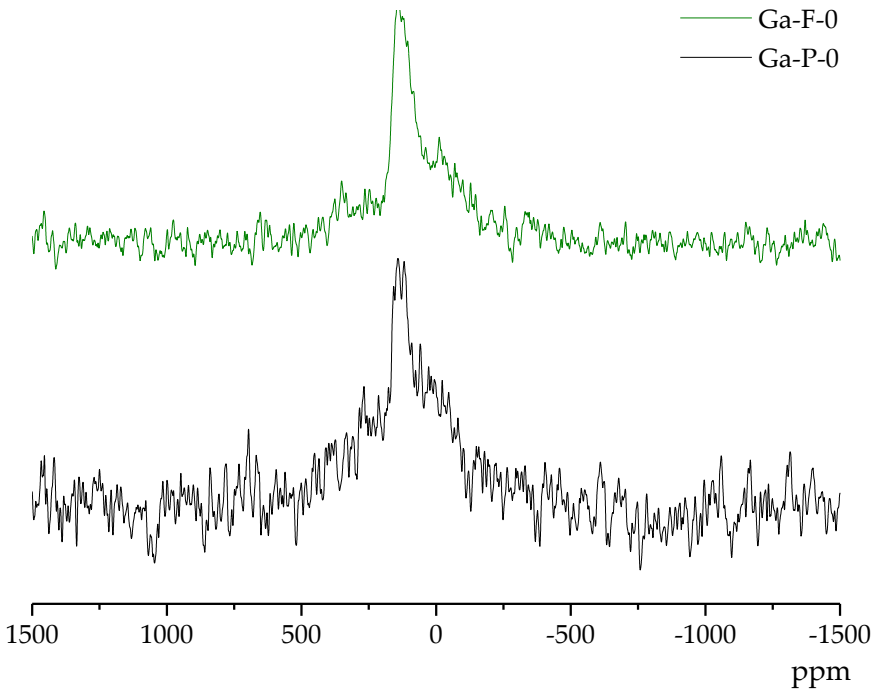

FIGURE A.19: ^{71}Ga solid state MAS NMR spectra of Ga-P-0 and Ga-F-0

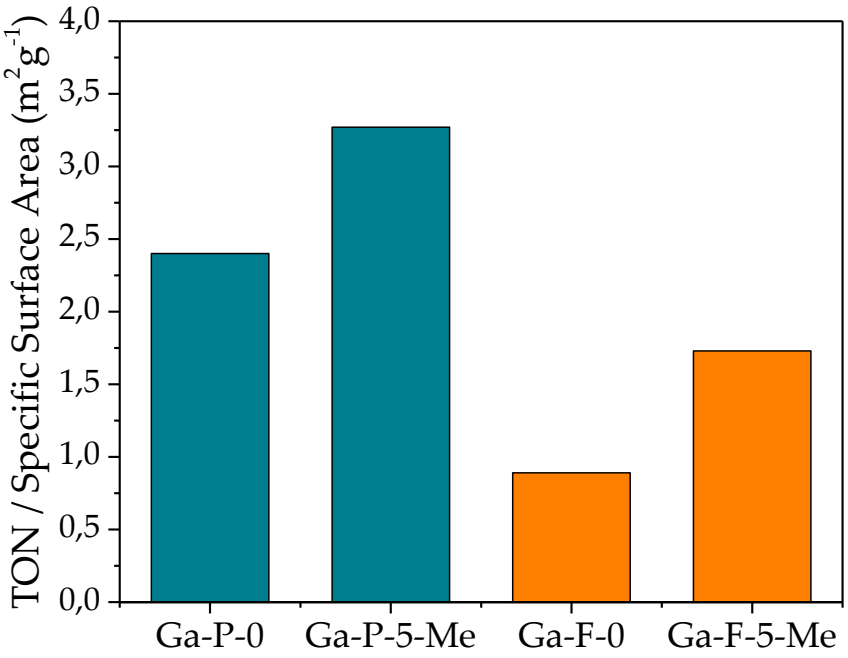

FIGURE A.20: Activity comparison of Ga-P-0, Ga-P-5-Me, Ga-F-0 and Ga-F-5-Me normalized by the specific surface area.

References

(1) Anastas, P. T.; Warner, J. C., *12 Principles of Green Chemistry. Green Chemistry: Theory and Practice*; Oxford Univ. Press New York: 1998.

(2) Climent, M. J.; Velty, A.; Corma, A. *Green Chemistry* **2002**, *4*, 565–569.

(3) Nanda, M. R.; Zhang, Y.; Yuan, Z.; Qin, W.; Ghaziaskar, H. S.; Xu, C. *Renewable and Sustainable Energy Reviews* **2016**, *56*, 1022–1031.

(4) Da Silva, C. X.; Gonçalves, V. L.; Mota, C. J. *Green Chemistry* **2009**, *11*, 38–41.

(5) Deutsch, J.; Martin, A.; Lieske, H. *Journal of Catalysis* **2007**, *245*, 428–435.

(6) Roldán, L.; Mallada, R.; Fraile, J. M.; Mayoral, J. A.; Menéndez, M. *Asia-Pacific Journal of Chemical Engineering* **2009**, *4*, 279–284.

(7) Vicente, G.; Melero, J. A.; Morales, G.; Paniagua, M.; Martín, E. *Green Chemistry* **2010**, *12*, 899–907.

(8) Li, L.; Korányi, T. I.; Sels, B. F.; Pescarmona, P. P. *Green Chemistry* **2012**, *14*, 1611–1619.

(9) Corma, A.; Iborra, S.; Velty, A. *Chemical Reviews* **2007**, *107*, 2411–2502.

(10) Sheldon, R. A. *Green Chemistry* **2005**, *7*, 267–278.

(11) Collard, X.; Li, L.; Lueangchaichaweng, W.; Bertrand, A.; Aprile, C.; Pescarmona, P. P. *Catalysis Today* **2014**, *235*, 184–192.

(12) Godard, N.; Collard, X.; Vivian, A.; Bivona, L. A.; Fiorilli, S.; Fusaro, L.; Aprile, C. *Applied Catalysis A: General* **2018**, *556*, 73–80.

(13) Godard, N.; Vivian, A.; Fusaro, L.; Cannavicci, L.; Aprile, C.; Debecker, D. P. *ChemCatChem* **2017**, *9*, 2211–2218.

(14) Cejka, J.; Corma, A.; Zones, S., *Zeolites and catalysis: synthesis, reactions and applications*; John Wiley & Sons: 2010.

(15) Breck, D. W., *Zeolite molecular sieves: structure, chemistry and use*; Krieger: 1984.

(16) Kresge, C.; Leonowicz, M.; Roth, W. J.; Vartuli, J.; Beck, J. *nature* **1992**, *359*, 710.

(17) Beck, J. S.; Vartuli, J.; Roth, W. J.; Leonowicz, M.; Kresge, C.; Schmitt, K.; Chu, C.; Olson, D. H.; Sheppard, E.; McCullen, S. *Journal of the American Chemical Society* **1992**, *114*, 10834–10843.

(18) Poyraz, A. S.; Kuo, C.-H.; Biswas, S.; King'ondu, C. K.; Suib, S. L. *Nature communications* **2013**, *4*, 2952.

(19) Tan, P.; Qin, J.-X.; Liu, X.-Q.; Yin, X.-Q.; Sun, L.-B. *Journal of Materials Chemistry A* **2014**, *2*, 4698–4705.

(20) Yang, M.; Li, S.; Wang, Y.; Herron, J. A.; Xu, Y.; Allard, L. F.; Lee, S.; Huang, J.; Mavrikakis, M.; Flytzani-Stephanopoulos, M. *Science* **2014**, *346*, 1498–1501.

(21) Liang, J.; Liang, Z.; Zou, R.; Zhao, Y. *Advanced Materials* **2017**, *29*, 1701139.

(22) Cheetham, A. K.; Férey, G.; Loiseau, T. *Angewandte Chemie International Edition* **1999**, *38*, 3268–3292.

(23) Corma, A; García, H.; Llabrés i Xamena, F. *Chemical reviews* **2010**, *110*, 4606–4655.

(24) Eddaoudi, M.; Moler, D. B.; Li, H.; Chen, B.; Reineke, T. M.; O'keeffe, M.; Yaghi, O. M. *Accounts of chemical research* **2001**, *34*, 319–330.

(25) Feng, D.; Chung, W.-C.; Wei, Z.; Gu, Z.-Y.; Jiang, H.-L.; Chen, Y.-P.; Darensbourg, D. J.; Zhou, H.-C. *Journal of the American Chemical Society* **2013**, *135*, 17105–17110.

(26) Feng, D.; Gu, Z.-Y.; Chen, Y.-P.; Park, J.; Wei, Z.; Sun, Y.; Bosch, M.; Yuan, S.; Zhou, H.-C. *Journal of the American Chemical Society* **2014**, *136*, 17714–17717.

(27) Cavka, J. H.; Jakobsen, S.; Olsbye, U.; Guillou, N.; Lamberti, C.; Bordiga, S.; Lillerud, K. P. *Journal of the American Chemical Society* **2008**, *130*, 13850–13851.

(28) Férey, G.; Mellot-Draznieks, C.; Serre, C.; Millange, F.; Dutour, J.; Surblé, S.; Margiolaki, I. *Science* **2005**, *309*, 2040–2042.

(29) Beck, J. *W. J. Roth, JC Vartuli, WO Patent* **1991**, 91–11390.

(30) Occelli, M. L.; Robson, H. E. *ACS Publications* **1989**.

(31) Tsuneo, Y.; Toshio, S.; Kazuyuki, K.; Chuzo, K. *Bulletin of the Chemical Society of Japan* **1990**, *63*, 1535–1537.

(32) Hoffmann, F.; Fröba, M. *Chemical Society Reviews* **2011**, *40*, 608–620.

(33) Tanev, P. T.; Pinnavaia, T. J. *science* **1995**, *267*, 865–867.

(34) Tanev, P. T.; Chibwe, M.; Pinnavaia, T. J. *Nature* **1994**, *368*, 321.

(35) Bagshaw, S. A.; Prouzet, E.; Pinnavaia, T. J. *Science* **1995**, *269*, 1242–1244.

(36) Zhao, D.; Huo, Q.; Feng, J.; Chmelka, B. F.; Stucky, G. D. *Journal of the American Chemical Society* **1998**, *120*, 6024–6036.

(37) Zhao, D.; Feng, J.; Huo, Q.; Melosh, N.; Fredrickson, G. H.; Chmelka, B. F.; Stucky, G. D. *science* **1998**, *279*, 548–552.

(38) Yang, P.; Zhao, D.; Margolese, D. I.; Chmelka, B. F.; Stucky, G. D. *Chemistry of Materials* **1999**, *11*, 2813–2826.

(39) Hoffmann, F.; Cornelius, M.; Morell, J.; Fröba, M. *Angewandte Chemie International Edition* **2006**, *45*, 3216–3251.

(40) Mou, C.-Y.; Lin, H.-P. *Pure and applied chemistry* **2000**, *72*, 137–146.

(41) Zhao, T.; Elzatahry, A.; Li, X.; Zhao, D. *Nature Reviews Materials* **2019**, 1–17.

(42) Adachi, M.; Harada, T.; Harada, M. *Langmuir* **1999**, *15*, 7097–7100.

(43) Debecker, D. P.; Le Bras, S.; Boissière, C.; Chaumonnot, A.; Sanchez, C. *Chemical Society Reviews* **2018**, *47*, 4112–4155.

(44) Debecker, D. P. *The Chemical Record* **2018**, *18*, 662–675.

(45) Tuel, A. *Microporous and Mesoporous Materials* **1999**, *27*, 151–169.

(46) Cejka, J.; Corma, A.; Zones, S., *Zeolites and catalysis: synthesis, reactions and applications*; John Wiley & Sons: 2010.

(47) Shamzhy, M.; Opanasenko, M.; Concepción, P.; Martínez, A. *Chemical Society Reviews* **2019**, *48*, 1095–1149.

(48) Čejka, J.; Wichterlová, B. *Catalysis reviews* **2002**, *44*, 375–421.

(49) Meeprasert, J.; Jungsuttiwong, S.; Namuangruk, S. *Microporous and Mesoporous Materials* **2013**, *175*, 99–106.

(50) Kosslick, H; Lischke, G; Parlitz, B; Storek, W; Fricke, R *Applied Catalysis A: General* **1999**, *184*, 49–60.

(51) Li, H.; Zhou, D.; Tian, D.; Shi, C.; Müller, U.; Feyen, M.; Yilmaz, B.; Gies, H.; Xiao, F.; De Vos, D. *ChemPhysChem* **2014**, *15*, 1700–1707.

(52) Wang, A.; Austin, D.; Karmakar, A.; Bernard, G. M.; Michaelis, V. K.; Yung, M. M.; Zeng, H.; Song, H. *ACS Catalysis* **2017**, *7*, 3681–3692.

(53) Fang, Y.; Su, X.; Bai, X.; Wu, W.; Wang, G.; Xiao, L.; Yu, A. *Journal of energy chemistry* **2017**, *26*, 768–775.

(54) Yang, G.; Zhou, L.; Han, X. *Journal of Molecular Catalysis A: Chemical* **2012**, *363*, 371–379.

(55) Lewis, J. D.; Van de Vyver, S.; Crisci, A. J.; Gunther, W. R.; Michaelis, V. K.; Griffin, R. G.; Román-Leshkov, Y. *ChemSusChem* **2014**, *7*, 2255–2265.

(56) Twaiq, F. A.; Mohamed, A. R.; Bhatia, S. *Microporous and Mesoporous Materials* **2003**, *64*, 95–107.

(57) Byambajav, E.; Ohtsuka, Y. *Fuel* **2003**, *82*, 1571–1577.

(58) Taguchi, A.; Schüth, F. *Microporous and Mesoporous Materials* **2005**, *77*, 1–45.

(59) Okumura, K.; Nishigaki, K.; Niwa, M. *Microporous and Mesoporous Materials* **2001**, *44-45*, 509–516.

(60) Climent, M. J.; Corma, A.; Iborra, S.; Navarro, M. C.; Primo, J. *Journal of Catalysis* **1996**, *161*, 783–789.

(61) Climent, M. J.; Corma, A.; Guil-López, R.; Iborra, S.; Primo, J. *Journal of Catalysis* **1998**, *175*, 70–79.

(62) Onaka, M.; Hashimoto, N.; Kitabata, Y.; Yamasaki, R. *Applied Catalysis A: General* **2003**, *241*, 307–317.

(63) Kugita, T.; Jana, S. K.; Owada, T.; Hashimoto, N.; Onaka, M.; Namba, S. *Applied Catalysis A: General* **2003**, *245*, 353–362.

(64) Zhu, Y.; Jaenicke, S.; Chuah, G. K. *Journal of Catalysis* **2003**, *218*, 396–404.

(65) Moliner, M.; Román-Leshkov, Y.; Davis, M. E. *Proceedings of the National Academy of Sciences* **2010**, *107*, 6164–6168.

(66) Nikolla, E.; Román-Leshkov, Y.; Moliner, M.; Davis, M. E. *Acs Catalysis* **2011**, *1*, 408–410.

(67) Holm, M. S.; Saravanamurugan, S.; Taarning, E. *Science* **2010**, *328*, 602–605.

(68) Taarning, E.; Saravanamurugan, S.; Spangsberg Holm, M.; Xiong, J.; West, R. M.; Christensen, C. H. *ChemSusChem* **2009**, *2*, 625–627.

(69) Li, L.; Stroobants, C.; Lin, K.; Jacobs, P. A.; Sels, B. F.; Pescarmona, P. P. *Green Chemistry* **2011**, *13*, 1175–1181.

(70) Corma, A.; Domine, M. E.; Valencia, S. *Journal of Catalysis* **2003**, *215*, 294–304.

(71) Boronat, M.; Concepción, P.; Corma, A.; Renz, M.; Valencia, S. *Journal of Catalysis* **2005**, *234*, 111–118.

(72) Boronat, M.; Corma, A.; Renz, M. *The journal of physical chemistry B* **2006**, *110*, 21168–21174.

(73) Boronat, M.; Corma, A.; Renz, M.; Viruela, P. M. *Chemistry–A European Journal* **2006**, *12*, 7067–7077.

(74) Boronat, M.; Concepción, P.; Corma, A.; Navarro, M. T.; Renz, M.; Valencia, S. *Physical Chemistry Chemical Physics* **2009**, *11*, 2876–2884.

(75) Boronat, M.; Concepción, P.; Corma, A.; Renz, M. *Catalysis today* **2007**, *121*, 39–44.

(76) Brand, S. K.; Labinger, J. A.; Davis, M. E. *ChemCatChem* **2016**, *8*, 121–124.

(77) Buckles, G.; Hutchings, G. J.; Williams, C. D. *Catalysis letters* **1991**, *11*, 89–93.

(78) Fricke, R.; Kosslick, H.; Lischke, G.; Richter, M. *Chemical Reviews* **2000**, *100*, 2303–2406.

(79) Kosslick, H.; Lischke, G.; Landmesser, H.; Parlitz, B.; Storek, W.; Fricke, R. *Journal of Catalysis* **1998**, *176*, 102–114.

(80) Takeguchi, T.; Kim, J.-B.; Kang, M.; Inui, T.; Cheuh, W.-T.; Haller, G. L. *Journal of Catalysis* **1998**, *175*, 1–6.

(81) Dumesic, J. A.; Huber, G. W.; Boudart, M. *Handbook of Heterogeneous Catalysis: Online* **2008**.

(82) Falconer, J. L.; Schwarz, J. A. *Catalysis Reviews* **1983**, *25*, 141–227.

(83) Sandoval-Díaz, L.-E.; González-Amaya, J.-A.; Trujillo, C.-A. *Microporous and mesoporous materials* **2015**, *215*, 229–243.

(84) Damjanović, L.; Auroux, A. In *Zeolite characterization and catalysis*; Springer: 2009, pp 107–167.

(85) Shen, J.; Auroux, A In *Studies in Surface Science and Catalysis*; Elsevier: 2004, pp 35–70.

(86) Jentys, A; Lercher, J. In *Studies in Surface Science and Catalysis*; Elsevier: 2001, pp 345–386.

(87) Chakraborty, B.; Viswanathan, B. *Catalysis Today* **1999**, *49*, 253–260.

(88) Fritz, P. O.; Lunsford, J. H. *Journal of Catalysis* **1989**, *118*, 85–98.

(89) Tsyganenko, A. A.; Denisenko, L. A.; Zverev, S. M.; Filimonov, V. N. *Journal of Catalysis* **1985**, *94*, 10–15.

(90) Zecchina, A.; Coluccia, S.; Guglielminotti, E.; Ghiotti, G. *The Journal of Physical Chemistry* **1971**, *75*, 2790–2798.

(91) Hunger, M. *Zeolites and catalysis: synthesis, reactions and applications* **2010**, *2*, 493–546.

(92) Lercher, J. A.; Gründling, C.; Eder-Mirth, G. *Catalysis Today* **1996**, *27*, 353–376.

(93) Zhang, W.; Ma, D.; Liu, X.; Liu, X.; Bao, X. *Chemical Communications* **1999**, 1091–1092.

(94) Baerlocher, C.; McCusker, L. B.; Olson, D. H., *Atlas of zeolite framework types*; Elsevier: 2007.

(95) Zhang, W.; Bao, X.; Guo, X.; Wang, X. *Catalysis Letters* **1999**, *60*, 89–94.

(96) Biaglow, A. I.; Gorte, R. J.; Kokotailo, G. T.; White, D. *Journal of Catalysis* **1994**, *148*, 779–786.

(97) Biaglow, A. I.; Gorte, R. J.; White, D. *Journal of Catalysis* **1994**, *150*, 221–224.

(98) Haw, J. F. *Physical Chemistry Chemical Physics* **2002**, *4*, 5431–5441.

(99) Haw, J. F.; Nicholas, J. B.; Xu, T.; Beck, L. W.; Ferguson, D. B. *Accounts of Chemical Research* **1996**, *29*, 259–267.

(100) Pazè, C.; Zecchina, A.; Spera, S.; Cosma, A.; Merlo, E.; Spanò, G.; Girotti, G. *Physical Chemistry Chemical Physics* **1999**, *1*, 2627–2629.

(101) Huang, J.; Jiang, Y.; Reddy Marthala, V. R.; Wang, W.; Sulikowski, B.; Hunger, M. *Microporous and Mesoporous Materials* **2007**, *99*, 86–90.

(102) Huang, J.; Jiang, Y.; Marthala, V. R. R.; Thomas, B.; Romanova, E.; Hunger, M. *The Journal of Physical Chemistry C* **2008**, *112*, 3811–3818.

(103) Lee, D.; Monin, G.; Duong, N. T.; Lopez, I. Z.; Bardet, M.; Mareau, V.; Gonon, L.; De Paëpe, G. *Journal of the American Chemical Society* **2014**, *136*, 13781–13788.

(104) Gladden, L. F.; Lutecki, M.; McGregor, J. *Characterization of Solid Materials and Heterogeneous Catalysts: From Structure to Surface Reactivity* **2012**, 289–342.

(105) Engelhardt, G.; Koller, H. In *Solid-State NMR II*; Springer: 1994, pp 1–29.

(106) Engelhardt, G.; Michel, D.

(107) Grimmer, A.-R.; Von Lampe, F; Mägi, M *Chemical physics letters* **1986**, *132*, 549–553.

(108) Chuang, I. S.; Kinney, D. R.; Maciel, G. E. *Journal of the American Chemical Society* **1993**, *115*, 8695–8705.

(109) Chuang, I.-S.; Maciel, G. E. *Journal of the American Chemical Society* **1996**, *118*, 401–406.

(110) Kobayashi, T.; DiVerdi, J. A.; Maciel, G. E. *The Journal of Physical Chemistry C* **2008**, *112*, 4315–4326.

(111) Zaera, F. *Catalysis letters* **2012**, *142*, 501–516.

(112) Gosselink, R.; Xia, W; Muhler, M; De Jong, K.; Bitter, J. *ACS Catalysis* **2013**, *3*, 2397–2402.

(113) Bhaumik, A.; Tatsumi, T. *Journal of Catalysis* **2000**, *189*, 31–39.

(114) Pena, M.; Dellarocca, V; Rey, F; Corma, A; Coluccia, S.; Marchese, L *Microporous and mesoporous materials* **2001**, *44*, 345–356.

(115) Wu, P.; Tatsumi, T.; Komatsu, T.; Yashima, T. *Chemistry of Materials* **2002**, *14*, 1657–1664.

(116) Manangon-Perugachi, L. E.; Vivian, A.; Eloy, P.; Debecker, D. P.; Aprile, C.; Gaigneaux, E. M. *Catalysis Today* **2019**, DOI: `https://doi.org/10.1016/j.cattod.2019.05.020`.

(117) Smeets, V.; Ben Mustapha, L.; Schnee, J.; Gaigneaux, E. M.; Debecker, D. P. *Molecular Catalysis* **2018**, *452*, 123–128.

(118) Fraile, J. M.; Garcia, J. I.; Mayoral, J. A.; Vispe, E. *Journal of Catalysis* **2000**, *189*, 40–51.

(119) Fraile, J. M.; Garcia, J. I.; Mayoral, J. A.; Vispe, E. *Journal of Catalysis* **2001**, *204*, 146–156.

(120) Karimi, B.; Mirzaei, H. M. *RSC Advances* **2013**, *3*, 20655–20661.

(121) Bozbas, K. *Renewable and Sustainable Energy Reviews* **2008**, *12*, 542–552.

(122) Pagliaro, M.; Ciriminna, R.; Kimura, H.; Rossi, M.; Della Pina, C. *Angewandte Chemie International Edition* **2007**, *46*, 4434–4440.

(123) Díaz-Álvarez, A. E.; Francos, J.; Lastra-Barreira, B.; Crochet, P.; Cadierno, V. *Chemical Communications* **2011**, *47*, 6208–6227.

(124) Chai, S.-H.; Wang, H.-P.; Liang, Y.; Xu, B.-Q. *Journal of Catalysis* **2007**, *250*, 342–349.

(125) Dasari, M. A.; Kiatsimkul, P.-P.; Sutterlin, W. R.; Suppes, G. J. *Applied Catalysis A: General* **2005**, *281*, 225–231.

(126) Klepáčová, K.; Mravec, D.; Bajus, M. *Applied Catalysis A: General* **2005**, *294*, 141–147.

(127) Soares, R. R.; Simonetti, D. A.; Dumesic, J. A. *Angewandte Chemie International Edition* **2006**, *45*, 3982–3985.

(128) Behr, A.; Eilting, J.; Irawadi, K.; Leschinski, J.; Lindner, F. *Green Chemistry* **2008**, *10*, 13–30.

(129) Drumright, R. E.; Gruber, P. R.; Henton, D. E. *Advanced Materials* **2000**, *12*, 1841–1846.

(130) Orazov, M.; Davis, M. E. *Proceedings of the National Academy of Sciences* **2015**, *112*, 11777–11782.

(131) Maki-Arvela, P.; Simakova, I. L.; Salmi, T.; Murzin, D. Y. *Chemical reviews* **2013**, *114*, 1909–1971.

(132) Pescarmona, P. P.; Janssen, K. P. F.; Delaet, C.; Stroobants, C.; Houthoofd, K.; Philippaerts, A.; De Jonghe, C.; Paul, J. S.; Jacobs, P. A.; Sels, B. F. *Green Chemistry* **2010**, *12*, 1083–1089.

(133) Tosi, I.; Riisager, A.; Taarning, E.; Jensen, P. R.; Meier, S. *Catalysis Science & Technology* **2018**, *8*, 2137–2145.

(134) Osmundsen, C. M.; Holm, M. S.; Dahl, S.; Taarning, E. *Proceedings of the Royal Society A: Mathematical, Physical and Engineering Sciences* **2012**, *468*, 2000–2016.

(135) Li, L.; Collard, X.; Bertrand, A.; Sels, B. F.; Pescarmona, P. P.; Aprile, C. *Journal of Catalysis* **2014**, *314*, 56–65.

(136) De Clippel, F.; Dusselier, M.; Van Rompaey, R.; Vanelderen, P.; Dijkmans, J.; Makshina, E.; Giebeler, L.; Oswald, S.; Baron, G. V.; Denayer, J. F. *Journal of the American chemical society* **2012**, *134*, 10089–10101.

(137) Crotti, C.; Farnetti, E.; Guidolin, N. *Green chemistry* **2010**, *12*, 2225–2231.

(138) Nanda, M. R.; Yuan, Z.; Qin, W.; Ghaziaskar, H. S.; Poirier, M.-A.; Xu, C. C. *Fuel* **2014**, *117*, 470–477.

(139) Clarkson, J. S.; Walker, A. J.; Wood, M. A. *Organic process research & development* **2001**, *5*, 630–635.

(140) Ferreira, P; Fonseca, I.; Ramos, A.; Vital, J; Castanheiro, J. *Applied Catalysis B: Environmental* **2010**, *98*, 94–99.

(141) Debecker, D. P.; Boissière, C.; Laurent, G.; Huet, S.; Eliaers, P.; Sanchez, C.; Backov, R. *Chemical Communications* **2015**, *51*, 14018–14021.

(142) Jiang, Y.; Zhao, Y.; Xu, X.; Lin, K.; Wang, D. *RSC Advances* **2016**, *6*, 77481–77488.

(143) Lin, K.; Lebedev, O. I.; Van Tendeloo, G.; Jacobs, P. A.; Pescarmona, P. P. *Chemistry–A European Journal* **2010**, *16*, 13509–13518.

(144) Tolborg, S.; Sádaba, I.; Osmundsen, C. M.; Fristrup, P.; Holm, M. S.; Taarning, E. *ChemSusChem* **2015**, *8*, 613–617.

(145) Boissiere, C.; Grosso, D.; Chaumonnot, A.; Nicole, L.; Sanchez, C. *Advanced Materials* **2011**, *23*, 599–623.

(146) Lu, Y.; Fan, H.; Stump, A.; Ward, T. L.; Rieker, T.; Brinker, C. J. *Nature* **1999**, *398*, 223.

(147) Debecker, D. P.; Stoyanova, M.; Colbeau-Justin, F.; Rodemerck, U.; Boissière, C.; Gaigneaux, E. M.; Sanchez, C. *Angewandte Chemie International Edition* **2012**, *51*, 2129–2131.

(148) Lari, G. M.; Dapsens, P. Y.; Scholz, D.; Mitchell, S; Mondelli, C.; Pérez-Ramírez, J. *Green Chemistry* **2016**, *18*, 1249–1260.

(149) Cossement, C.; Darville, J.; Gilles, J.-M.; Nagy, J. B.; Fernandez, C.; Amoureux, J.-P. *Magnetic Resonance in Chemistry* **1992**, *30*, 263–270.

(150) Huang, L.; Kruk, M. *Chemistry of Materials* **2015**, *27*, 679–689.

(151) Selvaraj, M.; Kawi, S.; Park, D.-W.; Ha, C.-S. *Microporous and Mesoporous Materials* **2009**, *117*, 586–595.

(152) Shah, P.; Ramaswamy, A. V.; Lazar, K.; Ramaswamy, V. *Microporous and Mesoporous Materials* **2007**, *100*, 210–226.

(153) Kruk, M.; Jaroniec, M.; Sayari, A. *The Journal of Physical Chemistry B* **1997**, *101*, 583–589.

(154) Jaroniec, M.; Solovyov, L. A. *Langmuir* **2006**, *22*, 6757–6760.

(155) Wu, S.; Han, Y.; Zou, Y.-C.; Song, J.-W.; Zhao, L.; Di, Y.; Liu, S.-Z.; Xiao, F.-S. *Chemistry of Materials* **2004**, *16*, 486–492.

(156) Shah, P.; Ramaswamy, V. *Microporous and Mesoporous Materials* **2008**, *114*, 270–280.

(157) Chaudhari, K.; Das, T. K.; Rajmohanan, P. R.; Lazar, K.; Sivasanker, S.; Chandwadkar, A. J. *Journal of Catalysis* **1999**, *183*, 281–291.

(158) Renz, M.; Blasco, T.; Corma, A.; Fornés, V.; Jensen, R.; Nemeth, L. *Chemistry – A European Journal* **2002**, *8*, 4708–4717.

(159) Xu, R.; Pang, W.; Yu, J.; Huo, Q.; Chen, J., *Chemistry of zeolites and related porous materials: synthesis and structure*; John Wiley & Sons: 2009.

(160) Yan, Z.; Ma, D.; Zhuang, J.; Liu, X.; Liu, X.; Han, X.; Bao, X.; Chang, F.; Xu, L.; Liu, Z. *Journal of Molecular Catalysis A: Chemical* **2003**, *194*, 153–167.

(161) Shah, P.; Ramaswamy, A. V.; Lazar, K.; Ramaswamy, V. *Microporous and Mesoporous Materials* **2007**, *100*, 210–226.

(162) Piumetti, M.; Armandi, M.; Garrone, E.; Bonelli, B. *Microporous and Mesoporous Materials* **2012**, *164*, 111–119.

(163) Busca, G., *Heterogeneous Catalytic Materials*; Elsevier: 2014, 103–195.

(164) Li, L.; Cani, D.; Pescarmona, P. P. *Inorganica Chimica Acta* **2015**, *431*, 289–296.

(165) Menezes, F. D.; Guimaraes, M. D.; da Silva, M. J. *Industrial & Engineering Chemistry Research* **2013**, *52*, 16709–16713.

(166) Bruinsma, P. J.; Kim, A. Y.; Liu, J.; Baskaran, S. *Chemistry of Materials* **1997**, *9*, 2507–2512.

(167) Bore, M. T.; Rathod, S. B.; Ward, T. L.; Datye, A. K. *Langmuir* **2003**, *19*, 256–264.

(168) Brinker, C. J.; Lu, Y.; Sellinger, A.; Fan, H. *Advanced materials* **1999**, *11*, 579–585.

(169) Hewitt, A. *Journal of aerosol science* **1993**, *24*, 155–162.

(170) Iskandar, F. *Advanced Powder Technology* **2009**, *20*, 283–292.

(171) Nandiyanto, A. B. D.; Okuyama, K. *Advanced Powder Technology* **2011**, *22*, 1–19.

(172) Debecker, D. P.; Stoyanova, M.; Rodemerck, U.; Colbeau-Justin, F.; Boissère, C.; Chaumonnot, A.; Bonduelle, A.; Sanchez, C. *Applied Catalysis A: General* **2014**, *470*, 458–466.

(173) Alarcón, E. A.; Villa, A. L.; de Correa, C. M. *Microporous and Mesoporous Materials* **2009**, *122*, 208–215.

(174) Bermejo-Deval, R.; Gounder, R.; Davis, M. E. *ACS catalysis* **2012**, *2*, 2705–2713.

(175) Mulvaney, P.; Grieser, F.; Meisel, D. *Langmuir* **1990**, *6*, 567–572.

(176) Luhmer, M *Magn. Reson. Imaging* **1996**, *14*, 911–913.

(177) Mal, N. K.; Ramaswamy, V.; Ganapathy, S; Ramaswamy, A. *Applied Catalysis A: General* **1995**, *125*, 233–245.

(178) Bruice, P. Y., *Organic Chemistry*; Pearson Prentice Hall: 2007.

(179) Collard, X.; Louette, P.; Fiorilli, S.; Aprile, C. *Physical Chemistry Chemical Physics* **2015**, *17*, 26756–26765.

(180) Yang, X.; Wu, L.; Wang, Z.; Bian, J.; Lu, T.; Zhou, L.; Chen, C.; Xu, J. *Catalysis Science & Technology* **2016**, *6*, 1757–1763.

(181) Sheldon, R. A. *Green Chemistry* **2017**, *19*, 18–43.

(182) Grudzien, R. M.; Jaroniec, M. *Chemical Communications* **2005**, 1076–1078.

(183) Zhao, L.; Zhu, G.; Zhang, D.; Di, Y.; Chen, Y.; Terasaki, O.; Qiu, S. *The Journal of Physical Chemistry B* **2005**, *109*, 764–768.

(184) Grudzien, R. M.; Grabicka, B. E.; Jaroniec, M. *Journal of Materials Chemistry* **2006**, *16*, 819–823.

(185) Jiang, X.; Brinker, C. J. *Journal of the American Chemical Society* **2006**, *128*, 4512–4513.

(186) Wang, Y.; Yang, C.; Zibrowius, B; Spliethoff, B; Lindén, M; Schüth, F *Chemistry of materials* **2003**, *15*, 5029–5035.

(187) Ji, X.; Hu, Q.; Hampsey, J. E.; Qiu, X.; Gao, L.; He, J.; Lu, Y. *Chemistry of materials* **2006**, *18*, 2265–2274.

(188) Prouzet, E.; Pinnavaia, T. J. *Angewandte Chemie International Edition in English* **1997**, *36*, 516–518.

(189) Rama Rao, G.; López, G. P.; Bravo, J.; Pham, H.; Datye, A. K.; Xu, H.; Ward, T. L. *Advanced materials* **2002**, *14*, 1301–1304.

(190) Moretti, G. *Journal of electron spectroscopy and related phenomena* **1998**, *95*, 95–144.

(191) Gaarenstroom, S.; Winograd, N. *The Journal of chemical physics* **1977**, *67*, 3500–3506.

(192) Moretti, G.; Filippone, F.; Satta, M. *Surface and Interface Analysis: An International Journal devoted to the development and application of techniques for the analysis of surfaces, interfaces and thin films* **2001**, *31*, 249–254.

(193) Bourque, J. L.; Biesinger, M. C.; Baines, K. M. *Dalton Transactions* **2016**, *45*, 7678–7696.

(194) Liu, R.-l.; Zhu, H.-q.; Wu, Z.-w.; Qin, Z.-f.; Fan, W.-b.; Wang, J.-g. *Journal of Fuel Chemistry and Technology* **2015**, *43*, 961–969.

(195) Wagner, C.; Joshi, A *Journal of Electron Spectroscopy and Related Phenomena* **1988**, *47*, 283–313.

(196) Moretti, G.; Palma, A.; Paparazzo, E.; Satta, M. *Surface Science* **2016**, *646*, 298–305.

(197) Massiot, D.; Farnan, I.; Gautier, N.; Trumeau, D.; Trokiner, A.; Coutures, J. P. *Solid State Nuclear Magnetic Resonance* **1995**, *4*, 241–248.

(198) Timken, H. K. C.; Oldfield, E. *Journal of the American Chemical Society* **1987**, *109*, 7669–7673.

(199) Chatterjee, M.; Iwasaki, T.; Onodera, Y.; Nagase, T.; Hayashi, H.; Ebina, T. *Chemistry of Materials* **2000**, *12*, 1654–1659.

(200) Bayense, C. R.; Kentgens, A. P. M.; De Haan, J. W.; Van de Ven, L. J. M.; Van Hooff, J. H. C. *The Journal of Physical Chemistry* **1992**, *96*, 775–782.

(201) Bivona, L. A.; Vivian, A.; Fusaro, L.; Fiorilli, S.; Aprile, C. *Applied Catalysis B: Environmental* **2019**, *247*, 182–190.

(202) Schüth, F.; Ward, M. D.; Buriak, J. M. *Chemistry of Materials* **2018**, *30*, 3599–3600.

(203) Vivian, A.; Fusaro, L.; Debecker, D. P.; Aprile, C. *ACS Sustainable Chemistry & Engineering* **2018**, *6*, 14095–14103.

(204) Luque, R.; Campelo, J. M.; Conesa, T. D.; Luna, D.; Marinas, J. M.; Romero, A. A. *Microporous and mesoporous materials* **2007**, *103*, 333–340.

(205) Okumura, K.; Nishigaki, K.; Niwa, M. *Microporous and mesoporous materials* **2001**, *44*, 509–516.

(206) Vansant, E. F.; Van Der Voort, P.; Vrancken, K. C., *Characterization and chemical modification of the silica surface*; Elsevier: 1995; Vol. 93.

(207) Matsumoto, A.; Sasaki, T.; Nishimiya, N.; Tsutsumi, K. *Colloids and Surfaces A: Physicochemical and Engineering Aspects* **2002**, *203*, 185–193.

(208) Bolis, V.; Fubini, B.; Marchese, L.; Martra, G.; Costa, D. *Journal of the Chemical Society, Faraday Transactions* **1991**, *87*, 497–505.

List of publications

Published articles

1. High-yield synthesis of ethyl lactate with mesoporous tin silicate catalysts prepared by an aerosol-assisted sol–gel process

   Godard, N.[#], Vivian, A.[#], Fusaro, L., Cannavicci, L., Aprile, C.[*], Debecker, D.P.[*]
   (2017) ChemCatChem, 9 (12), pp. 2211-2218.

2. Rapid room temperature synthesis of tin-based mesoporous solids: Influence of the particle size on the production of ethyl lactate

   Godard, N., Collard, X., Vivian, A., Bivona, L.A., Fiorilli, S., Fusaro, L., Aprile, C.[*]
   (2018) Applied Catalysis A: General, 556, pp. 73-80.

3. Mesoporous methyl-functionalized Sn-silicates generated by the aerosol process for the sustainable production of ethyl lactate

   Vivian, A., Fusaro, L., Debecker, D.P.[*], Aprile, C.[*]
   (2018) ACS Sustainable Chemistry and Engineering, 6 (11), pp. 14095-14103.

4. Hydrophobic titania-silica mixed oxides for the catalytic epoxidation of cyclooctene

   Manangon-Perugachi, L.E., Vivian, A., Eloy, P., Debecker, D.P., Aprile, C., Gaigneaux, E.M.[*]
   (2019) Catalysis Today, DOI: 10.1016/j.cattod.2019.05.020

5. Mercaptosilane-passivated $CuInS_2$ quantum dots for luminescence thermometry and luminescent labels

Marin, R., Vivian, A., Skripka, A., Migliori, A., Morandi, V., Enrichi, F., Vetrone, F., Ceroni, P., Aprile, C., Canton, P.[*]
(2019) ACS Applied Nano Materials, 2 (4), pp. 2426-2436.

6. Design and catalytic applications of 1D tubular nanostructures: Improving efficiency in glycerol conversion

   Bivona, L.A.[#]*, Vivian, A.*[#]*, Fusaro, L., Fiorilli, S., Aprile, C.*[*]
   (2019) Applied Catalysis B: Environmental, 247, pp. 182-190.

Submitted articles

1. Synthesis and in-depth characterization of Ga-based structured catalysts: enhancing glycerol conversion

   Vivian, A., Soumoy, L., Fusaro, L., Louette, P., Felten, A., Debecker, D.P., Aprile, C.[*]
   (2019) Applied Catalysis B: Environmental